

University of Alberta

**Changing Landscape Coatings for Bioactive Bone Fixation Implants via
Flame Spray Deposition**

by

Greg M. Nelson

A thesis submitted to the Faculty of Graduate Studies and Research
in partial fulfillment of the requirements for the degree of

Master of Science

in

Materials Engineering

Department of Chemical and Materials Engineering

©Greg M. Nelson

Fall 2013

Edmonton, Alberta

Permission is hereby granted to the University of Alberta Libraries to reproduce single copies of this thesis and to lend or sell such copies for private, scholarly or scientific research purposes only. Where the thesis is converted to, or otherwise made available in digital form, the University of Alberta will advise potential users of the thesis of these terms.

The author reserves all other publication and other rights in association with the copyright in the thesis and, except as herein before provided, neither the thesis nor any substantial portion thereof may be printed or otherwise reproduced in any material form whatsoever without the author's prior written permission.

Abstract

Owing to the bio-inert nature of load-bearing alloys and the brittle nature of bioactive materials there is a need to develop a composite bioactive material suitable for load-bearing applications. To fulfill this need, a new composite coating of a load-bearing alloy and a resorbable bioactive material was proposed. This composite coating system is termed a “changing landscape coating” owing to the replacement of the bioactive material with bone tissue over time. In this work, titanium or titanium alloy powder was blended with 45S5 bioactive glass powder and deposited with a flame spray torch. The effects of the type of titanium alloy, powder size distribution, and deposition condition were examined through experimental measurement and theoretical process modeling. It was shown that Ti-6Al-4V-based porous coatings, rather than titanium, may be a superior choice due to the potentially osteoproliferative bioactive glass, the potential ability to support viable tissue ingrowth, and the comparable strength to dense coatings.

Acknowledgments

First, I would like to thank my mentors, Dr. John Nychka and Dr. André McDonald, whom I have had the privilege of working with since September 2009 as an undergraduate student. From them I have learned so much including how to conduct, write about, and present research. I have learned to think, read, teach, and critique the work of others at an advanced level during my degree.

I am also indebted to my colleagues and friends in the Nychka and McDonald research groups for their support over the course of my degree. Special thanks go to Nicki, Mehdi, Michal, Natanael, and Dr. Sheila Passos for their help and support.

I am also thankful for the support provided by the excellent technical staff I have had the pleasure of working with. I would like to thank Mr. Shiraz Merali for conducting the XRD work and developing the XRD procedure presented herein. I would also like to thank Mr. Merali for his assistance and tutorship on all things XRD. I would like to thank Mr. Wayne Moffat and his laboratory staff for conducting the FTIR work as well as developing the FTIR protocols presented herein. I would like to thank Ms. De-Ann Rollings and Dr. Nathan Gerein for conducting the SEM imaging presented herein. I am also grateful to Mr. Ted Day of Mo-Sci Health Care Corporation who donated the bioactive glass powder used in this study.

Table of Contents

List of Figures	vi
List of Tables	xvi
List of Abbreviations	xviii
List of Symbols	xix
Chapter 1 – Introduction	1
1.1. Objectives	5
Chapter 2 – Literature Review	7
2.1. Biomaterials and Bioactivity	7
2.1.1. Tissue Fixation, Bioactivity, and Implants	7
2.1.1.1. Bio-inert Implants	8
2.1.1.2. Bioactive Implants	13
2.1.2. Mechanism of Bioactive Response and Assessment of Bioactivity... 16	
2.1.2.1. Bioactive Glass	16
2.1.2.2. Titanium and Titanium Dioxide (TiO ₂)	19
2.1.2.3. Hydroxyapatite (HA)	21
2.1.2.4. Implant Topography.....	22
2.2. Thermal Spray and Biomedical Coatings	24
2.3. Mechanical Assessment of Thermally Sprayed Coatings	28
2.4. Thermodynamic and Heat Transfer Modelling	31
Chapter 3 – Experimental Procedure	33
3.1. Experiments	33
3.2. Feedstock Materials	35
3.3. Thermal Spraying	37
3.3.1. Spray Conditions	37

3.3.2. Powder Blending and Deposition	38
3.4. Characterization	41
3.4.1. Particle Size Distribution (PSD)	41
3.4.2. Powder Morphology	41
3.4.3. Metallurgical Preparation and Optical Microscopy (OM)	42
3.4.3.1. Preliminary Composite Coatings	42
3.4.3.2. Cp-Ti and Ti-6Al-4V Alloy Composite Coatings	43
3.4.4. X-ray Diffraction (XRD)	47
3.5. In-Vitro Bioactivity Assessment	49
3.5.1. Simulated Body Fluid (SBF) Immersion Testing	49
3.5.2. Fourier Transform Infrared (FTIR) Spectroscopy FTIR	50
3.5.3. Scanning Electron Microscopy (SEM)	51
3.5.4. Inductively Coupled Plasma Mass Spectroscopy (ICP-MS)	51
3.6. Mechanical Properties	53
3.6.1. ASTM C633 Adhesion Testing	53
3.6.2. Fractography	56
Chapter 4 – Mathematical Model of Flame Spraying	57
4.1. Heat Transfer Estimation of Particle Temperatures during Deposition	57
Chapter 5 – Results and Discussion	62
5.1. Thermodynamic Estimation of Flame Temperature During Flame Spray Deposition	62
5.2. Characterization of Powder Feedstock Prior to Thermal Spraying	65
5.2.1. Particle Size Distribution (PSD)	65
5.2.2. X-ray Diffraction (XRD)	66
5.2.3. Powder Morphology	67

5.4. Characterization of Preliminary Coatings	70
5.4.1. Cross-sectional Optical Microscopy (CS-OM)	70
5.4.2. X-ray Diffraction (XRD)	72
5.4.3. Selection of a Powder Blending Ratio.....	77
5.5. Coating Characterization	78
5.5.1. Cross-sectional Optical Microscopy (CS-OM)	78
5.5.2. Glass Content and Porosity.....	91
5.5.2.1. Pore and Glassy Phase Size Distribution	99
5.5.3. X-ray Diffraction (XRD).....	111
5.6. <i>In Vitro</i> Bioactivity Assessment	121
5.6.1. Scanning Electron Microscopy (SEM) with Energy Dispersive X-ray (EDX) Spectroscopy	122
5.6.2. Fourier Transform Infrared (FTIR) Spectroscopy	128
5.6.3. Inductively Coupled Plasma Mass Spectroscopy (ICP-MS).....	134
5.6.4. Summary of <i>in vitro</i> Bioactivity Assessment	138
5.7. Mechanical Properties	140
5.7.1. Adhesion Testing and Fractography.....	140
5.8. Thermodynamic and Heat Transfer Modelling	154
5.9. Selection of the Most Promising Coating	161
Chapter 6 – Conclusions and Future Work	165
6.1. Conclusions	165
6.2. Future Work	171
Chapter 7 – References	173
Chapter 8 – Appendix: Drawings	183

List of Figures

Figure 1-1. Schematic representation of the Changing Landscape Coating system concept. The implant becomes integrated with bone tissue (osseintegrated) more and more with time as the bioactive glass resorbs; the interfacial area between implant and bone increases with time 4

Figure 2-1. Examples of orthodontic implants fabricated with and without a porous bone fixation region. Left (dense): Astra Tech (Molndal, Sweden) Right (porous): (IT1 Bonefit Institut Straumann, Waldenburg, Switzerland) (Reprinted and reproduced with permission from John Wiley and Sons Inc.) [5]. 11

Figure 2-2. Example of a titanium based total hip replacement system with porous bone fixation regions (Kobe Steel, Japan). (Reprinted and reproduced with permission from Elsevier Publishing Ltd.) [4]. 11

Figure 2-3. Scanning electron micrograph of the porous surface structure created by anodic oxidation of titanium. (Reprinted and reproduced with permission from Elsevier Publishing Ltd.) [4]. 12

Figure 2-4. Histological cross-sectional prepared from a porous Al₂O₃ implant after 8 weeks of implantation in a rabbit. The cross-section reveals the ingrowth of bone tissue that is characteristic of biological fixation. (Reprinted and reproduced with permission from John Wiley and Sons Inc.) [3]. 15

Figure 2-5 Comparison of the survivability of 2-10 years of class A bioactive glass and class B HA cone implants to maintain edentulous alveolar bone. (Reprinted and reproduced with permission from John Wiley and Sons Inc.) After: [2,15,26] 15

Figure 2-6 Schematic representation of the surface chemistry and surface charge changes responsible for HA formation on TiO ₂ . (Reproduced and reprinted with permission of Elsevier Publishing Ltd.) [4].	20
Figure 2-6. Generalized schematic of the thermal spray family of techniques.	25
Figure 3-1. Schematic representation of the experimental setup used for flame spraying.	38
Figure 3-2. Schematic representation of the dispersion and distribution of features throughout a microstructure. After [77].	45
Figure 3-3. Exploded view of one set of ASTM C633 Fixtures	53
Figure 3-4. Schematic representation of the bonded ASTM C633 fixture-substrate assembly.	55
Figure 5-1. Powder size distributions of the as-received metallic powders as measured by sieve analysis.	66
Figure 5-2. Powder size distribution of the as-received bioactive glass powder measured by sieve analysis.	66
Figure 5-3. X-ray diffraction patterns of the as-received feedstock powder.	67
Figure 5-4. a. SEM micrographs of the feedstock powder prior to thermal spray deposition. Images were taken in SE imaging mode; b. OM micrographs of coatings demonstrating reproducibility of coating morphology fabricated from < 45 μm Ti-6Al-4V alloy powder and 45 - 90 μm bioactive glass under the low flux condition from two different batches of Ti-6Al-4V powder; (left) lot 5573-S and (right) lot 236-L3.	69

Figure 5-5. Optical cross-sectional micrographs of the coatings produced with the preliminary powder blends. 72

Figure 5-6. X-ray diffraction patterns collected from the coatings fabricated from the preliminary powder blends. The weight percentage of bioactive glass is indicated to the right of the plot. 74

Figure 5-7. Representative optical cross-sectional micrographs of Ti-6Al-4V-based coatings sprayed under the low flux deposition condition. Arrow legend: Black – Bioactive glass; White – Epoxy-filled pore..... 80

Figure 5-8. Representative cross-sectional optical micrographs of Ti-6Al-4V-based coatings sprayed under the high flux deposition condition. Arrow legend: Black – Bioactive glass; Red – Reaction phase; White – Epoxy-filled pore..... 81

Figure 5-9. Representative cross-sectional optical micrographs of Cp-Ti-based coatings sprayed under the low flux deposition condition. Arrow legend: Black – Bioactive glass; Red – Reaction phase; White – Epoxy-filled pore 82

Figure 5-10. Representative cross-sectional optical micrographs of Cp-Ti-based coatings sprayed under the high flux deposition condition. Arrow legend: Black – Bioactive glass; Red – Reaction phase; White – Epoxy-filled pore 83

Figure 5-11. Schematic summary of the morphological and microstructural trends observed by optical microscopy. Each tile represents an individual combination of powder size, composition, and deposition condition. Legend: Metal - Small refers to < 45 μm powder and Large refers to 45 - 106 μm powder; Bioactive Glass: Small refers to 45 - 90 μm powder, Medium refers to 90 - 180 μm powder, and Large refers to 180 - 250 μm powder. 84

Figure 5-12. a. Optical cross-sectional micrographs of coatings deposited under the low flux condition demonstrating the presence of reaction phase (shaded red) for Cp-Ti-based coatings; b. Elemental mapping acquired by SEM with EDX localized around the glassy phase for coatings deposited under the low flux condition; c. Schematic representation of the glass morphology and reaction phase present within the microstructure for coatings deposited under the low flux condition 87

Figure 5-13. Schematic representation of the trends observed in the total porosity of the deposited coatings. Each tile represents an individual combination of powder size, composition, and deposition condition. Legend: Metal - Small refers to < 45 μm powder and Large refers to 45 - 106 μm powder; Bioactive Glass: Small refers to 45 - 90 μm powder, Medium refers to 90 - 180 μm powder, and Large refers to 180 - 250 μm powder. 92

Figure 5-14. Schematic representation of the trends observed in the total glassy phase content of the deposited coatings. Each tile represents an individual combination of powder size, composition, and deposition condition. Legend: Metal - Small refers to < 45 μm powder and Large refers to 45 - 106 μm powder; Bioactive Glass: Small refers to 45 - 90 μm powder, Medium refers to 90 - 180 μm powder, and Large refers to 180 - 250 μm powder. 83

Figure 5-15. Schematic representation of the trends observed in the portion of porosity with areas that would be suitable for the ingrowth of bone tissue. Each tile represents an individual combination of powder size, composition, and deposition condition. Legend: Metal - Small refers to < 45 μm powder and Large refers to 45 - 106 μm powder; Bioactive Glass: Small refers to 45 - 90 μm powder, Medium refers to 90 - 180 μm powder, and Large refers to 180 - 250 μm powder.....101

Figure 5-16. Schematic representation of the trends observed in the portion of glassy phase with areas that would be suitable for producing pores conducive to the ingrowth of bone tissue. Each tile represents an individual combination of powder size, composition, and deposition condition. Legend: Metal - Small refers to $< 45 \mu\text{m}$ powder and Large refers to $45 - 106 \mu\text{m}$ powder; Bioactive Glass: Small refers to $45 - 90 \mu\text{m}$ powder, Medium refers to $90 - 180 \mu\text{m}$ powder, and Large refers to $180 - 250 \mu\text{m}$ powder.102

Figure 5-17. Porosity distribution by area for Ti-6Al-4V-based composite coatings binned by order of magnitude. The top plots correspond to coatings fabricated from $< 45 \mu\text{m}$ metallic powder while the bottom plots correspond to coatings fabricated from $45 - 106 \mu\text{m}$ metallic powder. The relative frequency (number frequency) of features with areas in each size range is indicated above each bar.104

Figure 5-18. Porosity distribution by area for Cp-Ti-based composite coatings binned by order of magnitude. The top plots correspond to coatings fabricated from $< 45 \mu\text{m}$ metallic powder while the bottom plots correspond to coatings fabricated from $45 - 106 \mu\text{m}$ metallic powder. The relative frequency (number frequency) of features with areas in each size range is indicated above each bar105

Figure 5-19. Glassy phase distribution by area for Ti-6Al-4V-based composite coatings binned by order of magnitude. The top plots correspond to coatings fabricated from $< 45 \mu\text{m}$ metallic powder while the bottom plots correspond to coatings fabricated from $45 - 106 \mu\text{m}$ metallic powder. The relative frequency (number frequency) of features with areas in each size range is indicated above each bar110

Figure 5-20. Glassy phase distribution by area for Cp-Ti-based composite coatings binned by order of magnitude. The top plots correspond to coatings

fabricated from $< 45 \mu\text{m}$ metallic powder while the bottom plots correspond to coatings fabricated from $45 - 106 \mu\text{m}$ metallic powder. The relative frequency (number frequency) of features with areas in each size range is indicated above each bar.111

Figure 5-21. XRD patterns collected from coatings sprayed under the low flux condition.113

Figure 5-22. XRD patterns collected from coatings sprayed under the high flux condition.114

Figure 5-23. Schematic representation of the trends observed in the phase composition as a function of the manipulated variables. Each tile represents an individual combination of powder size, composition, and deposition condition. Legend: Metal - Small refers to $< 45 \mu\text{m}$ powder and Large refers to $45 - 106 \mu\text{m}$ powder; Bioactive Glass: Small refers to $45 - 90 \mu\text{m}$ powder, Medium refers to $90 - 180 \mu\text{m}$ powder, and Large refers to $180 - 250 \mu\text{m}$ powder.115

Figure 5-24. Phase diagram of the ternary $\text{CaO-TiO}_2\text{-SiO}_2$. Compositions are in weight percent and temperatures are given in $^\circ\text{C}$. Heavy lines are phase boundaries; fine lines are isotherms (dashes in both cases indicate uncertainty; Heavy dash-dot lines indicate boundaries of two-liquid region and letters refer to invariant points. The eutectic of interest corresponds to point P at 1365°C (reprinted and reproduced with permission from John Wiley and Sons Inc.) [103].120

Figure 5-25 Schematic representation of the results of the in vitro bioactivity assessment through SBF immersion testing of the coated substrates. Positive results are indicated with the time interval that HA formation was observed. Each tile represents an individual combination of powder size, composition, and deposition condition. Legend: Metal - Small refers to $< 45 \mu\text{m}$ powder and Large

refers to 45 - 106 μm powder; Bioactive Glass: Small refers to 45 - 90 μm powder, Medium refers to 90 - 180 μm powder, and Large refers to 180 - 250 μm powder.....122

Figure 5-26. . a. Representative time-lapse of SEM micrographs taken after SBF immersion in SE and BSE imaging mode of the $< 45 \mu\text{m}$ metallic powder blended with 45 - 90 μm bioactive glass coatings. White arrows correspond to hydroxyapatite and black arrows correspond to bioactive glass; b. Representative SEM micrographs of the cross-sectional morphology of the incorporated bioactive glass located at or near the top surface of the coating taken in BSE imaging mode (grey arrow indicates encapsulating layer surrounding bioactive glass particles). Left: $< 45 \mu\text{m}$ Ti-6Al-4V alloy blended with 45 - 90 μm bioactive glass; Right: $< 45 \mu\text{m}$ Cp-Ti blended with 45 - 90 μm bioactive glass.....124

Figure 5-27. Representative SEM micrographs of observed mineral layer formation taken after SBF immersion in SE and BSE imaging mode of the control coatings sprayed under the high flux deposition condition. The white arrows correspond to the surface layer.126

Figure 5-28. FTIR spectra collected from the control coatings fabricated under the high flux deposition condition after SBF immersion.....130

Figure 5-29. FTIR spectra collected from the control coatings fabricated under the high flux deposition condition after SBF immersion.....131

Figure 5-30. FTIR spectra collected from the Ti-6Al-4V-based composite coatings after SBF immersion.....132

Figure 5-31. FTIR spectra collected from the Cp-Ti-based composite coatings after SBF immersion.133

Figure 5-32. Aqueous concentrations of Ti, Al, and V in spent SBF solution collected after each 3 day cycle and measured by ICP-MS. Standard error was $\pm 0.1 \mu\text{mol/L}$ (Ti), and $\pm 0.04 \mu\text{mol/L}$ (Al, V).....137

Figure 5-33. Schematic representation of the trends observed in the mechanical bond strengths of the coatings. Each tile represents an individual combination of powder size, composition, and deposition condition. Legend: Metal - Small refers to $< 45 \mu\text{m}$ powder and Large refers to $45 - 106 \mu\text{m}$ powder; Bioactive Glass: Small refers to $45 - 90 \mu\text{m}$ powder, Medium refers to $90 - 180 \mu\text{m}$ powder, and Large refers to $180 - 250 \mu\text{m}$ powder.142

Figure 5-34. Composite plot of porosity and mechanical stress at coating fracture as a function of feedstock bioactive glass particle size distribution: a. coatings based upon $< 45 \mu\text{m}$ metallic powder; b. coatings based upon $45 - 106 \mu\text{m}$ metallic powder.....143

Figure 5-35. Schematic representation of potential failure modes in cross-section from ASTM Standard C633 tensile adhesion testing.143

Figure 5-36. Representative fractographs of failed control coatings after ASTM Standard C633 tensile adhesion testing taken by macrophotography. Failure mode type legend: 1. Coating-substrate adhesive failure, 2. Coating cohesive failure, 3. Coating-epoxy adhesive failure, 4. Epoxy cohesive failure, and 5. Epoxy-stub adhesive failure.144

Figure 5-37. Representative fractographs of failed composite coatings fabricated from $< 45 \mu\text{m}$ metallic powder after ASTM Standard C633 tensile adhesion testing taken by macrophotography. Failure mode type legend: 1. Coating-substrate adhesive failure, 2. Coating cohesive failure, 3. Coating-epoxy adhesive failure, 4. Epoxy cohesive failure, and 5. Epoxy-stub adhesive failure.....145

Figure 5-38. Representative fractographs of failed composite coatings fabricated from 45 - 106 μm metallic powder after ASTM Standard C633 tensile adhesion testing taken by macrophotography Failure mode type legend: 1. Coating-substrate adhesive failure, 2. Coating cohesive failure, 3. Coating-epoxy adhesive failure, 4. Epoxy cohesive failure, and 5. Epoxy-stub adhesive failure.....146

Figure 5-39. Representative optical micrograph of the substrate-coating interface in cross-section demonstrating a continuous interface that suggests metallurgical bonding has occurred. Image was taken from the 45 - 106 μm Cp-Ti-based control coating sprayed under the high flux deposition condition.146

Figure 5-40. Representative optical micrographs of the epoxy-side of the fracture surfaces. Black arrows indicate a translucent/transparent phase that may be bioactive glass. Micrographs demonstrate epoxy-cohesive failure, epoxy-coating adhesive failure, and coating cohesive failure. Left image: coating fabricated from < 45 μm Ti-6Al-4V alloy blended with 90 - 180 μm bioactive glass deposited under the low flux deposition condition; right image: coating fabricated from < 45 μm Cp-Ti blended with 45 - 90 μm bioactive glass deposited under the low flux deposition condition.....152

Figure 5-41. Thermodynamic reaction plots: a. Ellingham diagram of major oxides present within the system; b. Gibbs free energy and enthalpy of reaction for the reduction of alumina through the oxidation of Ti to TiO.....156

Figure 5-42. Theoretical particle temperatures attained during flame spray deposition as determined by heat transfer modeling.....159

Figure 5-43. Overall schematic indicating which coatings are the most suitable candidates for the changing landscape coating system on the basis of an overall assessment of the results from each analysis technique. Each tile represents an individual combination of powder size, composition, and deposition condition.

Legend: Metal - Small refers to $< 45 \mu\text{m}$ powder and Large refers to $45 - 106 \mu\text{m}$ powder; Bioactive Glass: Small refers to $45 - 90 \mu\text{m}$ powder, Medium refers to $90 - 180 \mu\text{m}$ powder, and Large refers to $180 - 250 \mu\text{m}$ powder. 164

List of Tables

Table 2-1. Examples of materials used in the human body by material classification. After [2,5,16].	7
Table 2-2. Categorization of tissue response to biomaterials. After [2-4,15].	8
Table 2-3. Stages in the class A bioactive response of 45S5 bioactive glass. After [2-4,25,26].....	18
Table 3-1. Summary of the experiments performed and models that were developed in this study.....	34
Table 3-2. Flame spraying conditions.....	38
Table 3-3. Preliminary powder blends examined.....	39
Table 3-4. 85:15 Powder blends used for flame spraying.....	40
Table 3-5. Coatings tested for bioactivity.. ..	50
Table 5-1. Gaseous composition used for modeling the fluid properties.....	64
Table 5-2. Summary of gaseous properties used for heat transfer modeling.	64
Table 5-3. Summary of porosity for control coatings.	95
Table 5-4. Summary of porosity and glassy phase content for the composite coatings.	97

Table 5-5. Common calcium phosphate minerals and the theoretical Ca/P ratio	125
Table 5-6. Time of surface layer formation as well as Ca/P ratio, if any, of the observed surface layer as determined by SEM.	125
Table 5-7. Summary of surface layer identification by FTIR of the coated titanium substrates after SBF immersion testing.	129
Table 5-8. Thickness and stress at failure of the thermally sprayed control coatings according to ASTM Standard C633 tensile adhesion testing.	148
Table 5-9. Stress at failure of the thermally sprayed coatings according to ASTM Standard C633 tensile adhesion testing.	142

List of Abbreviations

BG:	Bioactive Glass
BSE:	Backscattered Electron
CLC:	Changing Landscape Coating
Cp-Ti:	Commercially Pure Titanium
CS-OM:	Cross-sectional Optical Microscopy
EDX:	Energy Dispersive X-ray Spectroscopy
FTIR:	Fourier Transform Infrared Spectroscopy
HA:	Hydroxylapatite
HF:	High Flux
ICP-MS:	Inductively Coupled Plasma – Mass Spectroscopy
LF:	Low Flux
OM:	Optical Microscopy
PSD:	Particle Size Distribution
SE:	Secondary Electron
SEM:	Scanning Electron Microscopy
SBF:	Simulated Body Fluid
Ti-6Al-4V:	Titanium-6wt.% Aluminium-4wt.% Vanadium
XRD:	X-ray Diffraction

List of Symbols

A_s	Surface area of the particle (m^2)
Bi	Biot number, $Bi = \frac{hd_p}{6k_p}$
c_p	Specific heat capacity ($\text{J kg}^{-1} \text{K}^{-1}$)
d_p	Particle diameter (m)
F	F -test statistic
ΔG_f	Gibbs free energy change of formation (J)
ΔG_{rxn}	Gibbs free energy change of reaction (J)
h	Convective heat transfer coefficient ($\text{W m}^{-2} \text{K}^{-1}$)
ΔH_{rxn}	Enthalpy change of reaction (J)
k_g	Thermal conductivity of the carrier gas ($\text{W m}^{-1} \text{K}^{-1}$)
k_p	Thermal conductivity of the particle ($\text{W m}^{-1} \text{K}^{-1}$)
L_s	Stand-off distance (m)
L_x	Distance traveled by particle (m)
Ma	Mach number, $Ma = \frac{v_g}{\sqrt{\gamma RT_{\text{flame}}}}$
Nu	Nusselt number, $Nu = \frac{hd_p}{k_g}$
Pr	Prandtl number, $Pr = \frac{\mu_g c_p}{k_g}$
r	Recovery factor

R	Gas constant ($\text{J kg}^{-1} \text{K}^{-1}$)
Re_{d_p}	Reynolds number based on particle diameter, $\text{Re}_{d_p} = \frac{d_p (v_g - v_p) \rho_g}{\mu_g}$
s	Sample standard deviation
t_x	Time spent traveling by a particle
T	T -test statistic
T_{aw}	Adiabatic wall temperature (K)
T_{flame}	Adiabatic flame temperature (K)
T_0	Ambient temperature (K)
T_p	Particle temperature (K)
v_g	Gas velocity (m/s)
v_p	Particle velocity (m/s)
\bar{x}	Sample mean

Greek Symbols

γ	Specific heat ratio
μ_g	Viscosity of the carrier gas (Pa s)
ρ_p	Density of the particle (kg m^{-3})
ρ_g	Density of the carrier gas (kg m^{-3})
σ_f	Stress at failure of the coating (MPa)
Ω	Particle volume (m^3)

Chapter 1 – Introduction¹

1.1 Synopsis of Thesis

Alloys used in the construction of load-bearing implants are bio-inert, such as titanium or its alloys [1], while materials that are highly bioactive, such as bioactive glass, are brittle and possess an uncertain lifespan under load-bearing conditions. Therefore, there is a need to develop a bioactive composite material for load-bearing applications. The composite material should be mechanically stable, should have a porous structure conducive to tissue ingrowth, and should actively promote osteoblast attachment and proliferation. Biomedical implants intended for load-bearing applications such as bone-fixation, orthopedic, and orthodontic implants are often constructed of titanium or its alloys. For example, a common alloy used in these applications is Ti-6Al-4V alloy or Cp-Ti [1]. Titanium or titanium alloys are a natural choice for load-bearing applications due to their biocompatibility, high yield strength, and cyclical loading properties [1]. However, titanium is not bioactive and does not promote the differentiation of new osteoblasts, i.e., osteoproduction, or promote tissue attachment and implant integration, i.e., osteoconduction, without specialized surface treatment [2-4]. The lack of bioactivity can result in the failure of the load-bearing implant by the development of a fibrous capsule of tissue around the implant and premature loosening of the implant. The possibility of fibrous tissue encapsulation is of particular concern when there is significant micro-movement of the implant or the

¹A version of this chapter has been accepted for publication. Nelson 2013. Surface Innovations. A version of this chapter has been submitted for publication in Journal of Materials Science and Engineering – Part C.

surrounding tissue is unhealthy [1-3,5,6]. Therefore, it is clear that the bond between an artificial implant and human tissue is crucial to the long-term viability of the implant. Enhancement of the bonding is often necessary to ensure the success of dental and orthopedic implants. Other investigators have treated titanium to induce osteoconductivity [7-10], but even treated titanium will not actively promote the development of new tissue as it is not osteoproduative. Therefore, it is desirable to incorporate an osteoproduative compound to improve implant-tissue bonding.

Bioactive materials include ceramics such as 45S5 bioactive glass. 45S5 bioactive glass releases ions *in vivo* at a rate that invokes a cellular response [2,3]. The cellular response invoked by 45S5 bioactive glass actively promotes the development of new bone tissue, i.e., osteoproduativity, through signaling osteoprogenitor cells to differentiate into osteoblasts [2,3]. Additionally, 45S5 bioactive glass is absorbed and replaced with tissue over time *in vivo* [2,3]. However, 45S5 bioactive glass is a brittle ceramic that possess uncertain lifespan in load-bearing applications due to its brittle nature and the complex loading conditions that exist *in vivo*.

Therefore, a potential solution is to develop a new porous composite coating system with mechanical stability and osteoproduative capabilities. In this study, a porous coating of 45S5 bioactive glass and Cp-Ti or Ti-6Al-4V alloy was fabricated with flame spray deposition. Other studies have focused on preparing

coatings of HA, titanium, titanium alloys, titanium oxides, and composites of the aforementioned materials through air plasma spray (APS) and high-velocity oxyfuel (HVOF) spraying. However, APS and HVOF are more expensive and will result in a denser coating than oxy-acetylene flame spraying. A coating with a pore structure that is capable of supporting tissue ingrowth and the development of vascularization would be desirable. The greater mechanical interlock would further strength the bond between the artificial implant and surrounding tissue.

The concept presented herein is the production of a porous composite coating of titanium alloy and resorbable bioactive glass particulates that are partially encapsulated by the stronger and tougher titanium alloy in the coating (see Fig. 1-1). The structure can be described as a time-dependent bioactive glass porogen which will result in a "changing landscape coating" with time as the bioactive glass particulates dissolve during osseointegration (see Fig. 1-1). The bioactive glass initiates surface mineralization as it dissolves, leaving a metal-surrounded pore for tissue ingrowth that did not previously exist. The new pore will have an undercut keyhole-like shape and by its creation it will increase the mechanical interlocking of bone tissue with the implant provided the bioactive glass, and surrounding porosity, is sufficiently large to create a suitable pore structure with individual pore diameters of at least 40 to 80 μm [11,12]. Oxy-acetylene flame spraying will result in a coating that contains both larger pores and a higher degree of porosity than other thermal spray techniques such as HVOF or APS [13].

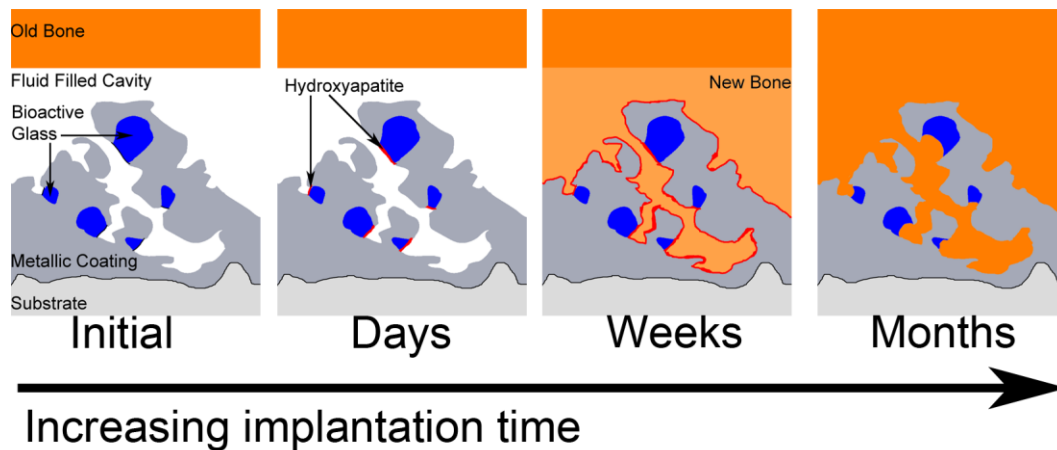


Figure 1-1. Schematic representation of the Changing Landscape Coating system concept. The implant becomes integrated with bone tissue (osseintegrated) more and more with time as the bioactive glass resorbs; the interfacial area between implant and bone increases with time.

The work presented herein focuses on establishing whether a coating with a structure suitable for a changing landscape coating (see Fig. 1-1) that provides an *in vitro* bioactive response can be created. Moreover, this work is focused on utilizing oxy-acetylene flame spraying to create changing landscape coatings as a proof of concept. Furthermore, assessment of the resorption of the bioactive glass would require an *in vivo* animal model in which cells would scavenge the necessary ions from the bioactive glass to create new bone tissue from the bioactive glass [2,14]. Therefore, assessment of the rate and degree of glass resorption is beyond the scope of this study.

The consequences the proportion of metallic powder to ceramic powder, the deposition conditions as well as the effects of the type of metallic matrix powder (i.e., commercially pure titanium (Cp-Ti) or Ti-6Al-4V alloy) are examined. Furthermore, the effects of altering the particle size distributions are explored.

The consequences of manipulating these parameters on the microstructure, coating porosity, phase composition, *in vitro* bioactivity, and tensile adhesion strength are explored from experimental measurements, as well as with theoretical heat transfer and thermodynamic modeling. Analysis and evaluation of the variables investigated herein were through quantitative cross-sectional optical microscopy (CS-OM), image analysis, X-ray diffraction (XRD), simulated body fluid (SBF) immersion testing, Fourier transform infrared (FTIR) spectroscopy, scanning electron microscopy (SEM) with energy dispersive x-ray (EDX) spectroscopy, and tensile adhesion testing.

1.1. Objectives

The research was conducted to develop the new changing landscape coating system with the following objectives in mind:

- Development of an understanding of how the ratio of metallic powder to ceramic powder, the type of titanium alloy, powder size distribution, and deposition conditions affects the microstructure, porosity, and phases that were formed in the coating;
- Determination of the effects of the aforementioned variables on the *in vitro* bioactivity of the composite coating by SBF immersion testing;
- Assessment of the tensile adhesion strength of the coatings, relating back to the aforementioned variables to allow for future optimization of the adhesion strength balanced with porosity for tissue ingrowth;

- Creation of a theoretical heat-transfer model to allow for prediction of in-flight particle temperatures as a function of deposition condition, particle size, and particle composition.

Chapter 2 – Literature Review

2.1. Biomaterials and Bioactivity

The term “biomaterial” is typically used to refer to a material that is suitable to replace damaged human tissue and is often constructed in the form of an implant [2,3,5,15]. Biomaterials envelope a wide range of materials and can be polymeric, ceramic, metallic, or a composite in nature [2,5,16]. A selection of materials that have been used in the human body is included in Table 2-1

Table 2-1. Examples of materials used in the human body by material classification. After [2,5,16].

Material Class	Examples
Metal	Gold Stainless Steel Titanium Zirconium Tantalum
Ceramics	Bioactive glasses Hydroxylapatite Titania Alumina
Polymers	Polyethylene Polylacticacid
Composites	Ti-HA Polyethylene-HA

2.1.1. Tissue Fixation, Bioactivity, and Implants

The suitability of a given material depends on how it interacts with the human body and the healing process. Ideally, a biomaterial is designed to have a specific reaction in the human body [5]. Hench [2,15], a world leader in the development of biomaterials, classifies biomaterials based upon the characteristic tissue response which can be divided into four distinct classes. The first three responses

(see Table 2-2) [2-4,15] will be discussed in detail here. However, it should be noted that many materials exhibit a combination of responses.

Table 2-2. Categorization of tissue response to biomaterials. After [2-4,15].

Response Type	Method of Attachment	Material Characteristics	Examples
1 (bio-inert)	Bone ingrowth into surface irregularities (morphological fixation).	Dense, nonporous, inert materials	Alumina Zirconia Ti Stainless Steel
2 (porous ingrowth)	Bone ingrowth into internal pores (biological fixation)	Porous, inert, materials	Porous Ti
3 (bioactive)	Direct chemical bonding (bioactive fixation)	Surface reactive materials that promote tissue attachment	Bioactive Glasses Dense HA
4 (resorbable)	Living tissue replaces the biomaterial at a gradual rate	Materials that dissolve at a rate to facilitate tissue replacement	Bioactive Glasses

2.1.1.1. Bio-inert Implants

The first type of tissue response belongs to a group of materials termed bio-inert [1,2,4,5]. Here, the tissue attaches passively to the implant surface by growing into any surface irregularities. Fixation by growth into surface irregularities is termed morphological fixation and is often the dominant mechanism for inert metals and ceramics such as dense titanium. As such, materials that achieve morphological fixation lack chemical and biological bonding. This deficit allows for both relative movement between tissue and the development of non-adherent fibrous tissue. To combat this shortcoming, it is common for the implant to be loaded compressively [2]. However, if the surrounding tissue is unhealthy, if non-adherent fibrous tissue develops, and/or if there is significant movement of the

implant relative to the surrounding tissue then these factors will eventually lead to the failure of the implant [1-3,5,6]. However, most materials commonly used for load-bearing applications are dense materials that exhibit only morphological fixation [1].

Porous materials exhibit the second tissue response in which the surrounding tissue grows into the internal porosity of the material. In this application the ingrowth of bone tissue is of interest. Tissue attachment through the ingrowth of bone tissue into porosity is termed biological fixation and relies on the increased contact area between the biomaterial and the surrounding tissue; biological fixation is the dominant mechanism for porous implants such as porous titanium [1,2,5]. As such, materials that achieve biological fixation lack chemical and biological bonding but have a reduced probability of developing non-adherent fibrous tissue due to movement of the implant relative to the surrounding tissue [1,2,5].

However, there is some debate regarding what range of pore size will encourage the ingrowth of bone tissue as well as the development of vascular tissue necessary to maintain long-term viability of the implant. The studies reviewed by Hench [2] showed that the pores must be greater 100 - 150 μm in diameter to allow for the development of vascular tissue to support ingrown bone tissue, while a study by Klenke *et al.* [11] demonstrated that a pore size of 80 μm in diameter with neck diameters of 20 μm allowed for significant ingrowth of bone

tissue and the development of supporting vascular tissue. Additionally, a study reviewed by Ellingsen [5] found that some ingrowth of bone tissue and some development of vascular tissue occurred with pore diameters in the 10 to 40 μm range. Furthermore, a study by Underwood *et al.* [12] found that the development of vascular tissue occurred for the ingrowth of epidermal tissue with pores sizes between 40 and 60 μm for polymeric scaffolds. It is worth noting that the material utilized in the latter cases exhibited a type 3 tissue response while the former did not. In any case, the presence of pores in the 10 to 100 μm diameter range are beneficial for encouraging tissue ingrowth into a porous implant.

Porous implants that are suitable for facilitating biological fixation are often constructed from a bulk porous material or treated in some manner to obtain a porous surface [2,4,17-19]. Common fabrication methods of porous implants include: utilization of a bulk porous material (often obtained through powder metallurgy) [2,4,17-19], chemical or electrochemical treatment of the implant surface to generate a macroporous structure [2,4,17,18], or application of a porous material through a coating technique [2,4,17,18]. However, porous coatings currently used in clinical applications are often monolithic metals or ceramics applied through techniques such as plasma spray, diffusion bonding, electrochemical treatment, or direct sintering of powder onto the implant surface [17,18,20]. Examples of load-bearing bone fixation implants with porous fixation regions surfaces are included in Fig. 2-1 [5] and 2-2 [4]. The microscopic structure of the porous surface is designed with pore diameters in excess of 40 μm

to facilitate the ingrowth of bone tissue as previously discussed. For example, a scanning electron micrograph of the surface structure of anodically oxidized titanium is included in Fig. 2-3 [4] and a histological cross-section of a porous Al_2O_3 implant that underwent tissue ingrowth with pore diameters in excess of $100\ \mu\text{m}$ has been included in Fig. 2-4 [2].

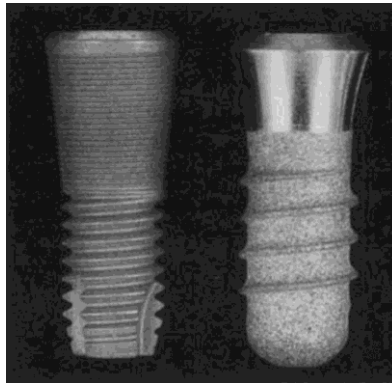


Figure 2-1. Examples of orthodontic implants fabricated with and without a porous bone fixation region. Left (dense): Astra Tech (Molndal, Sweden) Right (porous): (ITI Bonefit Institut Straumann, Waldenburg, Switzerland) (Reprinted and reproduced with permission from John Wiley and Sons Inc.) [5].

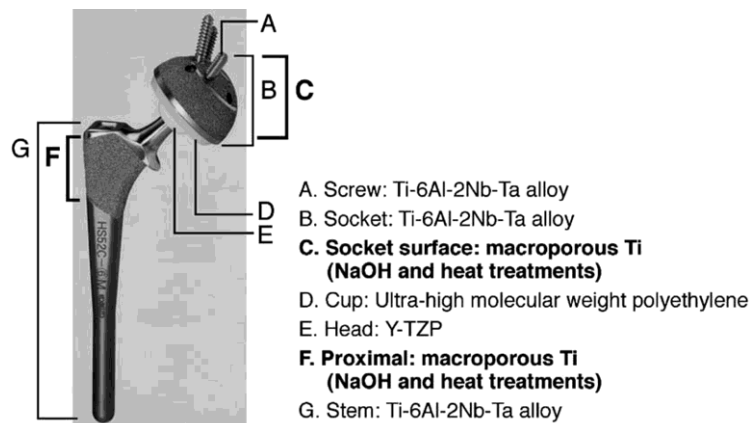


Figure 2-2. Example of a titanium based total hip replacement system with porous bone fixation regions (Kobe Steel, Japan). (Reprinted and reproduced with permission from Elsevier Publishing Ltd.) [4].

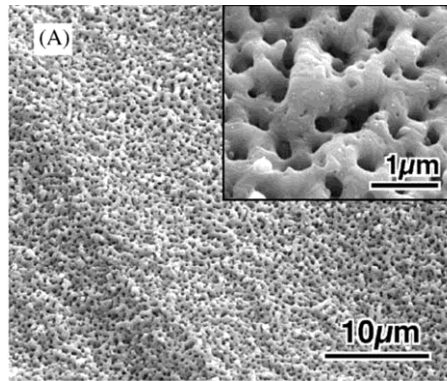


Figure 2-3. Scanning electron micrograph of the porous surface structure created by anodic oxidation of titanium. (Reprinted and reproduced with permission from Elsevier Publishing Ltd.) [4].

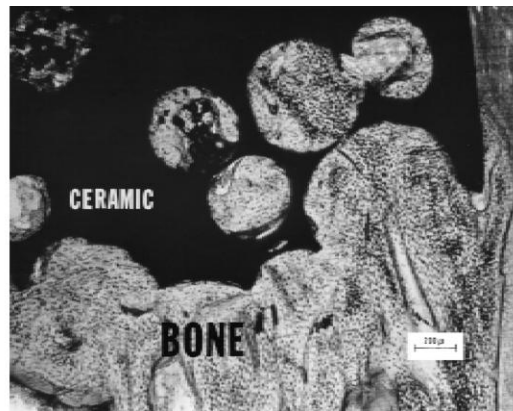


Figure 2-4. Histological cross-sectional prepared from a porous Al_2O_3 implant after 8 weeks of implantation in a rabbit. The cross-section reveals the ingrowth of bone tissue that is characteristic of biological fixation. (Reprinted and reproduced with permission from John Wiley and Sons Inc.) [2].

However, failure of porous implants can occur, despite the increased stability provided by the porous bone fixation regions, through loosening of the implant via micro-movement; such movement can result in the death of the ingrown tissue and the loss of interfacial stability leading to implant failure. The probability of failure can be reduced by including a compound with a type 3 tissue response (see Table 2-2), a bioactive material [2]. It should be noted that some coatings applied to porous implants are ceramics, such as bioactive glass, or hydroxyapatite, that exhibit a type 3 response [4,17,20]. However, these ceramic coatings are

mechanically fragile and possess uncertain lifespan in the complex mechanical loading conditions present in load-bearing applications. Therefore, incorporating a compound that exhibits a type 3 tissue response into a tougher porous matrix would represent a means of enhancing implant viability. Furthermore, the importance of a direct tissue-implant bond is underlined as the tissue-implant interface is often the point of failure in clinical practice with bio-inert materials [2].

2.1.1.2. Bioactive Implants

Materials that exhibit a type 3 response (see Table 2-2) are termed bioactive. In contrast to materials that are bio-inert, bioactive materials demonstrate surface reactivity that allows for the formation of a direct bond between the tissue and artificial material. Bioactive materials can be subdivided into two classes based upon their specific reaction with the human body, termed class A and B [2,3]. The distinction between classes is based upon how the osteoblasts respond to the material. Materials that exhibit class A bioactivity promote both osteoconduction and osteoproduction, while only osteoconduction is observed for a class B bioactive material. The fundamental difference that gives rise to each class is the ability of a given material to produce the critical ionic concentrations and release rates necessary to stimulate the production of new osteoblasts [2,3]. These concentrations and rates act as chemical stimuli for osteoprogenitor cells to undergo mitosis and cell differentiation. If the critical concentrations and release rates of soluble Si, P, Na, and Ca ions are present, then a genetic response resulting in the active promotion of new bone growth is observed

(osteoproduction) [3]. If no such environment exists, then bone migration along the interface is observed (osteoconduction) as only the cells directly in contact will bond to the implant. Class B biomaterials that have been investigated include dense HA and metallic oxides including: titanium, zirconium and tantalum [3,4,8,21,22]. Class A biomaterials consist of bioactive glasses and ceramics that are capable of providing the desired chemical environment [3]. For example, the first class A bioactive material, 45S5 bioactive glass, was developed by Hench *et al.* [23]. This development prompted early work by Greenlee *et al.* [24] and Beckham *et al.* [25] that confirmed that the bioactive glass family developed by Hench actively promoted the bonding between artificial material and hard tissue.

The importance of achieving a class A bioactive response in load-bearing dental implants was demonstrated by Stanley *et al.* [2,15,26], wherein cones of bioactive glass and HA were prepared for endosseous ridge maintenance implants (ERMI). These implants were intended to preserve the jawbone in patients who have had teeth extracted prior to being fitted for dentures. It was demonstrated (see Fig. 2-5) [2,15,26] that the bioactive glass implants exhibited a much greater survivability over a ten year period. As such, a class A bioactive response is desired for a changing landscape coating.

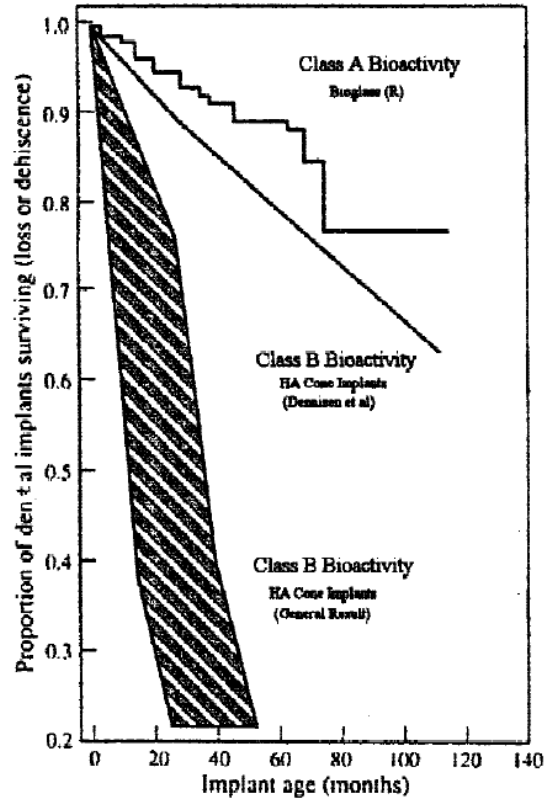


Figure 2-5. Comparison of the survivability of 2-10 years of class A bioactive glass and class B HA cone implants to maintain edentulous alveolar bone. (Reprinted and reproduced with permission from John Wiley and Sons Inc.) After: [2,15,26]

The two most common bioactive ceramic materials are 45S5 bioactive glass and HA [2-4]. Both of these materials promote cell attachment and growth along the implant surface, that is, osteoconduction. However, 45S5 bioactive glass releases ions *in vivo* at a rate that invokes a cellular response [2,3]. Additionally, 45S5 bioactive glass is absorbed and replaced with tissue over time *in vivo* [2,3]. However, dense HA may neither be osteoproliferative nor stable over the long term [2,3]. A study by Lai *et al.* [20] found that HA-coated acetabular cups in total hip-replacement implants led to approximately 38% of the patients requiring surgical revision due to radiological instability of the implants within ten years. However, both of these materials are brittle ceramics that possess uncertain lifespan in load-

bearing applications due to the complex loading conditions that exist *in vivo*. But, the definite osteoproduktivity and the greater long term viability suggest that 45S5 bioaktive glass is a superior choice to HA. Furthermore, preparing a composite of titanium or a titanium alloy and 45S5 bioaktive glass represents an alternative to using bio-inert titanium for load-bearing applications. Incorporation of the osteoproduktive resorbable bioaktive glass into a porous structure of titanium will allow for the development of a changing landscape coating.

2.1.2. Mechanism of Bioaktive Response and Assessment of Bioaktivity

The mechanisms leading to both direct chemical and biological bonding in bioaktive materials have been extensively studied. The mechanisms between class A and B bioaktive materials differ by the rate new which new bone is formed; class A bioaktive materials produce new bone rapidly, while class B bioaktive materials do so much more slowly due to the dramatically lower number of osteoprogenitor cells undergoing differentiation and mitosis into osteoblasts [3]. The mechanisms for three common biomaterials will be discussed here. They are 45S5 bioaktive glass, titania (TiO₂), and HA.

2.1.2.1. Bioaktive Glass

In the case of 45S5 bioaktive glass the mechanism involves twelve distinct reaction stages [2-4,27,28] (see Table 2-3), which differs from class B bioaktivity in the time it takes for the reaction stages 8 to 12 to occur. These stages (see Table

2-3) consist of both acellular and cellaur steps. The first five stages do not actually depend on the presence of cells to occur, hence the development of an acellular simulated body fluid (SBF) for *in vitro* testing by Kokubo *et al.* [28,29]. The use of SBF has received some criticism as the solution is highly saturated with respect to apatite and that the testing conditions do not reflect the stress states present *in vivo*, but it still remains an accepted technique [30]. The goal of SBF testing is to assess if HA forms *in vitro* on a given material; the presence of HA is confirmed by a combination of two or more of the following techniques: SEM, XRD, and FTIR [4,8,9,16,27-29,31-43]. Studying stages 6 through 12 requires the use of cell cultures or *in vivo* testing. SBF testing has also been used to study factors such as roughness, and porosity that could influence the ability for bone attachment to occur [11,36,44,45]. Based on the above studies, bioactivity was investigated through SBF testing and the presence of HA confirmed with a combination of SEM and FTIR.

Table 2-3. Stages in the class A bioactive response of 45S5 bioactive glass. After [2-4,27,28].

Log Time [h]	Stage	Surface Reactions
< 1	1	Ion exchange with body fluid
	2	Formation of Si-OH bonds
	3	Condensation of Si-OH groups to Si-O-Si
1	4	Adsorption of amorphous Ca + PO ₄ + CO ₃
2	5	Crystallization of hydroxyl carbonate apatite (HCA)
	6	Adsorption of biological moieties in HCA layer
20	7	Action of macrophages
	8	Attachment of osteoprogenitor cells
	9	Differentiation of osteoprogenitor cells into osteoblasts
100	10	Generation of collagen matrix
	11	Crystallization of matrix
	12	Proliferation of bone

Another key issue is the degree of crystallinity of bioactive glass. An *in vitro* study by Peitl *et al.* [27] found that increasing the degree of crystallinity retarded the rate of bioactive response. The authors found that HA precipitation occurred 30 hours later for crystallized bioactive glass than for amorphous glass. Other studies have also found similar trends [4]. Work by Nychka *et al.* [46] found that crystallization modified the dissolution rate of bioactive glass in a complex manner that may lead to a distribution of dissolution rates as a function of crystallographic orientation. This may retard or perhaps even prevent the osteoproduktivity capacity of the bioactive glass. But, early work by Hench and Greenlee indicated that the crystallinity did not significantly alter the final *in vivo* response [23,24]. However, an amorphous structure will be desired for the bioactive glass to ensure preservation of the dissolution rates that lead to the osteoproduktive capability.

2.1.2.2. Titanium and Titanium Dioxide (TiO₂)

Titanium has been shown to be osteoconductive, but not osteopductive, after specialized surface treatment [2-4]. The osteoconductivity has been shown to be due to the presence of a crystalline layer of titanium dioxide (TiO₂) [2-4]. TiO₂, specifically anatase, has been shown to be an effective class B bioactive material. Work conducted by Uchida *et al.* [47] found that sol-gel derived anatase can form HA in SBF, while rutile can to a lesser degree, but amorphous titania (TiO₂) does not. Another study by Lindgren *et al.* [37] found the same trend for furnace oxidized titanium and PVD deposited titania. These results suggest a very strong structural and stereological dependence on the bioactivity of non-soluble class B materials. To explain this dependence a mechanism has been suggested for the response based on the aligned –OH groups present on the oxide surface (see Fig. 2-6 [4]). The first stage of the mechanism involves the formation of hydroxide surface groups aligned in a manner conducive to the development of HA. The formation of hydroxide surface groups results in a negative surface charge; the negative surface charge attracts positive calcium ions from the surrounding body fluid resulting in the formation of an amorphous calcium titanate. The attraction of calcium ions continues until the overall surface charge is positive. At this point, negative phosphate ions are attracted to the material surface resulting in the formation of amorphous calcium phosphate. The formation of amorphous calcium phosphate results in the formation of apatite [4,31]. This mechanism is supported by zeta-potential studies conducted on TiO₂ surfaces immersed in SBF by Himeno *et al.*[31] An interesting corollary of the stereological mechanism is that

any material that produces an oxide with an appropriate structure can undergo this process, such as zirconia, tantalum and niobium [4]. The stereological mechanism for class B bioactivity also explains why HA formation is not observed on amorphous titania despite the high prevalence of $-OH$ groups [4].

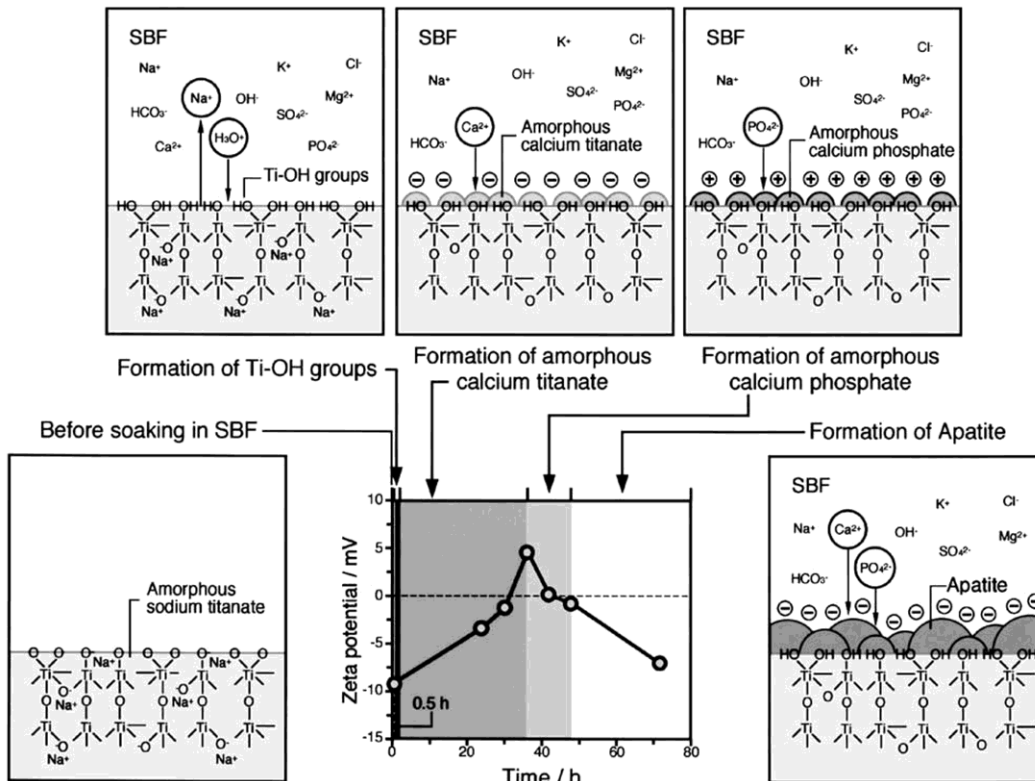


Figure 2-6. Schematic representation of the surface chemistry and surface charge changes responsible for HA formation on TiO_2 . (Reproduced and reprinted with permission of Elsevier Publishing Ltd.) [4].

Further research has been conducted to develop innovative approaches to induce bioactivity of titanium such as anodizing titanium [9], treatment of titanium in sodium hydroxide solutions [7,48] and plasma oxidation of titanium [10]. These techniques have successfully resulted in apatite formation *in vitro*. In order to justify the use of a coating over the above techniques, the proposed coating must

demonstrate the potential for better bonding through tissue ingrowth, rapid formation of HA, and an osteoproliferative class A bioactive response.

2.1.2.3. Hydroxyapatite (HA)

The bioactive response of HA is derived from a continuous process of dissolution and re-precipitation where the artificial HA interacts with the HA present within natural bone. On immersion in SBF, SEM/EDX studies have shown that the Ca/P ratio of the artificial HA varies over time [4]. Initially the ratio is 1.67 and quickly increases to 1.87 within three hours; this is followed by a more gradual decrease to 1.41 over the next six hours. At that point, the Ca/P ratio slowly increases to 1.65. Zeta potential measurements have confirmed that HA undergoes a very similar sequence of surface charge changes as that of titania [4]. HA selectively combines with calcium ions in the first stage which is followed by combination with phosphate ions to form metastable calcium phosphate. Calcium phosphate converts over time to bone-like apatite. An interesting note is that a relationship between the degree of densification and bioactivity exists; that is, as HA approaches full densification the bioactivity decreases owing to the larger initial negative surface charge observed [4]. Also, from a thermodynamic and kinetic perspective, the dissolution and precipitation mechanism introduces some limits on the applications for which HA can be utilized. That is, under high levels of cyclic stress as in high wear applications, such as coating of acetabular cups in hip implants, there is a marked problem with the dissolution of HA occurring more rapidly without a corresponding increase in the rate of re-precipitation resulting in

implant failure at an unacceptable rate regardless of tissue health as demonstrated in a study by Lai *et al.* [20]. The premature failure of the acetabular cups suggests that the HA is not capable of maintaining stability in that application. A study by Overgaard *et al.* [49] examined the effects of different loading conditions on the stability of HA. A coated implant was surgically installed into a dog femur. Three different groups of dogs were tested: a control group, a group continuously loaded, and a group immobilized after four weeks. A marked increase in HA resorption was found in the continuously loaded case. However, the drawbacks of HA may be overcome by selection of bioactive glass as previously described.

2.1.2.4. Implant Topography

In addition to the bioactive response, several very important considerations for implant longevity and stability are topography and roughness [5,6,44]. The effects of topography and roughness are complex. A review by Packham [50] discusses the fundamental effects of surface roughness, surface topography and surface energy on wetting and adhesion. After moderate deviation from a plane surface, a roughness factor is meaningless as it does not take into account the lateral characteristics of a surface. It is suggested that a fractal parameter should be used instead [50,51]. The fractal analysis provides a more physically meaningful measure of the deviation from an ideal plane as well as the degree of order within the structure. A surface that provides good adhesion would be well-ordered with a high surface area [50,51]. This fractal approach has been used successfully to study both coating adhesion and the stability of biomedical implants [51-54].

Further evidence regarding the important of implant roughness was found by Kwahara *et al.* [44]. The authors found that increasing the final roughness of the implant positively affected the rate at which bone formation occurred. These findings suggest that a fractal analysis should be employed as an avenue of future work for optimizing the proposed coating.

2.2. Thermal Spray and Biomedical Coatings

The limitations of using monolithic forms of both class A and B bioactive materials have led to the development of composites and coatings. One of the earliest uses of bioactive glass as an implant coating was performed by Greenspan and Hench [14] utilizing a coating and firing technique with alumina implants. It was found that coating the implant with 45S5 bioactive technique did not compromise the bioactivity of the glass, nor did it severely limit the flexural strength of the alumina. However, it has been noted that the fatigue lifespan of bioceramic materials under the complex loading conditions present in clinical practice is quite uncertain [2]. After the success of initial work, many other coating techniques have been used to deploy both class A and B bioactive compounds as coatings and composites. An alternative to inducing bioactivity through surface treatment of titanium implants would be to deposit a bioactive surface layer using a thermal spraying technique. Thermal spraying techniques take a feedstock material, typically a powder, and heat it in a high-temperature flame or plasma. The particles are often carried into the torch by an inert carrier gas such as argon or nitrogen. The particles pass through the torch and enter the high temperature flame or plasma and are melted or softened, accelerated, and deposited on a prepared substrate to produce a coating that is built up layer by layer. A general schematic of the thermal spray process is included in Fig. 2-7. In the reviewed studies, the feedstock for thermally sprayed coatings have been prepared in a variety of ways, including slurry coating [21,55], sintering followed by grinding [41], mechanical alloying [21], and simple blending [56].

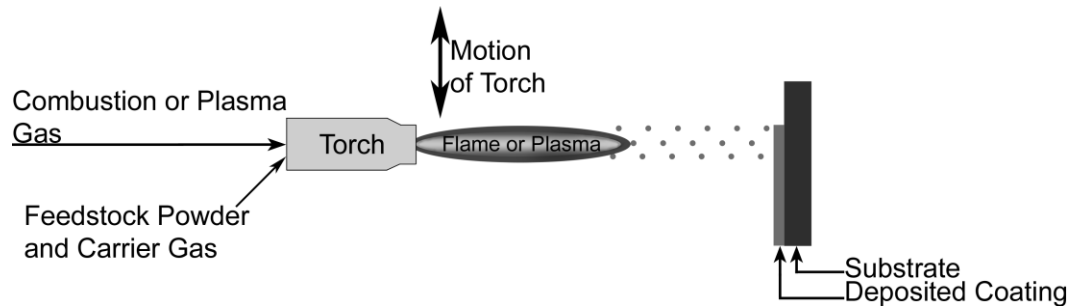


Figure 2-7. Generalized schematic of the thermal spray family of techniques.

The bioactive compound can be deployed as a single component coating or as a bioactive phase in a composite coating. Other studies have focused on preparing coatings of HA, titanium, titanium alloys, titanium oxides, and composites of the aforementioned materials. Techniques that have been used include but are not limited to: air/vacuum plasma spray (APS and VPS) [21,41,42,49,55,57-62], high velocity oxy-fuel spray (HVOF) [21,36,45,56,63-67], chemical treatment [7], and micro-arc oxidation [22]. However, these techniques are more expensive and will result in a denser coating than that produced by oxy-acetylene flame spraying [13]. Flame spraying is a process in which the combustion of acetylene (C_2H_2) in oxygen (O_2) produces a high-temperature flame that facilitates melting, acceleration, and deposition of particles to produce a coating as in Fig. 2-7. Flame spraying produces flame temperatures on the order of 3000 to 3400 K [13,68] depending upon the gaseous flow rates used. Metallic particles normally attain velocities between 15 and 30 m/s [68]; however, higher velocities are likely possible for particles with lower densities such as ceramics. In contrast, techniques such as APS produce plasma temperatures in excess of 4000 K [13] and metallic particles attain velocities in excess of 70 m/s [69]. Therefore, owing

to the lower temperatures and velocities attained during flame spraying the coatings produced tend to be more porous [13].

A coating with a pore structure that is capable of supporting tissue ingrowth and the development of vascular tissue is desirable [11,12]. The greater mechanical interlock would further strengthen the bond between the artificial implant and the surrounding tissue. The use of a composite coating is particularly attractive as it can potentially produce properties that are tailored to a given application [2]. A composite coating that consists of a blend of resorbable bioactive glass incorporated into a matrix of titanium or titanium alloy may provide an appropriate solution for load-bearing implants. The bioactive glass will initiate surface mineralization and provide an osteoproliferative response during the osseointegration of the coating. Additionally, with increasing time of implantation the bioactive glass will dissolve thereby acting as a time-dependent porogen which will result in a changing landscape coating with time during osseointegration. The newly created metal-surrounded pore is available for tissue ingrowth after the dissolution of the bioactive glass. The new pore will have an undercut keyhole-like shape and the creation of the pore will increase the mechanical interlocking of bone tissue with the implant provided the bioactive glass, and surrounding porosity, is sufficiently large to create a suitable pore structure with individual pore diameters of at least 40 to 80 μm [11,12]. Oxy-acetylene flame spraying will result in a coating that contains both larger pores

and a higher degree of porosity than other thermal spray techniques such as HVOF or APS [13].

The literature shows that extensive work has been conducted with APS/VPS and HVOF. The work done thus far seems to focus on class B bioactive materials and to some extent composites of class A or class B materials with bio-inert materials. The present contribution of this thesis work is new as little to no other work has been conducted on preparing a composite coating of bioactive glass blended with titanium or a titanium alloy by flame spray. The contribution of a changing landscape coating represents a new coating system.

2.3. Mechanical Assessment of Thermally Sprayed Coatings

The measurement of coating properties presents a challenge as it is very difficult to separate the properties of the substrate from the properties of the coating. As such, properties are commonly investigated using: microhardness [36,41,55,56,65,66], tensile adhesion strength [36,55,56,70,71], shear strength [41,70], three and four point bending [14,42,72,73], single notch bending [58], and interfacial indentation adhesion [70,71]. Thermally sprayed coatings, including those intended for bone fixation applications, are most commonly assessed with one of two adhesion tests: tensile adhesion testing, according to ASTM Standard C633 [74], or interfacial indentation testing [70,71]. Other studies have tested monolithic and composite coatings produced with HVOF [21,36,67] or APS [55,57,58,62] with tensile adhesion testing that were intended for bone-fixation applications. For instance, Tsui *et al.* [58] examined the adhesion strength of HA sprayed on Ti-6Al-4V alloy substrates with APS with the most promising coating adhesion strength reported at 14 ± 2 MPa ($n = 3$).

In the thermal spray community, ASTM Standard C633 [74] is typically used for adhesion testing. However, there are many factors that can impact the accuracy of the result from the test standard. The first variable of note is the thickness of the coating. Hadad *et al.* [71] noted that the thickness of the coating has an effect on the residual stress state. As the coating thickness increases, the ASTM C633 adhesion strength decreases due to the residual coating stresses. However, it should be noted that the coatings described in that work were dense mono-

component coatings, not porous composite coatings. Additionally, another complication is that the epoxy may infiltrate the substrate-coating interface and artificially increase bond strength if the coating is insufficiently thick [70,71]. Furthermore, it is common for a mixed failure mode to be observed making isolation of the adhesive or cohesive strength difficult [71]. However, this test still remains an accepted means of characterizing bonding strength in the thermal spray community.

The limitations of ASTM C633 lead to the development of interfacial indentation adhesion testing. This test involves the use of a Knoop or Vicker's indenter, placed at the coating-substrate interface. This test better characterizes the ability of the interface to resist delamination. However, this test also does not take into account the cohesive properties of the coating, but it offers a good measure of the interfacial toughness [71]. However, due to the nature of the proposed coating, this test may be unsuitable; porosity of the coating and the unknown elastic modulus of the coating make for difficulties in interpretation of indentation data due to scatter.

Further, the factors that influence the mechanical properties of biomedical coatings are an area of key interest. One of the more obvious factors is the powder used to produce the coating. This effect is demonstrated through the extensive work by Lima *et al.* [36,64-66] on the properties of HVOF-deposited conventional fused-and-crushed titania (TiO_2), nano-structured TiO_2 , and nano-

structured HA. The authors found that higher adhesive strength (in excess of 70 MPa for nano-structured TiO₂ coatings), a greater degree of bioactivity, and more uniform properties were obtained by using a nano-structured powder. The size of the powder utilized will also have an effect on porosity due to the degree of particle melting. A study by Li *et al.* [67] examined the effects of particle size on the adhesion strength of HVOF-sprayed HA coatings. The authors found that the point of failure was often the interface between unmelted and melted portions of the particles that comprised the coating. It is conceivable that variation of the feedstock sizes, type of alloy, and deposition conditions could result in control over the degree of porosity as well as the mechanical properties of the coating, which gives motivation for this study.

2.4. Thermodynamic and Heat Transfer Modelling²

The mechanical properties of the coating have been shown to be a function of microstructural characteristics, particle melting state, phase composition, and deposition parameters [21,55,57,58,64,67]. Therefore, insight into the temperature and chemical nature of the torch flame jet as well as the temperatures achieved by the particle in flight is of importance in attempting to predict the final microstructure, mechanical properties, and phase composition.

One approach to predict the temperature and chemical environment of a high temperature flame or plasma is to utilize thermodynamic combustion analysis [13,75]. A study by Bandyopadhyay and Nylén [68] utilized a combination of thermodynamic combustion analysis and computational fluid dynamics to determine the properties of an oxy-acetylene flame jet and to estimate the particle temperatures. Dewar *et al.* [76] went further to propose a lumped capacitance heat transfer model to determine the degree of heating for a particle carried in a heated gaseous stream. Therefore, an estimation of the flame temperature, local chemical environment, and particle temperatures may be obtained by coupling a thermodynamic combustion analysis and lumped capacitance heat transfer model. If the local chemical environment and particle temperatures are known then the phases present within the coating can be predicted through thermodynamic analysis. One approach to determine the stability of oxides in a given chemical environment is to construct an Ellingham diagram. This approach is often

²A version of this section has been submitted for publication in Journal of Materials Science and Engineering - Part C

employed in metallurgical, oxidation, and thermal analysis work [77]. Further, if this diagram is paired with a known phase composition, then the absence or presence of a phase could be used to predict the particle temperatures and the reactions that occurred during deposition. In this study, an Ellingham diagram will be paired with a thermodynamic combustion analysis and lumped capacitance heat transfer model to validate the presence of observed phases.

Chapter 3 – Experimental Procedure³

3.1. Experiments

The experiments performed in this study were selected to accomplish the objectives outlined previously. For each objective a list of anticipated outcomes was developed and an experimental technique was selected to accomplish the outcome (see Table 3-1).

³A version of this chapter has been published in Nelson *et al.* [78] , “Flame Spray Deposition of Titanium Alloy-Bioactive Glass Composite Coatings”, *Journal of Thermal Spray Technology*, volume 20, issue 6, Dec 2011, pg 1339-1351.

Another version of this chapter has been accepted for publication. Nelson 2013. *Surface Innovations*.

A different version of this chapter has been submitted for publication in the *Journal of Materials Science and Engineering – Part C*

Table 3-1. Summary of the experiments performed and models that were developed in this study.

Objectives	Experimental Technique	Anticipated Outcomes
Characterization of feedstock materials	PSD XRD FTIR SEM	- Particle size distribution - Initial phase composition - Chemical bond identification - Particle morphology
Production and preliminary characterization of coatings produced with various powder blends	Flame Spray XRD CS-OM	- Porous composite coatings with tailored properties - Phase composition - Porosity and morphology of composite coatings
Production and characterization of produced composite coatings and controls	Flame Spray XRD CS-OM	- Porous composite coatings with tailored properties - Phase composition - Porosity and morphology of composite coatings
In-vitro bioactivity assessment	Immersion in SBF FTIR SEM ICP-MS	- HA formation - HA evolution - HA morphology and location - Dissolution of metallic ions
Mechanical property assessment	ASTM C633 Fractography	- Coating adhesion strength - Fracture surface characterization
Heat transfer and thermodynamic modelling	FactSage TM Derived Model	- Estimation of flame temperatures and combustion products - Estimation of particle temperatures during deposition

3.2. Feedstock Materials

The materials used in the fabrication of composite coatings consist of a substrate, a titanium powder, and a bioactive glass powder. The substrate used for all coatings was Grade 2 Cp-Ti plate purchased from McMaster-Carr (Chicago, IL, USA). However, two different thicknesses were necessary due to the different requirements for the ASTM C633 compliant mechanical tests [74]. For other experiments, titanium plate with a thickness of 1.59 mm (1/16") was used. But, in the case of the mechanical assessment a thickness of 3.18 mm (1/8") was required. The 1.59 mm plate was cut into 15 x 25 mm rectangular coupons using a slow speed saw (TechCut 4, Allied High Tech Products, Inc., Rancho Dominguez, CA, USA) operating at 200 rpm with a metal-bonded diamond wafering blade (Allied High Tech Products, Inc., Rancho Dominguez, CA, USA) cooled with a propylene glycol-based lubricant (Low Speed Cutting Fluid, Allied High Tech Products, Inc., Rancho Dominguez, CA, USA). The 3.18 mm thick plate was cut into 25.4 mm diameter circular coupons using a multi axis water jet cutter (OMAX 2652 abrasive water jet cutter, OMAX Corp., Kent, WA, USA) operating at 345 MPa (50 ksi) with #80 crushed garnet grit.

Two different compositions of titanium powder, Grade 23 Ti-6Al-4V alloy (6 wt. % aluminum, 4 wt. % vanadium, and 0.13 wt. % oxygen) and Grade 1 CP-Ti (0.13 wt. % oxygen, 0.05 wt. % iron, 0.02 wt. % carbon, and 0.01 wt. % nitrogen) were purchased in two different size ranges each. The titanium powder size ranges selected were less than 45 μm ($< 45 \mu\text{m}$) (Cp-Ti lot - 09-001 and Ti64 - lot

236-L3 & 5573-S) and 45 to 106 μm (- 106 + 45 μm) (Cp-Ti - lot 12-026 and Ti64 - Lot 12-055); this powder was supplied by Raymor Industries (Boisbriand, QC, Canada). However, one kilogram of Ti-6Al-4V powder sieved to the 45 to 106 μm size range was donated by Carpenter Technologies (45 to 152 μm , lot P1796, Woonsocket, RI, USA). This batch was deemed equivalent to the powder purchased from Raymor based on the SEM and XRD characterization. The titanium powders were sieved to remove both undersized and oversized fractions using a Ro-Tap powder sieve (RX-29-Can, W.S. Tyler, Mentor, OH, USA).

The bioactive glass used in this study was melt-cast derived 45S5 powder donated by Mo-Sci Healthcare (GL0160P, lot NA30MAY08, Rolla, MO, USA) with a size range of 106 to 710 μm (- 710 + 106 μm) and a nominal composition of: 45 wt. % SiO_2 , 24.5 wt. % Na_2O , 24.5 wt. % CaO , and 6 wt. % P_2O_5 . The bioactive glass powder was sieved to a size range of 106 to 212 μm (- 212 + 106 μm) with a Ro-Tap powder sieve for use in the powder blends used to manufacture the preliminary coatings. The as-provided bioactive glass was ball-milled with cylindrical alumina media (20.6-mm diameter Al_2O_3 , US Stoneware, East Palestine, OH, USA) for 5 h. After milling the glass was sieved to three size ranges, 45 to 90 μm (- 90 + 45 μm), 90 to 180 μm (- 180 + 90 μm), and 180 to 250 μm (- 250 + 180 μm), using a Ro-Tap powder sieve. The sieved bioactive glass was used for all subsequent work.

3.3. Thermal Spraying

3.3.1. Spray Conditions

An oxy-acetylene flame spray torch (6PII ThermoSpray Gun, Sulzer Metco Inc., Westbury, NY, USA) was operated under two sets of conditions, these conditions will be referred to as “high flux” and “low flux”. Table 3-2 includes the stand-off distance in addition to the flow rate of O₂, C₂H₂, and Ar for each deposition condition. The stand-off distance is the distance maintained between the torch and the substrate during deposition. Figure 3-1 includes a schematic representation of the flame spray setup with all equipment labeled. The flame spray torch was mounted on a robotic arm (HP20, Motorman Inc., West Carrollton, OH, USA) that operated at a constant velocity of 400 mm/s regardless of deposition condition. The number of torch passes was fixed at 10 for the preliminary coatings (see Table 3-3 in section 3.3.2) and at 5 for all further coatings. The powder feed rate was controlled by use of a volumetric powder feeder (5MPE Powder Feeder, Sulzer Metco Inc., Westbury, NY, USA) which was operated at 60 FMR (flow meter reading) for the coatings deposited with the preliminary powder blends and 90 FMR (flow meter reading) for all further coatings. The powder was agitated in the feeder by use of an air vibrator.

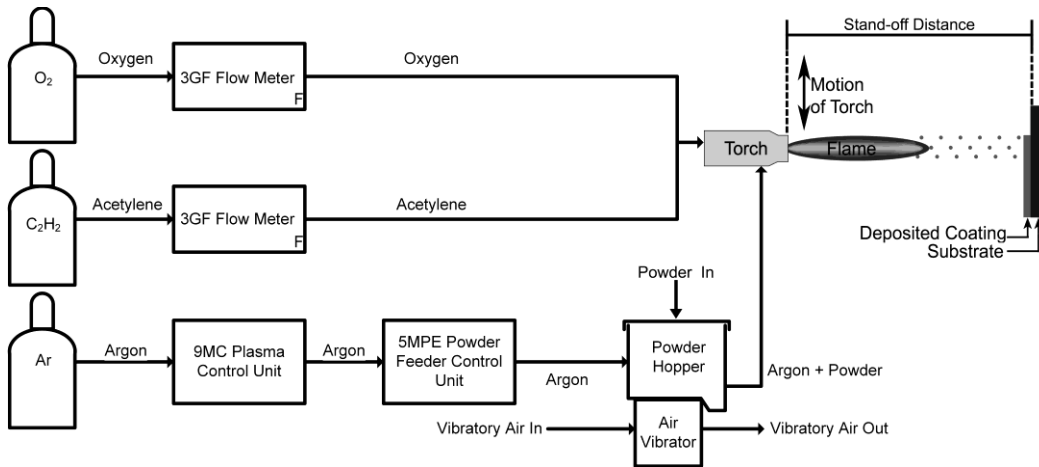


Figure 3-1. Schematic representation of the experimental setup used for flame spraying.

Table 3-2. Flame spraying conditions.

Deposition Condition	Oxygen Flow Rate [NLPM]	Acetylene Flow Rate [NLPM]	Argon Flow Rate [NLPM]	Stand-off Distance [mm]
Low Flux	25	15	9.5	150
High Flux	35	22	9.5	100

3.3.2. Powder Blending and Deposition

The cut titanium substrates were grit-blasted (Trinco Dry Blast, Trinco Tool Co., Fraser, IL, USA) with #24 grit alumina abrasive (686 μm Al_2O_3 , Treibacher Schleifmittel North America, Inc., Niagara Falls, NY, USA) in preparation for flame-spraying. The substrates were clamped to the substrate holder and residual contamination was removed with compressed air.

A preliminary analysis was conducted to establish the appropriate proportions of metallic to bioactive glass powder for flame-spray deposition. 45S5 bioactive glass (Mo-Sci Health Care, Rolla, MO, USA) powder (derived from a melt casting route) was sieved to a size range of 106 to 212 μm (- 212 + 106 μm) with a Ro-Tap powder sieve (RX-29-CAN, W.S. Tyler, Mentor, OH, USA). Two

blends of titanium alloy (Ti-6Al-4V) (5573-S, Raymor Industries, Boisbriand, QC, Canada) and 45S5 bioactive glass were prepared. To facilitate the blending of < 45 μm Ti-6Al-4V alloy and 106 to 212 μm bioactive glass powder, appropriate amounts (see Table 3-3) of each component were placed in a 1L Nalgene® polymeric bottle. The bottle was shaken end over end for 15 minutes. Additional mixing occurred in the volumetric powder feeder by using an air vibrator. Each blend was deposited with the oxy-acetylene flame spray torch on to the prepared titanium substrates under both deposition conditions.

Table 3-3. Preliminary powder blends examined.

Blend		Mass of Bioactive Glass [g]	Mass of Ti-6Al-4V [g]
Ti-6Al-4V [wt. %]	Bioactive Glass [wt. %]		
100	0	0	200
85 (78 vol. %)	15 (22 vol. %)	30	170
62 (50 vol. %)	38 (50 vol. %)	76	124
0	100	200	0

After the coatings deposited from the preliminary blends were studied, the Cp-Ti and Ti-6Al-4V alloy powders were each blended with 45S5 bioactive glass. The blending ratio was established at a metallic to ceramic powder ratio of 85:15 by weight by the preliminary analysis discussed above. Each Cp-Ti and Ti-6Al-4V alloy particle size distribution was blended with each 45S5 bioactive glass particle size distribution for a total of twelve different blends. Table 3-4 lists the various blends utilized in this study. Blending was accomplished in the manner described previously for the coatings fabricated from the preliminary powder blends.

Table 3-4. 85:15 Powder blends used for flame spraying.

Metallic Powder Size Range [μm]	45S5 Bioactive Glass Powder Size Range [μm]	Metal-based Powder
0 to 45	45 to 90	Cp-Ti Ti-6Al-4V
0 to 45	90 to 180	Cp-Ti Ti-6Al-4V
0 to 45	180 to 250	Cp-Ti Ti-6Al-4V
45 to 106	45 to 90	Cp-Ti Ti-6Al-4V
45 to 106	90 to 180	Cp-Ti Ti-6Al-4V
45 to 106	180 to 250	Cp-Ti Ti-6Al-4V

Each blend was deposited with the oxy-acetylene flame spray torch on to the prepared titanium substrates under both deposition conditions. Additionally, control coatings were also deposited by flame-spraying using both size ranges of Cp-Ti and Ti-6Al-4V alloy under both depositions conditions. The coated titanium substrates were stored in a desiccator cabinet (Secador, Fisher Scientific, Ottawa, ON, Canada).

3.4. Characterization

3.4.1. Particle Size Distribution (PSD)

The particle size distributions of the as-received and milled powders were characterized through a standard sieve analysis without sampling. That is, the entire quantity of powder was sieved rather than a small sample. This method was carried out with a Ro-Tap powder siever and sieves with the following opening sizes: 720, 600, 500, 354, 250, 180, 106, 90, 53, 45, 38, and 20 μm . Appropriate sieves were selected for each powder. For instance, sieves between 720 and 106 μm were used for the as-received 45S5 bioactive glass powder. The main result of this analysis was knowledge regarding the size distribution. However, because this method relies on the mechanical separation of powder it is the smallest dimension of each particle that is measured. While this does not make a difference for spherical powders, a powder with an angular or irregular morphology may appear to be smaller than in reality (as could be the case for the bioactive glass powder). Additionally, care was taken with the sieving time as too short a time would not result in proper separation and too long a time could result in the breakage of brittle particles from particle-particle and particle-sieve impacts.

3.4.2. Powder Morphology

An SEM (Evo MA 15, Carl Zeiss Inc., Toronto, ON, Canada) was used to characterize the morphology of the Cp-Ti, Ti-6Al-4V, and bioactive glass powders. The titanium powders were characterized as-received; the bioactive glass powder was characterized both as-received and after milling. The bioactive

glass powder was coated with gold (SEMprep II DC sputter coater, NanoTech, Prestwich, Manchester, UK), while no coating was necessary for the titanium powders. The powders were imaged in secondary electron (SE) mode with a LaB₆ filament operating at a voltage of 10 kV.

3.4.3. Metallurgical Preparation and Optical Microscopy (OM)

3.4.3.1. Preliminary Composite Coatings

The coated titanium substrates were mounted in cold-mount epoxy (EpoxySet, Allied High Tech Products Inc., Rancho Dominguez, CA, USA) and cured overnight (approximately 10 hrs). The epoxy-mounted samples were ground (TwinPrep 3, Allied High Tech Products Inc., Rancho Dominguez, CA, USA) with silicon carbide grit paper (SiC Grit Paper, Allied High Tech Products Inc., Rancho Dominguez, CA, USA). The grit sizes used were in the sequence 240, 320, 400, 600, 800, and 1200. The samples were polished (Imperial Polishing Pads, Allied High Tech Products Inc., Rancho Dominguez, CA, USA) with a diamond suspension (Polycrystalline Diamond Suspension Water-based, High Tech Products Inc., Rancho Dominguez, CA, USA). The diamond suspensions were used in the following particle size sequence: 3, 1, and 0.25 μm . The polished samples were cleaned with 5 mL of acetone and a line-free cloth (KimWipes, Kimberly Clark, Irving, TX, USA).

The polished samples were viewed with an optical microscope (Epiphot 300, Nikon Corporation, Markham, ON, Canada). Micrographs of a 626 x 416 μm area

(4288 x 2848 pixels) were taken with a digital camera (D300 Camera, Nikon Corporation, Markham, ON, Canada). The micrographs were taken in Brightfield mode (BF), with an exposure time of 5 ms. A total of 40 micrographs were taken (5 micrographs for each combination of sample composition and spray condition).

3.4.3.2. Cp-Ti and Ti-6Al-4V Alloy Composite Coatings

Metallurgical cross-sections of each coated titanium substrate were prepared for inspection by optical microscopy. The coated titanium substrates were mounted in a cold-mount two component low-viscosity epoxy (EpoFix, Struers A/S., Ballerup, Denmark) which was fluorescently dyed (EpoDye, Struers A/S., Ballerup, Denmark). Two different coatings taken randomly from the same flame spray deposition were mounted. The samples were infiltrated with epoxy by means of a vacuum pump (LAV-3, Fischer Technical, Roselle, IL, USA) to fill any surface-accessible pores. The vacuum pump was operated at a gauge pressure of -68 KPa. The epoxy was allowed to cure overnight (approximately 15 h). The epoxy mounted coatings were ground and polished using an identical procedure to that which was presented for the coatings fabricated from the preliminary powder blends (see section 3.4.3.1). However, grinding was accomplished with silicon carbide grit papers in the following progression: 240, 320, 600, and 1200.

An optical microscope (OM) (Axio Imager M2m, Carl Zeiss AG., Oberkochen, Germany) was used to view the polished cross-sections. All cross-sections were illuminated with a 100 W halogen bulb (HAL 100 Lamp, Carl Zeiss AG.,

Oberkochen, Germany) operated at a voltage corresponding to a colour temperature of 3200 K. Neutral density filters were required to decrease the light intensity to 1.5% due to the highly reflective nature of the samples. Additionally, all samples were viewed under a 50 W UV mercury discharge lamp (Excitation wavelength of 350 nm) (HBO 50 Lamp, Carl Zeiss AG., Oberkochen, Germany). Micrographs (Grayscale: 1388 x 1040 pixels; Colour: 2776 x 2080 pixels) of a 716 x 536 μm area were taken with a high dynamic range pixel-shifting digital camera (Axiocam HRc, Carl Zeiss AG., Oberkochen, Germany). Micrographs were acquired in the brightfield (BF) and ultraviolet fluorescent (UV FL) modes of operation. The UV FL images were used to identify pores filled with epoxy to aid in image analysis. Images were taken with a 20x objective and 10x eyepiece lens. Grayscale micrographs were utilized for image processing, whilst colour micrographs were used for qualitative comparison. The grayscale micrographs were deliberately overexposed to provide more details in the darker regions of the micrograph. A total of 12 grayscale and 5 representative colour micrographs were taken for each sample.

The representative colour micrographs were compared qualitatively, in a binary manner, to establish whether the bioactive glass and porosity was well distributed and well dispersed throughout the structure or poorly dispersed and distributed (see Fig. 3-2) [79]. The degree of dispersion and distribution of the bioactive glass and porosity was assessed qualitatively and was categorized as either well dispersed and well distributed or poorly dispersed and poorly distributed.

Coatings which exhibited well dispersed and well distributed bioactive glass and porosity were described as spatially homogenous. (Note: the effects of pre-selection of homogenous coatings versus non-homogenous coatings with respect to osseointegration would need to be studied in greater detail. The case here was made to be able to assess if the coating deposition method was capable of producing a particular pore size range and distribution – ultimately, interconnectivity could be a better measure of coating performance, but cannot be well interpreted from cross-sectional micrographs).

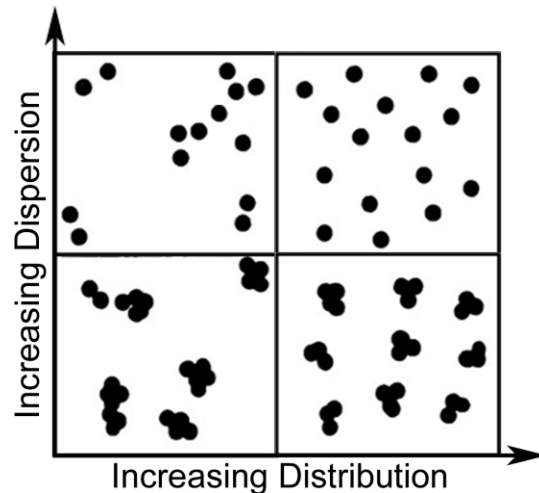


Figure 3-2. Schematic representation of the dispersion and distribution of features throughout a microstructure. After [77]

Image processing was conducted according to ASTM Standard E2109 [80] using a variety of software with automatic and manual steps. The goal of image processing was to produce porosity and glass size distributions and percentages. The first stage of image processing was conducted with the ImageJ software (National Institutes of Health, USA). First, object separation lines were drawn onto the micrograph to aid in computer differentiation of individual features. Second, the “threshold” operation was used to threshold both the pores and glass

present in the coating. The resultant image was then processed using the binary functions “close” and “open”, as necessary, to eliminate artifacts. Next, this image was edited using Adobe Photoshop (CS3, Adobe Systems Incorporated, San Jose, CA). Photoshop was used in conjunction with the BF and UV FL micrographs to identify which objects correspond to bioactive glass. These objects were then coloured to allow differentiation from pores by an automated measurement program. Additionally, any area not being considered, such as the substrate, was removed from the analysis. Finally, the micrograph was processed using an automatic measurement program in AxioVision (4.8, Zeiss, Carl Zeiss AG., Oberkochen, Germany). The output of the measurement program was used to produce bioactive glass and porosity size distributions. The control coatings were also analyzed for comparison to the blended composites. It was assumed that the area percentage generated from this analysis (See Eqn 3-1, 3-2.) was equivalent to the volumetric percentage [56,81]. The equations for both the porosity and glassy phase content were:

$$\% \text{ Porosity} = \frac{\sum \text{Pore Pixels}}{\sum \text{Pixels in micrograph} - \sum \text{Extraneous pixels}} \quad (3-1)$$

$$\% \text{ Glassy Phase} = \frac{\sum \text{Glassy Phase Pixels}}{\sum \text{Pixels in micrograph} - \sum \text{Extraneous pixels}} \quad (3-2)$$

The percent by weight of bioactive glass was calculated by assuming that the area percentage was equivalent to the volumetric percentage. A simple rule of mixtures was then employed using the densities of titanium and bioactive glass. The error in the image processing results was assessed by calculation of the two-sided 95% confidence interval according to [82]:

$$\bar{x} = \bar{x} \pm T_{97.25, n-1} \frac{s}{\sqrt{n}}. \quad (3-3)$$

The statistical significance of variables was assessed using a combination of the two-sample T -test and F -test. Statistical significance was determined with a two-tailed test in each case and significance of 0.05. First, whether the variances were equal was assessed by calculating the F statistic and comparing it to the tabulated values. The F -statistic was given by [82]:

$$F = \frac{s_1^2}{s_2^2}. \quad (3-4)$$

If the calculated value of the F -statistic was less than the critical tabulated value then the variances are equal and the T -statistic can be calculated by [82]:

$$T = \frac{\bar{X}_1 - \bar{X}_2}{\sqrt{\frac{(n_1 - 1)s_1^2 + (n_2 - 1)s_2^2}{n_1 + n_2 - 2} \left(\frac{1}{n_1} + \frac{1}{n_2} \right)}}. \quad (3-5)$$

If the calculated value of the F -statistic was greater than the critical tabulated value then the variances are unequal and the T -statistic can be calculated [82]:

$$T = \frac{\bar{X}_1 - \bar{X}_2}{\sqrt{\frac{s_1^2}{n_1} + \frac{s_2^2}{n_2}}}. \quad (3-6)$$

3.4.4. X-ray Diffraction (XRD)

The phase composition of the feedstock powders prior to thermal spray deposition as well as the coated titanium substrates were analyzed with XRD (Rigaku Ultima IV XRD System, Rigaku, ON, Canada). The patterns were solved with the Jade 7 software (Jade 7, Materials Data Inc, Livermore., CA, USA). A continuous reflective XRD mode was used in which the 2θ angle was scanned between 10

and 120° at a rate of 2 degrees per minute. The XRD machine employed a Cu anode operated at 40 kV and 44 mA. The system utilized a curved graphite monochromator. The system was configured in the focused beam geometry for the feedstock powder, while parallel beam geometry was used for the coated titanium substrates. The parallel beam mode was selected to overcome a poor signal to noise ratio due to surface roughness. An automated 10 position stage was used to streamline the analysis (ASC-10 Stage, Rigaku, ON, Canada).

3.5. In-Vitro Bioactivity Assessment

3.5.1. Simulated Body Fluid (SBF) Immersion Testing

The in-vitro bioactivity was assessed by immersion in simulated body fluid (SBF). The SBF was prepared according to the revised method and formula developed by Kokubo and Takadama [29]. The samples were rinsed with 5 mL of de-ionized ultra-filtered water (DIUF). The rinsed samples were placed in a 50 mL polymeric Petri dishes and the SBF was added. The filled Petri dishes were held at $36.5 \pm 1.5^\circ\text{C}$ in a water bath (Isotemp 210, Fisher Scientific, Ottawa, ON, Canada) for the duration of the testing. In this study, the coatings were exposed to SBF for 3, 7, and 14 days. The sample surface area to SBF volume ratio was maintained at 0.1 cm^{-1} in accordance with the procedures developed by Kokubo and Takadama [29] and the solution was also replaced every 3 days to ensure an adequate supply of ions. After testing was completed, the samples were rinsed with 5 mL DIUF and then allowed to dry in air overnight. After drying, the samples were stored in the desiccator cabinet. The treated samples were assessed for the presence of hydroxylapatite (HA) ($\text{Ca}(\text{PO}_4)_6(\text{OH})_2$) as an indicator of *in vitro* bioactivity using two techniques: scanning electron microscopy (SEM) with energy dispersive X-ray spectroscopy (EDX) and Fourier transform infrared spectroscopy (FTIR). For each technique, one sample was analyzed at each exposure time for each coating type. Further, spent samples of SBF were analyzed for the presence of metallic ions with inductively coupled plasma mass spectroscopy (ICP-MS).

Only a subset of the produced coatings was tested to investigate the effects of the type of alloy, particle size, and deposition condition (see Table 3-5). In addition to these coatings control coatings of Ti-6Al-4V alloy and Cp-Ti were tested produced using both feedstock sizes and both deposition conditions.

Table 3-5. Coatings tested for bioactivity.

Deposition Condition	Metal Powder Size Range [μm]	Bioactive Glass Size Range [μm]	Metal-based Powder
Low Flux	0-45	45 - 90	Cp-Ti Ti-6Al-4V
		90 - 180	Cp-Ti Ti-6Al-4V
	45 - 106	45 - 90	Cp-Ti Ti-6Al-4V
		90 - 180	Cp-Ti Ti-6Al-4V
High Flux	45 - 106	90 - 180	Cp-Ti Ti-6Al-4V

3.5.2. Fourier Transform Infrared (FTIR) Spectroscopy FTIR

The control coatings and the Cp-Ti-based composite coatings were analyzed with an FTIR spectrometer (Nicolet Magna-IR Spectrometer 750, Thermo Scientific, Newington, NH, USA) with a spectral range of 7000 to 50 cm^{-1} . The coated substrates were dusted with a layer of potassium bromide (KBr) powder (Xymotech Biosystems Inc, Cote Saint-Luc, QC, Canada) and the powder that did not adhere was brushed off prior to the collection of an infrared spectra. The coated substrates were run in diffuse reflectance mode with 256 scans and a resolution of 8 cm^{-1} . The spectra were collected between 400 cm^{-1} and 4000 cm^{-1} .

However, a KBr pellet method was used for the Ti-6Al-4V-based composite coatings and 45 to 106 μm Cp-Ti-based composite coatings. To facilitate the preparation of a pellet the coating was planed from the substrate using a razor blade to obtain powder. This powder was mixed with KBr powder and compressed into a spherical pellet. The pellets were run in absorbance transmittance mode with 32 scans and a resolution of 4 cm^{-1} . The spectra were collected between 400 cm^{-1} and 4000 cm^{-1} .

3.5.3. Scanning Electron Microscopy (SEM)

The treated coatings were examined using the same SEM as the feedstock powders. The SEM was used to image surface features and to identify changes in surface composition using EDX (Silicon Drift Detector, Bruker, East Milton, ON, Canada). The samples were coated with carbon using a carbon evaporator (EM SD005, Leica, Richmond Hill, ON, Canada) in preparation for examination. Imaging was conducted in both SE and backscattered electron (BSE) imaging modes at a tilt of 15° . EDX Spectra were captured over a 6.05 mm^2 area to give an average surface composition.

3.5.4. Inductively Coupled Plasma Mass Spectroscopy (ICP-MS)

An ICP-MS (Elan 6000 ICP-MS, Perkin Elmer, Waltham, MA, USA) equipped with an autosampler (AS-90/91, Perkin Elmer, Waltham, MA, USA) was used to assess whether or not the coatings released metallic ions whilst immersed in SBF. Samples of DIUF water and prepared SBF were analyzed to establish a baseline.

Samples of spent SBF taken after each 3-day interval were collected and analyzed. Analysis with the ICP-MS was conducted to measure the aqueous concentration of Ti, Al, and V. The ICP-MS was calibrated using standard stock solutions (CPI Chemicals, Vienna, Austria) at the following concentrations by mass: 0, 5, 10, and 20 ppb.

3.6. Mechanical Properties

3.6.1. ASTM C633 Adhesion Testing

The mechanical bond strength of the coatings was assessed using tensile testing according to ASTM C633 [74]. A custom set of fixtures (see Appendix 1: Drawings) was designed in accordance with ASTM C633 [74]. The custom fixtures were compatible with a uniaxial mechanical tester (3382Q1754, Instron, Norwood, MA, USA) equipped with a 100 kN load cell (47188, 2525-173, Instron, Norwood, MA, USA). These fixtures were machined from 25.4 mm diameter 1045 turned ground and polished carbon steel rod stock (Metals Supermarket, Edmonton, AB, Canada). These three fixtures (see Fig. 3-3 for an exploded isometric view of half the fixture assembly) will be referred to as a stub, a threaded cylinder, and a coupling fixture. The through hole in the coupling fixture was used to secure the assembly into the universal mechanical tester with a 12.5 mm diameter clevis pin.

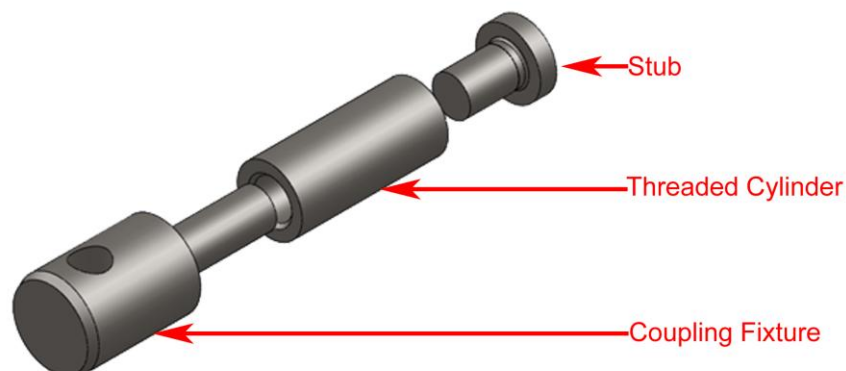


Figure 3-3. Exploded view of one set of ASTM C633 Fixtures.

The coatings tested for mechanical properties were identical to the subset used in the bioactivity study (see Table 3-4). The bonding surfaces of the fixtures and the uncoated reverse side of the substrate were grit blasted and cleaned with 5 mL of acetone and 5 mL of isopropyl alcohol. For each sample condition, a total of five assemblies corresponding to five coated circular substrates and ten stubs were grit-blasted. The diameter of each coated substrate was measured using a caliper. This diameter was used to calculate the cross-sectional area of the coating. The cleaned stubs and substrates were then bonded using the two-component cold mount metallurgical epoxy with fluorescent dye (see Fig. 3-4 for a schematic representation of the bonded assembly). To ensure consistent epoxy thickness a 7.7 mL transfer pipette (Fisher Scientific, Ottawa, ON, Canada) was used to place a single drop (~0.2 mL) of epoxy on each surface. The surfaces were then placed together and any excess epoxy that was squeezed from the interface was wiped off. The alignment was checked by hand. The assemblies were allowed to cure overnight (approximately 15 h). In addition to the coated circular substrates, one set of stubs were bonded together with epoxy alone to calibrate for the bond strength of that batch of epoxy.

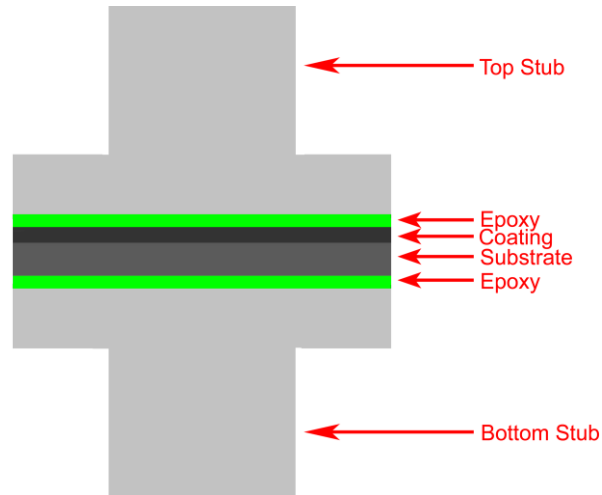


Figure 3-4. Schematic representation of the bonded ASTM C633 fixture-substrate assembly.

The bonded assemblies were then threaded into the fixtures and top-loaded into the universal mechanical tester. Top-loading was selected to ensure that the fixtures would align in the z -direction under their own weight. The coatings were subsequently tested until failure occurs. The maximum load was recorded and used for calculation of the breaking stress, depicted by

$$\sigma_f = \frac{F_f}{\pi D_{\text{substrate}}^2} . \quad (3-3)$$

The average breaking stress was computed through a simple arithmetic average and the standard deviation was computed as a sample standard deviation. It was assumed that the area used in the calculation was the projected surface area of the circular substrate. The data was collected using the Series IX software (Instron, Norwood, MA, USA). The uniaxial tensile tester operated with a constant cross-head speed of 0.84 mm/min and data was captured at a rate of 10 Hz.

The thickness of the control coatings was measured through image analysis of micrographs with the imageJ software package. Two micrographs corresponding to a total of 6 mm of coating length were taken and analyzed. A total of 20 thickness measurements were taken per coating and each measurement was spaced 300 μm apart (for a total of 6 mm of coating length). The thickness measurements were utilized to assess the effect, if any, of thickness on the mechanical adhesion strength.

3.6.2. Fractography

Analysis of the fracture surfaces was conducted by macro photography of the failed sample. A digital single lens reflex camera (D300s, Nikon Corp., Tokyo, Japan) equipped with a 60 mm lens (AF-Micro Nikkor f2.8D, Nikon Corp., Tokyo, Japan) was mounted on a camera stand (MP4 Land Camera, Polaroid Corp., Waltham, MA, USA). The subject to lens distance was fixed at 241 mm to ensure consistent magnification. Failed coatings were placed on an adjustable lab stand (Fisher Scientific, Ottawa, ON, Canada) and the height was adjusted until the fracture surface was in focus. The aperture was set to f8 and the exposure was set to 1/3 of a second. The failed samples were imaged using both oblique lighting and a UV lamp (B-100 Spectroline, Spectronics Corp., Westbury, NY, USA). The resultant images were examined to assess the fracture mode of the specimen. The fracture mechanism, origin of crack initiation, and the path of fracture propagation were not studied.

Chapter 4 – Mathematical Model of Flame Spraying⁴

4.1. Heat Transfer Estimation of Particle Temperatures during Deposition

The in-flight temperature (T_p) of the particles was of particular importance for predicting their behaviour on impact as well as the degree of reaction that occurs. The model developed here, modified from the supersonic compressible flow model derived by Dewar *et al.* [76], was intended to predict T_p for subsonic compressible flow. Here, the additional heat generated by chemical reactions, such as the oxidization of metallic particles, was neglected and the heating occurring due to forced convection during flight was focused upon. However, the purpose of this analysis was to provide insight into the final coating structure, morphology and composition by comparing the relative temperatures attained by the Cp-Ti, Ti-6Al-4V alloy, and bioactive glass powders under the two deposition conditions. For the purposes of this analysis it was assumed that the particles are spherical.

A lumped capacitance model was developed for use in this study assuming the Biot number (Bi) was < 0.1 , so that no temperature gradient existed within each particle. The Biot number being less than 0.1 is a requirement for the validity of

⁴ A version of this chapter has been submitted for publication in the Journal of Materials Science and Engineering – Part C

this model as a Biot number in excess of 0.1 would indicate that the particle possessed an internal temperature gradient. This assumption was likely reasonable, but was validated, as the particle diameters are on the order of 10^{-5} to 10^{-4} m, with thermal conductivities of approximately 22 [83], 7 [83], and 0.9 W $m^{-1} K^{-1}$ [84] for Cp-Ti, Ti-6Al-4V alloy, and bioactive glass, respectively. Therefore, it was likely that the Biot number will be less than 0.1 for all particles in this study and thus there was no temperature gradient within each particle. The Biot number is defined as

$$Bi = \frac{hd_p}{6k_p}. \quad (4-1)$$

The particle temperature in this model varied only with the time the particle traveled within the flame jet (t_x) and the particle temperature was governed by the conservation of energy. The equation used in this study includes the adiabatic wall temperature (T_{aw}) and the ambient temperature (T_0). The ambient temperature was the temperature at which the powder entered the carrier gas stream and was assumed to be 20°C. The transient temperature of the particle was given [76] by:

$$T(t) = T_{aw} - (T_{aw} - T_0) \exp \left[- \frac{hA_s}{c_p \rho_p d_p \Omega} t_x \right]. \quad (4-2)$$

The time of flight for the particles, $t_x = \frac{L_s}{v_p}$ was used to estimate the transient temperature of the particle. If it was assumed that the particles are spherical and the stand-off distance equates to the total distance traveled in the jet by each particle then the temperature attained by the particle in flight was defined [76] by:

$$T_p = T_{aw} - (T_{aw} - T_0) \exp \left[-6 \frac{h}{c_p \rho_p d_p} \frac{L_s}{v_p} \right]. \quad (4-3)$$

During the flight of a particle through the flame jet heat was added to the particles through forced convective flow and viscous shear work by the fluid. A portion of this heat was conducted away from the particle surface and into the bulk reducing the amount of energy available to raise the surface temperature of the particle. Therefore, the equilibrium particle temperature was typically less but no more than the adiabatic wall temperature (T_{aw}). However, a recovery factor, r , was used to calculate the adiabatic wall temperature from the flame temperature. Shapiro [85] defined the adiabatic wall temperature as a function of the free stream temperature of the fluid (T_{flame}) and the Mach number

$$T_{aw} = \left[1 + r \frac{\gamma - 1}{2} \text{Ma}^2 \right] T_{flame}. \quad (4-4)$$

The recovery factor has been established for subsonic flow over a number of different geometries by theoretical analysis and experimentation as a simple relationship [86]. The recovery factor was defined by:

$$r \cong \sqrt{\text{Pr}}. \quad (4-5)$$

The Mach number was calculated as a function of the velocity of the gases creating jet and the mathematical definition of the speed of sound in an ideal gas.

The Mach number was defined as

$$\text{Ma} = \frac{v_g}{\sqrt{\gamma R T_{flame}}}. \quad (4-6)$$

The velocity of the flame gases were needed to estimate the Mach number and Reynolds numbers. The velocity of the argon and fuel gases was estimated using

the correlations between volumetric flow rate and linear velocity developed for an identical torch by Bandyopadhyay and Nylén [68]. The velocity of the argon flow was 20 m/s for both sets of parameters; while, velocities of 122 and 86 m/s were found for the oxy-acetylene flow for the high and low flux deposition condition, respectively. For the purposes of this model, the oxy-acetylene flow velocity was assumed to be the overall velocity of the flame jet because it was much larger than that of the argon.

The Reynolds number of the flow over all particles in this study was $\ll 5 \times 10^6$; therefore, it was assumed that the particle-fluid boundary is laminar in nature. The Reynolds number for a spherical particle traveling in a moving fluid flow was given by:

$$\text{Re}_{d_p} = \frac{d_p (v_g - v_p) \rho_g}{\mu_g} . \quad (4-7)$$

The forced convective heat transfer coefficient, h , was determined from the theory of cones for subsonic flow over a body of revolution. An expression for the coefficient was derived using the equations outlined by Shapiro [86] and was given by:

$$h \cong \frac{k_g}{d_p} (0.575 - 0.0094 \text{Ma}^{3/2}) \sqrt{\text{Re}_{d_p}} \times \text{Pr} . \quad (4-8)$$

The final variable not yet discussed in Eqn. 4-3 is the velocity of the particles (v_p). The particle velocities were not measured in this study; rather, an iterative approach where an expected range of particle velocities was used on the basis of literature. Other work indicates that metallic particles, such as nickel alloys,

should travel between 15 to 30 m/s [68]. It is conceivable that if bioactive glass particles are imparted the same momentum as metallic particles of the same diameter then ceramic particles should reach higher velocities due to their substantially lower densities (approximately 50% the density of titanium). As such, a range of particle velocities from 10 to 40 m/s was used for this analysis and the predicted temperatures were compared to the manufactured coatings to determine trends between deposition conditions, powder composition, and powder size distribution. It should be noted that this simplified model provides conservative estimates of the particulate temperature due to the exclusion of the additional heat generated by the presence of metallic particles within the oxygen containing flame.

Chapter 5 – Results and Discussion⁵

5.1. Thermodynamic Estimation of Flame Temperature During Flame Spray Deposition

The temperature of the flame as well as the chemical environment produced by the combustion of the fuel gas is heavily dependent on the spray parameters. Of particular importance are the relative proportions of C₂H₂, O₂, and Ar present within the flame; while, the flow rates of each gas affect the velocity of the flame as well as particle velocity on impact with the substrate. The flame temperature and chemical environment will play a role on the degree of melting of the particles injected into the flame as well as the final microstructure and phase composition of the coating. It is difficult to measure the true combustion temperature due to the multitude of reactions which occur in the jet and due to entrainment of air and loss of heat to the environment. Here, an adiabatic flame temperature – assuming no heat is lost to the environment – is used to compare the low and high flux conditions to gain insight into the effects the spray parameters have on the final coating.

The combustion was modeled as an isobaric and adiabatic reaction of C₂H₂ and O₂ mixed with inert Ar. It was assumed that the total pressure is 1 atm and that the

⁵A version of this chapter has been published in Nelson *et al.* [78], “Flame Spray Deposition of Titanium Alloy-Bioactive Glass Composite Coatings”, *Journal of Thermal Spray Technology*, volume 20, issue 6, Dec 2011, pg 1339-1351.

A version of this chapter has been accepted for publication. Nelson 2013. *Surface Innovations*.

A version of this chapter has been submitted for publication in the *Journal of Materials Science and Engineering – Part C*

initial temperature of the gaseous phases was 293 K. The thermodynamic calculations, including calculation of the composition and density of the flame, were performed using the FactSageTM thermodynamic software package (6.1, CRTC, Montreal, QC, CA) with the molar flow rates of C₂H₂, O₂, and Ar as inputs. The resultant adiabatic temperature was found to be 3381 K and 3358 K for the high and low flux deposition condition respectively. The flame temperatures calculated are in agreement with the range of flame temperatures found for oxy-acetylene flame spraying by other investigators (3000 to 3400 K) [13,68]. However, the actual flame temperature was likely lower due to radiative and convective cooling of the flame as well as the formation of other products such as NO_x from the entrainment of air. Additionally, once particles are introduced into the torch plume exothermic reactions such as oxidization of metallic particles would serve to increase the flame temperature.

To estimate the fluid and thermal properties of the resultant gas mixture, it was assumed that the dissociation products, such as O²⁻, H⁺, and OH⁻, could be neglected from the flame composition. Therefore, the flame was modeled as an ideal mixture of Ar, O₂, CO, CO₂, H₂O, H₂, as shown in Table 5-1, since these gases represent the non-dissociated products, corresponding to approximately 90 wt. % of the total composition. The flame properties were estimated using a sum of partial molar properties, that is, the property of each individual component was multiplied by its corresponding molar fraction. This approach has been used by other investigators to estimate the viscosity of gaseous mixtures [87]. The partial

molar property sums method was also used to estimate the thermal conductivity and to calculate the specific heat capacity of the gaseous mixture of the flame. While there are more complicated and accurate methods to estimate the viscosity and thermal conductivity of a gaseous blend [87-90], this approximation is reasonable as this analysis was intended to compare high flux to low flux deposition conditions as well as the various powder blends utilized in this study. The specific heat capacities were evaluated at the adiabatic flame temperature [91,92] and both the viscosity and thermal conductivity were evaluated at 2000°C [93] (limit of reference data). The resultant calculated properties (see Table 5-2) were used for all further calculations.

Table 5-1. Gaseous composition used for modeling the fluid properties.

Deposition Condition	Molar Fraction					
	Ar	O ₂	CO	CO ₂	H ₂ O	H ₂
Low Flux	0.19	0.03	0.51	0.08	0.10	0.09
High Flux	0.13	0.03	0.56	0.07	0.10	0.10

Table 5-2. Summary of gaseous properties used for heat transfer modeling.

Deposition Condition	T_{flame} [K]	v_g [m s ⁻¹]	ρ_g [g m ⁻³]	c_p [J kg ⁻¹ K ⁻¹]	k_g [10 ⁻³ W m ⁻¹ K ⁻¹]	μ_g [10 ⁻⁶ Pa s]	γ
Low Flux	3358	85	82.7	1956	187	87.1	1.21
High Flux	3381	122	87.4	1966	196	86.6	1.23

5.2. Characterization of Powder Feedstock Prior to Thermal Spraying

The feedstock powder was characterized prior to thermal spraying. The particle size distribution, the phase composition, and the particle morphology were characterized. The particle size distribution was assessed by a sieve analysis of the as-received powder. The phase composition of the powders was assessed with XRD of the as-received powder and the particle morphology was assessed with SEM imaging of the as-received powder and the bioactive glass after milling.

5.2.1. Particle Size Distribution (PSD)

The particle size distributions of the feedstock powders prior to flame spray deposition were assessed by sieve analysis. The masses in each range were recorded and normalized by the total powder mass. This analysis was conducted on the as-received powders. The metallic powder size distributions are plotted in Figure 5-1 while the bioactive glass powder size distribution is included in Figure 5-2. There was no significant difference between the Ti-6Al-4V alloy and Cp-Ti powder distributions. The < 45 μm powder had a mean size between 38 and 45 μm while the 45 to 106 μm powder had a mean size between 63 and 90 μm . The bulk of the bioactive glass powder was between 354 and 500 μm .

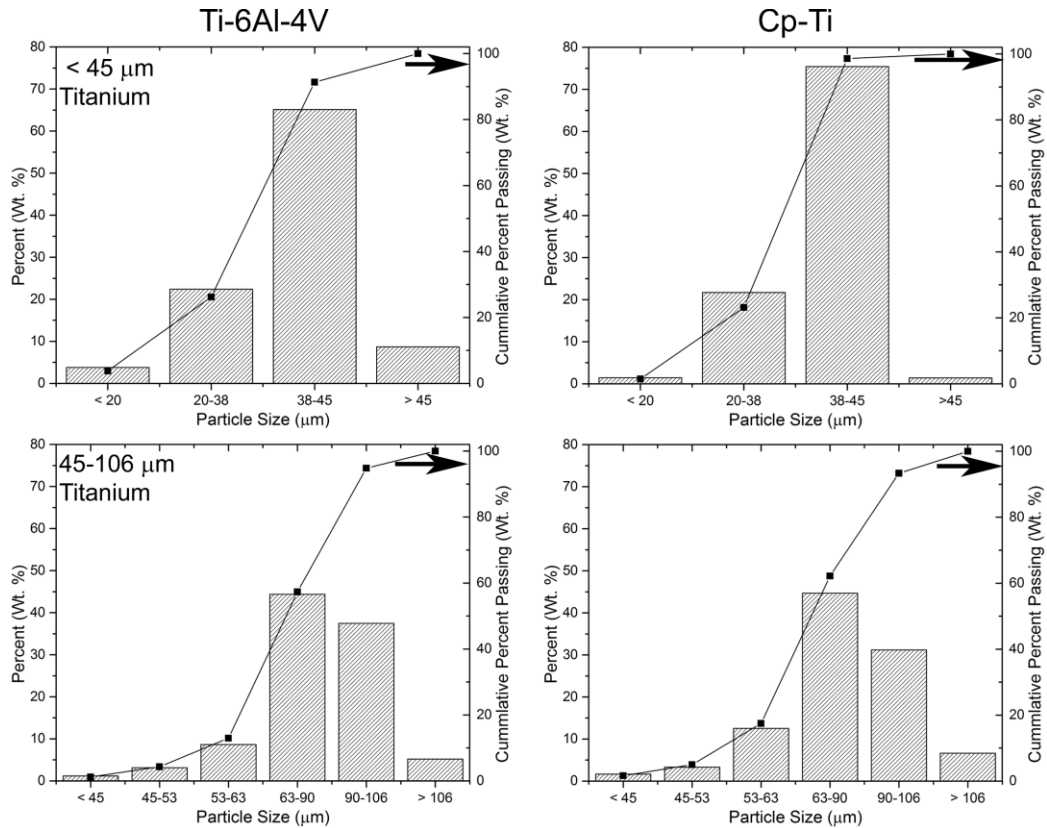


Figure 5-1. Powder size distributions of the as-received metallic powders measured by sieve analysis.

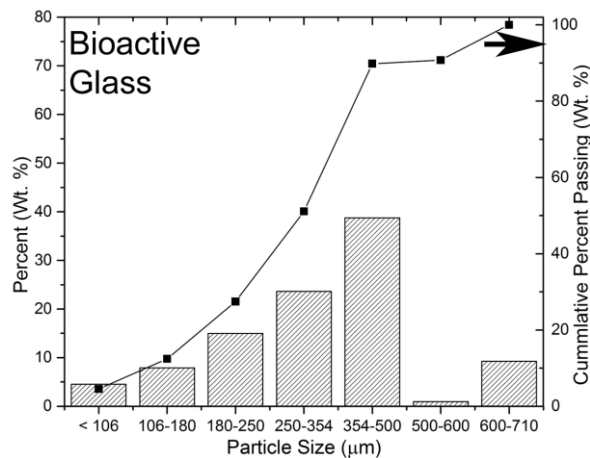


Figure 5-2. Powder size distribution of the as-received bioactive glass powder measured by sieve analysis.

5.2.2. X-ray Diffraction (XRD)

The phase composition of the feedstock powders prior to flame spay deposition were assessed by XRD analysis. Figure 5-3 shows XRD patterns of the powder

particles. The 45 to 106 μm Ti-6Al-4V alloy powder provided by Raymor and Carpenter had identical pattern (see Fig. 5-3). The peaks that were characteristic of all Ti-6Al-4V alloy powders corresponded to a titanium-aluminum phase Ti_xAl_y . The characteristic peaks for both Cp-Ti powders corresponded to metallic titanium, and the bioactive glass powder was amorphous as evidenced by the large, broad band located at $2\theta = 30^\circ$ to 40° .

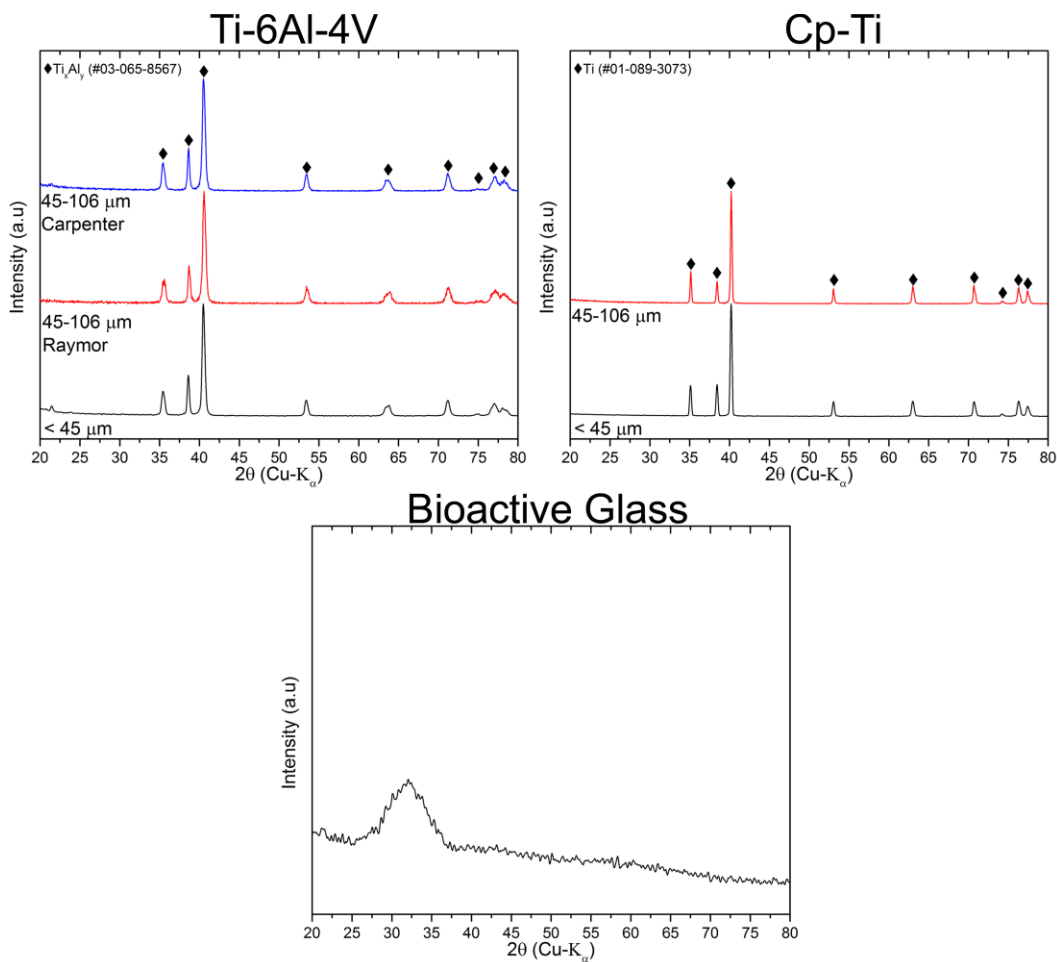


Figure 5-3. X-ray diffraction patterns of the as-received feedstock powder.

5.2.3. Powder Morphology

The morphology of the feedstock powders prior to flame spray deposition were assessed by using SEM imaging in the SE imaging mode (see Fig. 5-4). The

bioactive glass powder was assessed both as-received and after milling. While, only as-received metallic powders were imaged. A sample from both the Carpenter and Raymor 45 - 106 μm Ti-6Al-4V alloy powder was imaged and had identical morphology (see Fig. 5-4a). The metallic powders were spherical in morphology, regardless of the size range or composition. The bioactive glass powders both before and after milling had an angular, irregular and crushed morphology. Additionally, as several batches of powder were used in this study a representative comparison of the final coating microstructure between two different batches is included in (Fig. 5-4b). The morphology of the coating is deemed equivalent due to the similarities in the coating thickness, coating porosity, and the bioactive glass and porosity is both well dispersed and well distributed throughout the structure in each case.

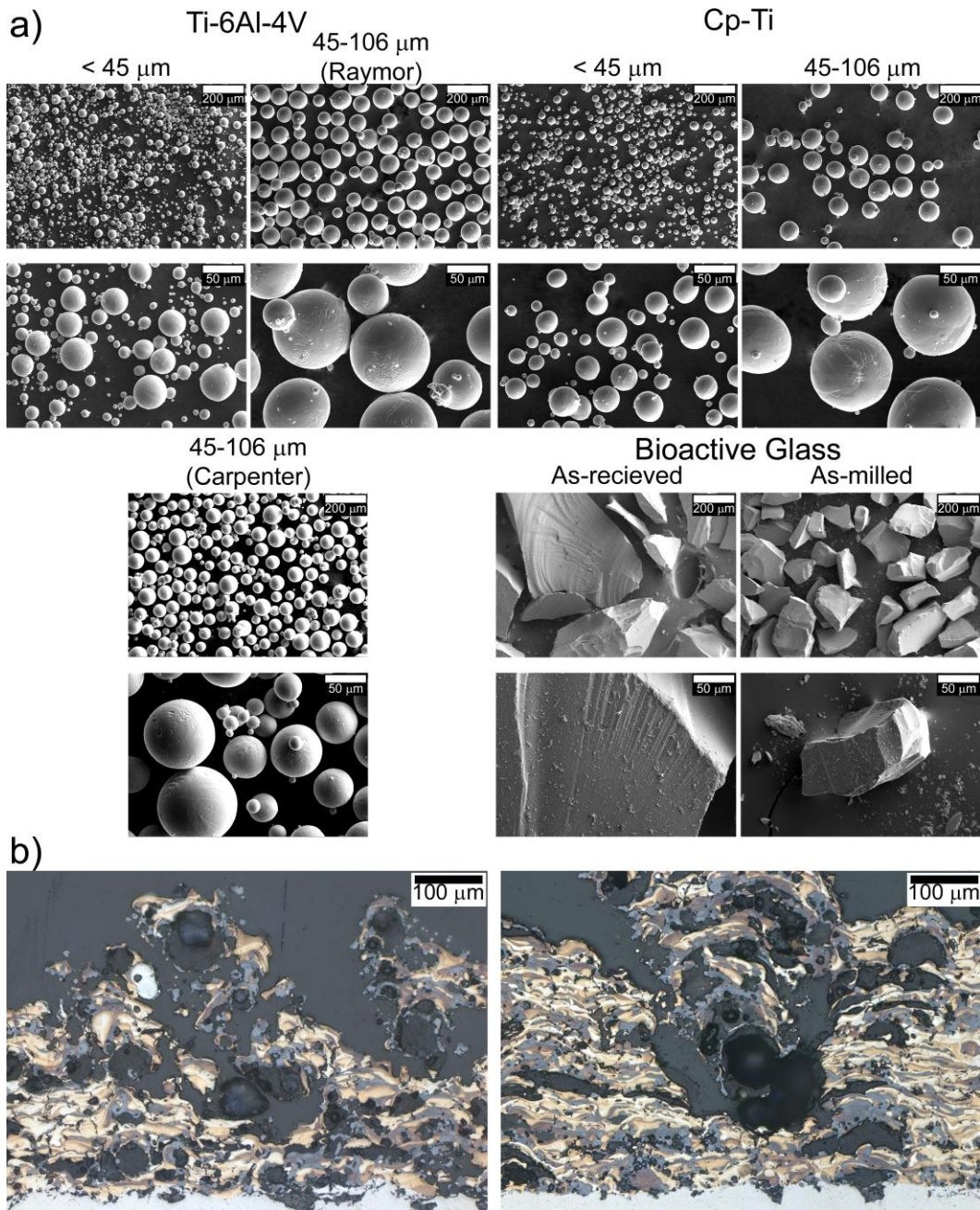


Figure 5-4. a. SEM micrographs of the feedstock powder prior to thermal spray deposition. Images were taken in SE imaging mode; b. OM micrographs of coatings demonstrating reproducibility of coating morphology fabricated from <math>< 45 \mu\text{m}</math> Ti-6Al-4V alloy powder and 45 - 90 μm bioactive glass under the low flux condition from two different batches of Ti-6Al-4V powder; (left) lot 5573-S and (right) lot 236-L3.

5.4. Characterization of Preliminary Coatings

The preliminary coatings characterized herein refer to those deposited with the powder blends in Table 3-3. Characterization of the preliminary coatings was conducted by qualitative comparison of cross-sectional optical micrographs and by comparison of the XRD patterns collected on each sample. The homogeneity of the coating was assessed by a qualitative binary assessment of whether the porosity and glassy phase was well dispersed and well distributed throughout the microstructure (see Fig. 3-2). After characterization was performed a single blending ratio was selected for further study on the basis of homogeneity of the spatial bioactive glass distribution, apparent porosity, and phase composition.

5.4.1. Cross-sectional Optical Microscopy (CS-OM)

Coatings prepared from 106 - 212 μm bioactive glass powder blended with < 45 μm Ti-6Al-4V alloy powder as well as control coatings (pure bioactive glass and pure Ti-6Al-4V alloy) were deposited by flame spraying onto titanium substrates. Both the high flux and low flux deposition conditions were used. The coatings were examined with optical microscopy, and representative images ($n = 5$) are presented in Fig. 5-5. The pure bioactive glass did not adhere well to the substrate for either set of deposition conditions, leaving only a scattering of glass particles on an otherwise bare substrate. When 38 wt. % bioactive glass was mixed with Ti-6Al-4V alloy, the composite coating exhibited a rough and porous microstructure for both deposition conditions. The coating was continuous; however, the distribution of bioactive glass through the coating was not

homogenous. In the composite coatings containing 15 wt. % bioactive glass, the glass distribution throughout the sample was more homogenous than that of the composite coatings with 38 wt. % bioactive glass. However, in the high flux deposition condition; there was no visual evidence of pore connectivity within the cross section. The pure Ti-6Al-4V alloy coating deposited under the high flux deposition condition exhibited a more compact and less porous coating than that deposited under the low flux deposition condition. The cross sectional micrographs (see Fig. 5-5) indicate that the bioactive glass is circular in shape for the coatings deposited from the composite blends (see Table 3-3). The circular shape differs from the usual angular and jagged shapes of the initial glass powder (see Fig. 5-4). This rounding of the bioactive glass powder suggests that the softening temperature (550°C) was reached or exceeded during deposition [94]. The heated bioactive glass changed from a jagged shape to a spherical shape to minimize surface free energy.

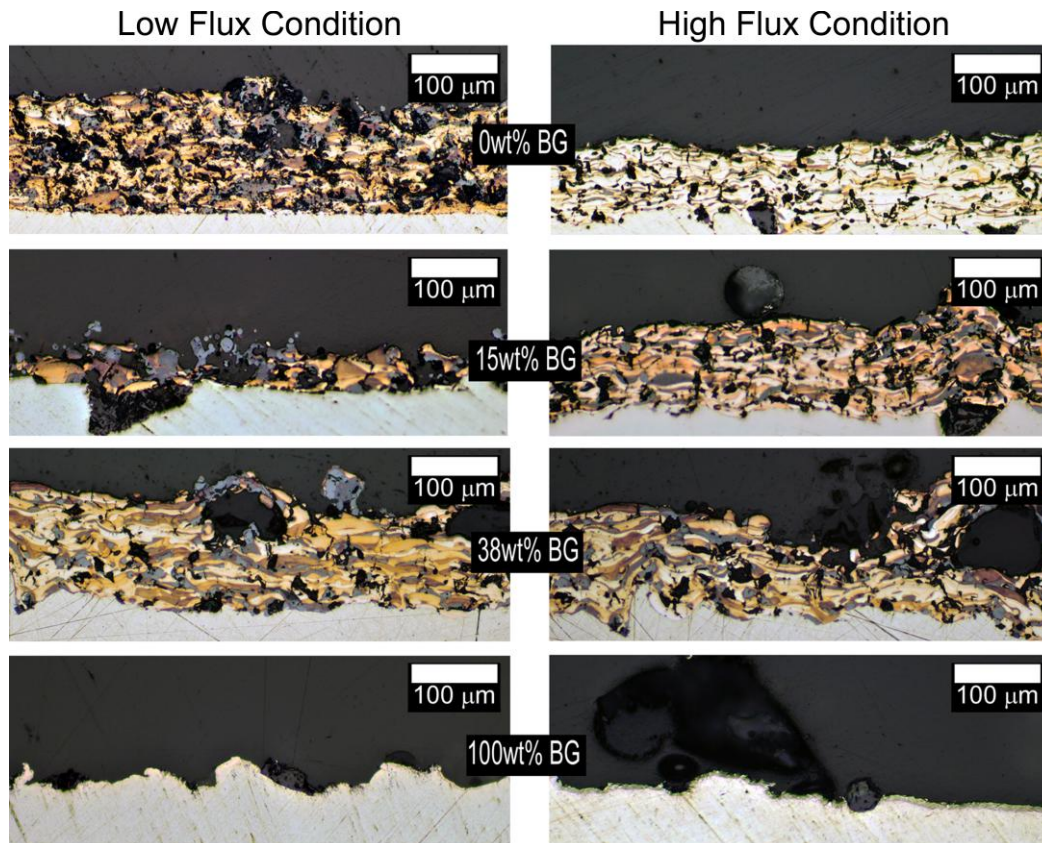


Figure 5-5. Optical cross-sectional micrographs of the coatings produced with the preliminary powder blends.

5.4.2. X-ray Diffraction (XRD)

The preliminary coatings were also analyzed with XRD and the profiles are presented in Fig. 5-6. The background on each profile has been stripped and the residual noise was reduced by a smoothing operation with the Jade 7 XRD software. Peak assignments were determined according to the guidelines provided in the Jade 7 XRD database. The pure bioactive glass coatings exhibited peaks for combeite ($\text{Na}_2\text{Ca}_2\text{Si}_3\text{O}_3$), titanium sub-oxide ($\text{TiO}_{0.89}$), titanium, and anatase phase of titanium dioxide (TiO_2). Titanium dioxide and titanium sub-oxide were present due to oxidation of the titanium substrate. The pure Ti-6Al-4V alloy control coating and composite coatings exhibited several phases: TiO_x , the anatase phase

of TiO_2 , the rutile phase of TiO_2 , metallic Ti, and a vanadium substituted titanium (III) oxide $(\text{Ti,V})_2\text{O}_3$

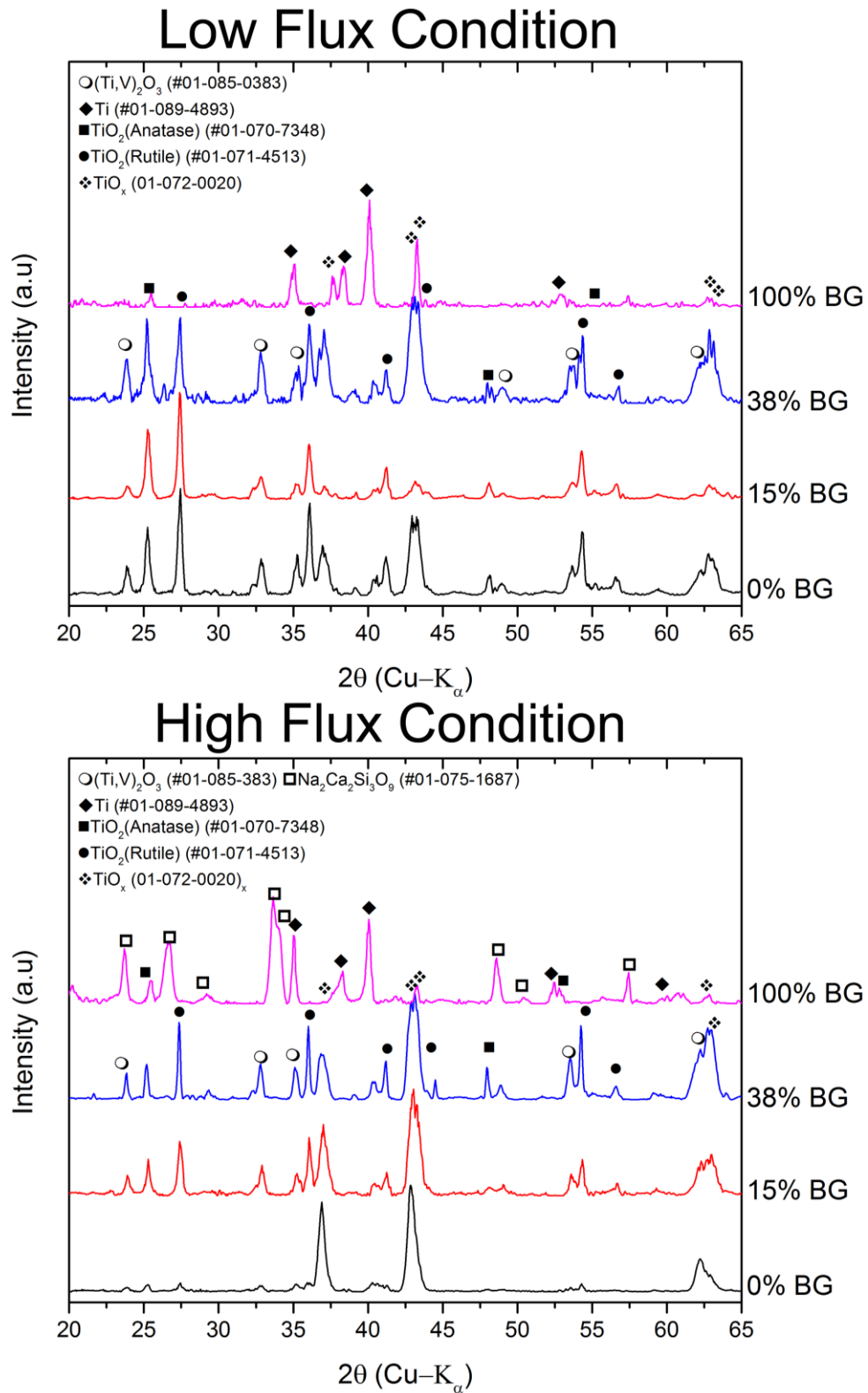


Figure 5-6. X-ray diffraction patterns collected from the coatings fabricated from the preliminary powder blends. The weight percentage of bioactive glass is indicated to the right of the plot.

The presence of a vanadium substituted oxide is supported by oxidation studies performed on Ti-6Al-4V alloy in an environment containing water vapour; however, there should also be alumina (Al_2O_3) within the scale [95]. But, Al_2O_3 is not observed in any of the patterns that were examined. The presence of combeite indicates that the bioactive glass powder was heated above its crystallization point (650 – 700 °C) during thermal spray deposition for high flux coatings and Cp-Ti-based composite coating [96,97]. However, it is also possible that the combeite peaks correspond to the iso-structural compound, $\text{Na}_2\text{CaSi}_2\text{O}_6$, which was found to be the main crystalline phase of 45S5 bioactive glass, formed between 610°C and 800°C by Lefebvre *et al.*[94] and Lin *et al.*[98]. Regardless, the presence of these peaks indicates crystallization of the previously amorphous (see Fig. 5-3) bioactive glass in the case of coatings deposited under the high flux condition. A previous study by Nychka *et al.* [46] indicated that the dissolution rate of bioactive glass in a crystalline form is modified from its amorphous form in a complex manner that lead to a distribution of dissolution rates that may be dependent on crystallographic direction. Additionally, the less stable bonds present within an amorphous glass should aid dissolution [46]. However, the crystallization of bioactive glass may retard the bioactive glasses ability to promote the differentiation of osteoblasts. As such, the crystallization of the bioactive glass when depositing under the high flux deposition condition could compromise the osteopductive response of the bioactive glass.

The adiabatic flame temperatures were much greater than the recrystallization point of the bioactive glass for both deposition conditions. The absence of crystalline combeite peaks under the low flux deposition condition, and the recrystallization of the bioactive glass under the high flux deposition condition can be explained by two possible mechanisms. The first mechanism is due to possible in-flight cooling of the particles between the torch and the substrate during deposition under the low flux deposition condition. During deposition with the low flux deposition condition, the torch was farther from the sample and the velocity of the gaseous stream was lower, compared to the high flux deposition condition. The increased distance and reduced velocity allowed additional convective cooling of the flame jet and the particles within the jet. The increased distance also allowed entrainment of cold air into the flame jet. The larger temperature difference between the hot particles and cold air entrained into the flame resulted in higher cooling rates. This is supported by the presence of amorphous bioactive glass in the coating samples produced under the low flux deposition condition, since higher cooling rates are necessary to prevent recrystallization and produce an amorphous structure. The second mechanism may be due to heating of the substrate due to impingement of the flame jet. During deposition under the high flux deposition condition, the torch was closer to the substrate, compared to the low flux deposition condition. The decreased stand-off distance resulted in additional heating of the substrate, which was covered by the initial layers of the coating, due to impingement of the flame. The higher temperature of the heated substrate produced smaller temperature gradients

between the heated substrate and the hot deposited particles. These smaller temperature gradients led to lower cooling rates, which produced the crystalline Combeite phase in the final coating. Alternatively, the heating due to the impingement of the torch for the high flux deposition condition heated the substrate above the recrystallization temperature of the bioactive glass. In any case, identification of which mechanism that played a dominant role requires further analysis and will be further addressed during the discussion of the theoretical models; but it is indisputable that the cooling rate of the bioactive glass particles was higher in the low flux deposition condition and/or that the lower stand-off distance allowed for heating of the substrate, including previously deposited layers of the coating, that resulted in crystallization under the high flux deposition condition

5.4.3. Selection of a Powder Blending Ratio

The selection of a powder blending ratio for further analysis was made on the basis of apparent homogeneity of the spatial bioactive glass distribution, apparent porosity, and phase composition. The 15 wt. % bioactive glass with 85 wt. % metallic titanium blend was selected due to apparent pore interconnectivity and the homogenous distribution of bioactive glass (see Fig. 5-5). The phase composition, as observed by XRD (see Fig 5-6), was equivalent to the coating sprayed from the pure Ti-6Al-4V alloy powder or the 38 wt. % bioactive glass powder blend and showed no evidence of bioactive glass crystallization (see Fig. 5-6).

5.5. Coating Characterization

After selection of the powder blend that contained 15 wt. % bioactive glass powder and 85 wt. % Ti-6Al-4V alloy powder, the focus of the work shifted to assessing the effects of deposition conditions, feedstock composition, and feedstock particle size distribution. The microstructure, morphology, and the phase composition of the coated titanium substrates were assessed with optical microscopy, quantitative image analysis, and x-ray diffraction. The repeatability of the microstructure and the phase composition was assessed by examining cross-sections of coatings and by collecting x-ray diffraction patterns on coatings deposited in separate flame spray deposition runs; additionally, the repeatability was assessed in a qualitative manner and is in agreement with the results presented by Nelson *et al.* [78]. The results presented herein led to the selection of a representative subset of coatings (as shown in Table 3-5) for further analysis. For each analysis a summary visual schematic was prepared to demonstrate the trends observed

5.5.1. Cross-sectional Optical Microscopy (CS-OM)

Cross-sectional optical microscopy (CS-OM) was performed to study the microstructure and morphology of the deposited coatings as well as to facilitate the quantitative image analysis that established the porosity and glassy phase distributions. Representative optical micrographs are included in Fig. 5-7 to Fig. 5-10. A summary visual schematic was prepared that summarizes the important trends that are discussed herein regarding the observed morphology of the coating

(see Fig. 5-11). The micrographs were grouped by deposition condition and metallic powder composition. The control coatings (see top images in Fig. 5-7 to Fig. 5-10) exhibit a porous but uniform laminar structure. The boundaries between splats are visible as variations in contrast between different lamellae. Additionally, it is evident from a qualitative comparison that the porosity of the Ti-6Al-4V alloy control coatings is higher than that of the Cp-Ti control coatings. However, a quantitative assessment of the porosity will be discussed in section 5.5.2. Similar trends were noted for the all Ti-6Al-4V alloy control coatings when compared to their Cp-Ti counterparts. The control coatings deposited under the high flux deposition condition do not exhibit a significantly different morphology from their low flux control counterparts. Further, it is additionally noted that the 45 - 106 μm Ti-6Al-4V alloy coating deposited under the high flux condition was significantly thinner as compared to its counterpart. The thinner coating could be due to a poor degree of sticking of the impacting particles during deposition or to erosion of the coating from the impingement of the flame during deposition under the high flux deposition condition.

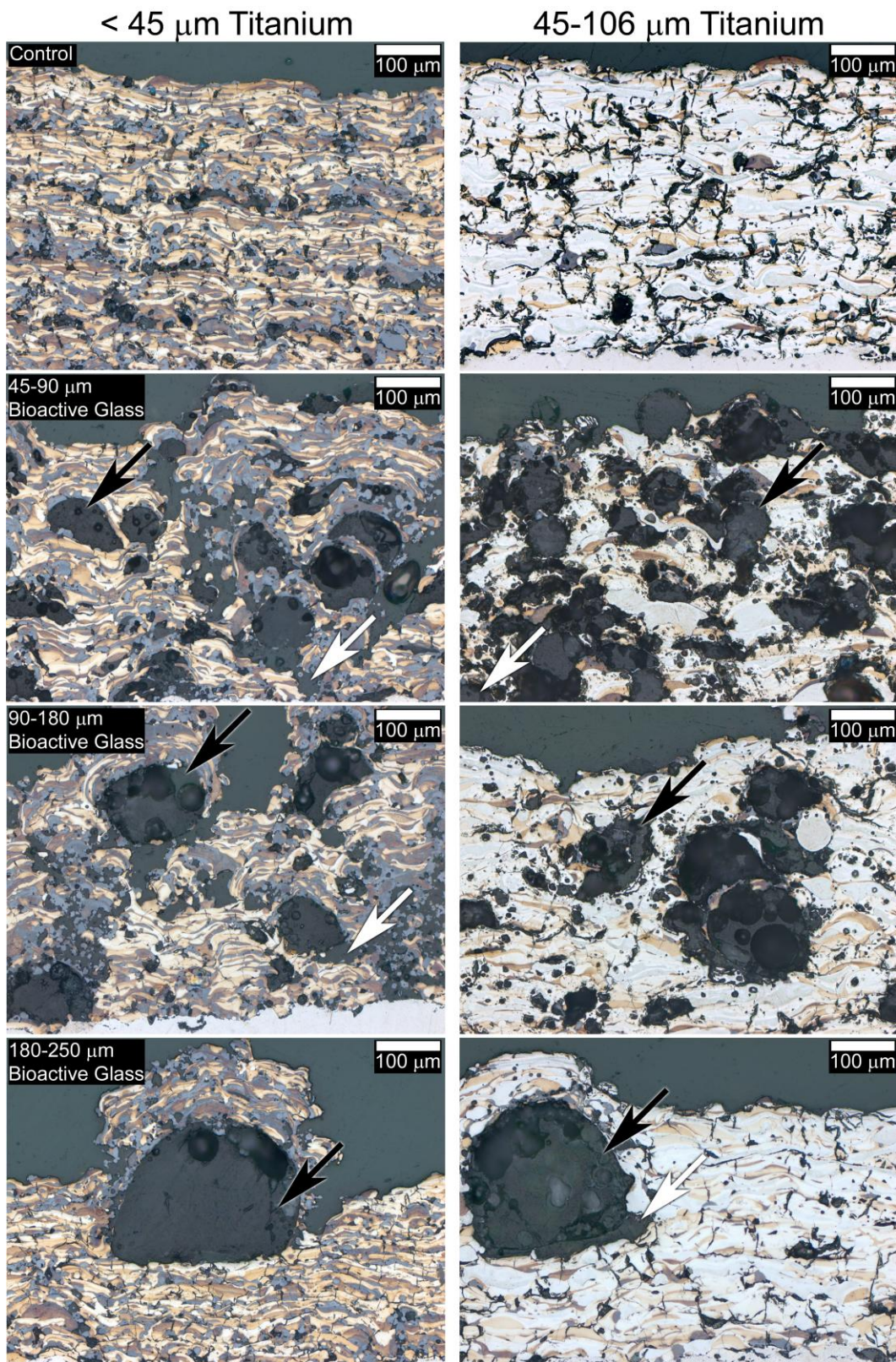


Figure 5-7. Representative optical cross-sectional micrographs of Ti-6Al-4V-based coatings sprayed under the low flux deposition condition. Arrow legend: Black – Bioactive glass; White – Epoxy-filled pore.

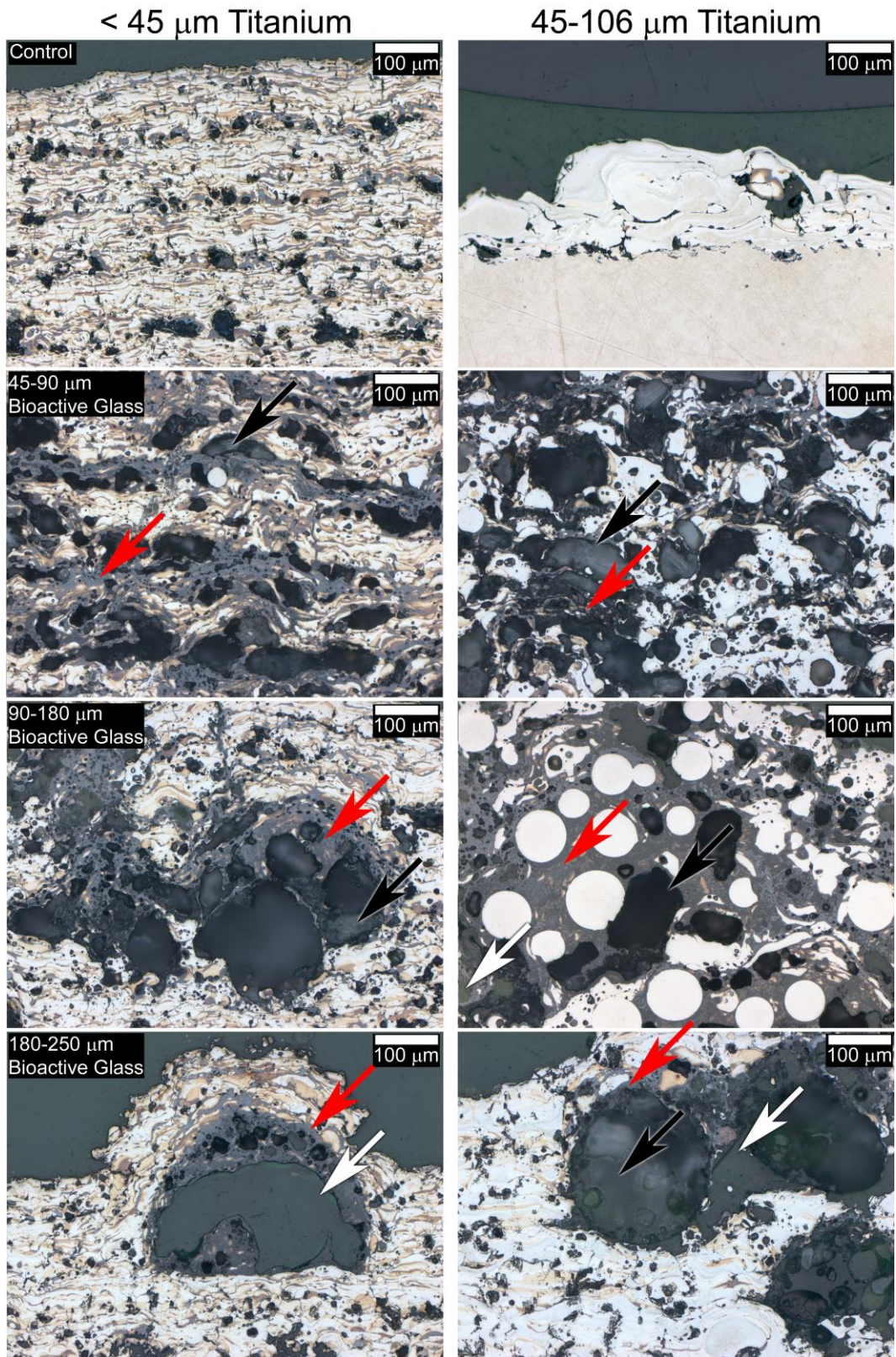


Figure 5-8. Representative cross-sectional optical micrographs of Ti-6Al-4V-based coatings sprayed under the high flux deposition condition. Arrow legend: Black – Bioactive glass; Red – Reaction phase; White – Epoxy-filled pore.

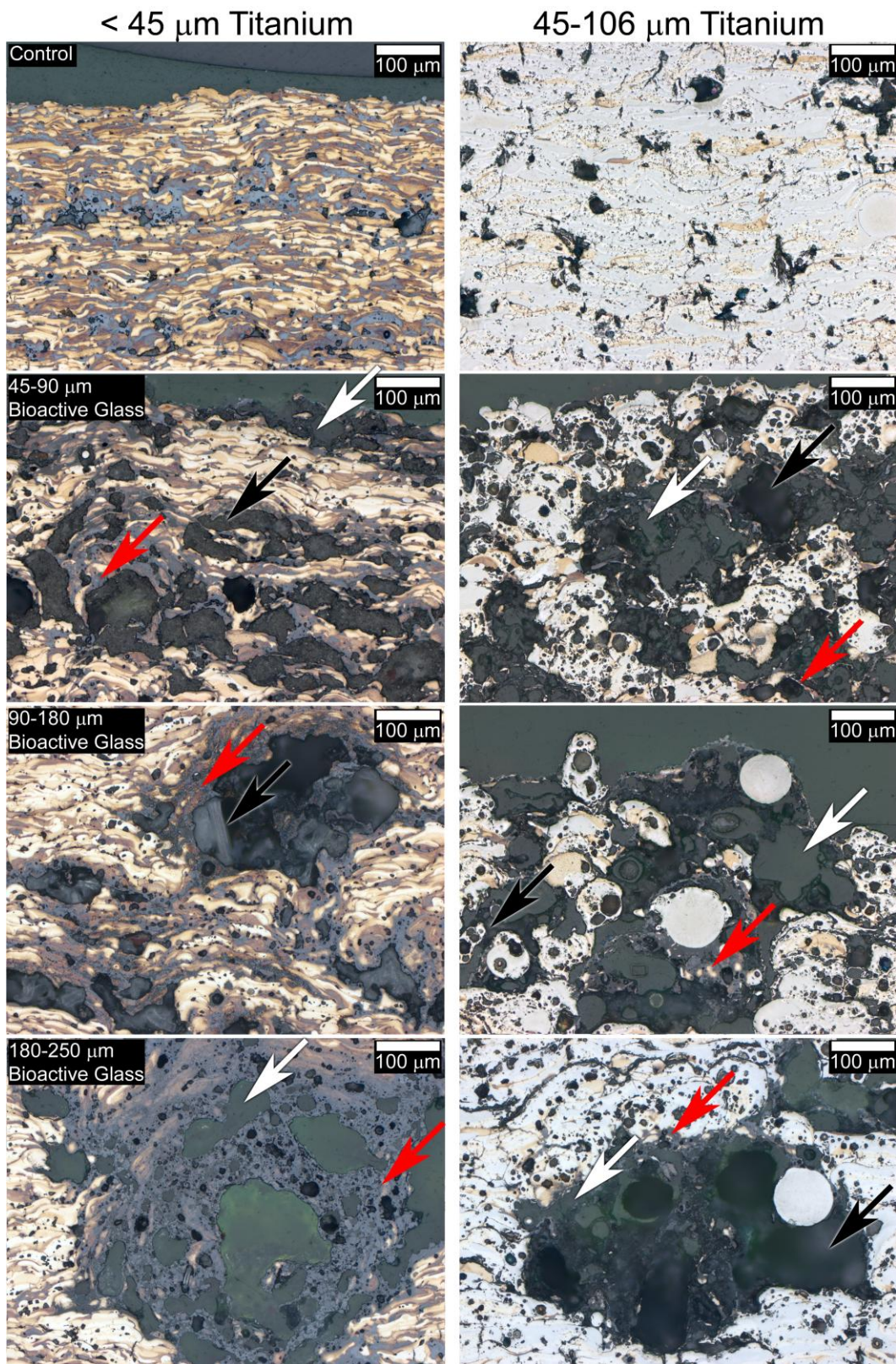


Figure 5-9. Representative cross-sectional optical micrographs of Cp-Ti-based coatings sprayed under the low flux deposition condition. Arrow legend: Black – Bioactive glass; Red – Reaction phase; White – Epoxy-filled pore.

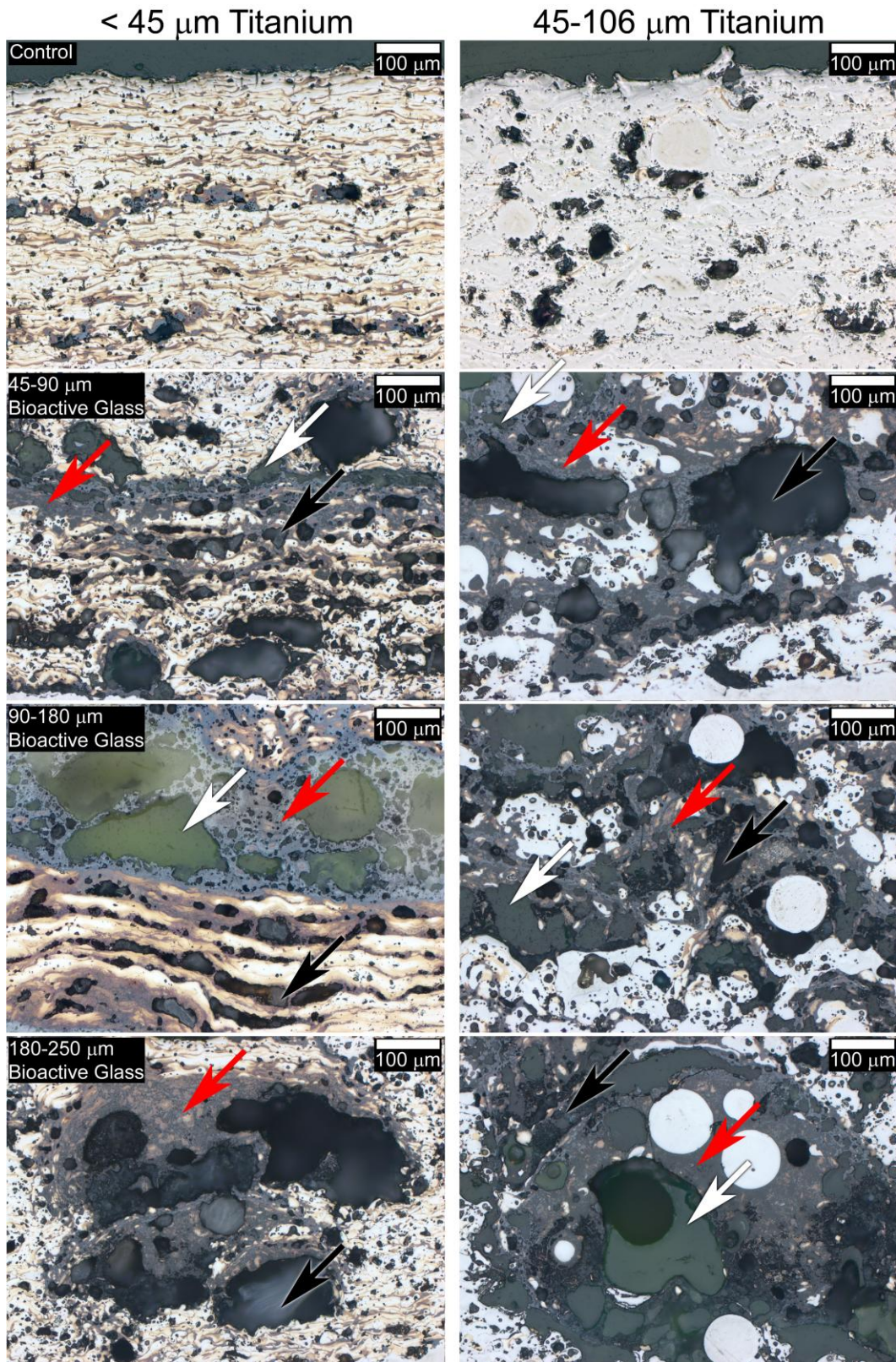


Figure 5-10. Representative cross-sectional optical micrographs of Cp-Ti-based coatings sprayed under the high flux deposition condition. Arrow legend: Black – Bioactive glass; Red – Reaction phase; White – Epoxy-filled pore.

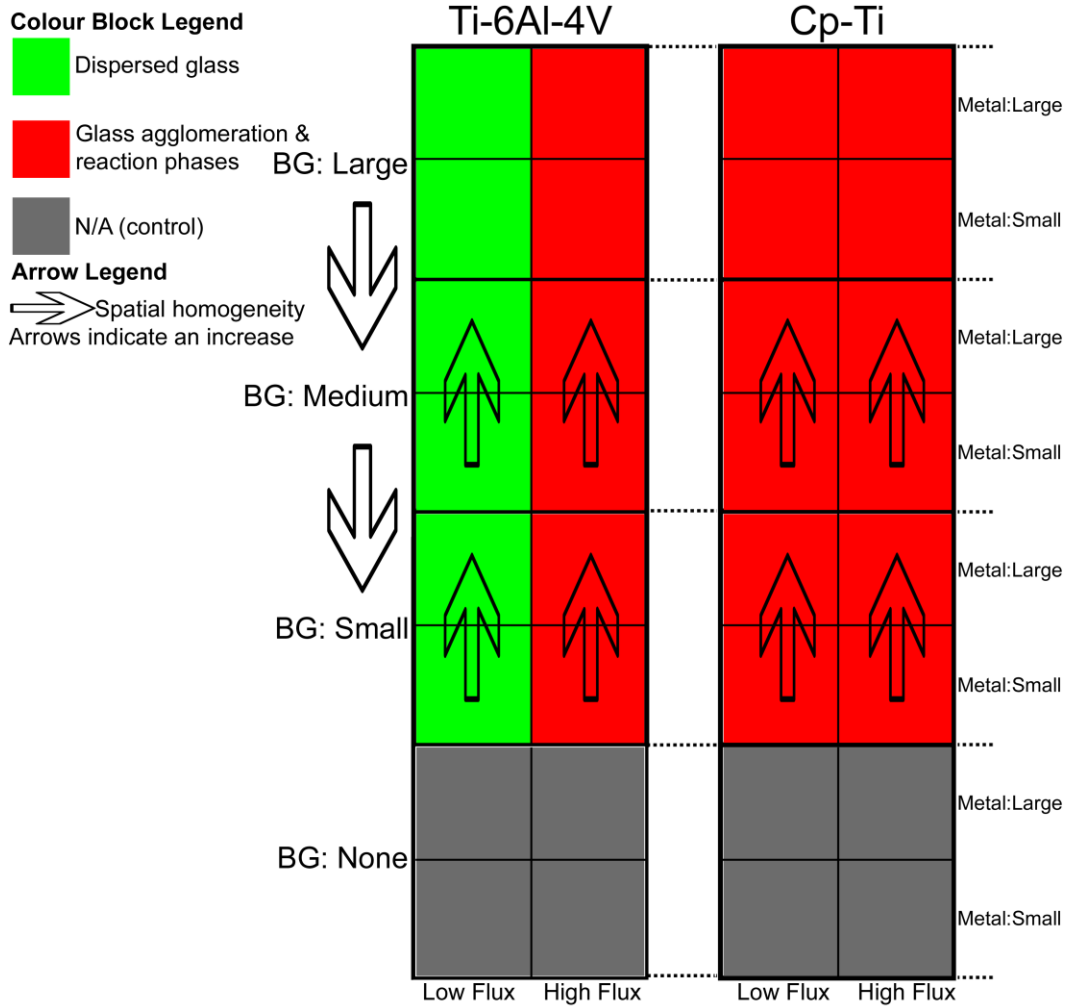


Figure 5-11. Schematic summary of the morphological and microstructural trends observed by optical microscopy. Each tile represents an individual combination of powder size, composition, and deposition condition. Legend: Metal - Small refers to < 45 μm powder and Large refers to 45 - 106 μm powder; Bioactive Glass: Small refers to 45 - 90 μm powder, Medium refers to 90 - 180 μm powder, and Large refers to 180 - 250 μm powder.

The addition of bioactive glass to the Cp-Ti or Ti-6Al-4V alloy powder resulted in a drastic change in microstructure and morphology of both the coating and its microconstituents. The previously angular and jagged bioactive glass powder particles (see Fig. 5-4) became either circular, as observed in the low flux Ti-6Al-4V-based composite coatings, or an interconnected globular phase, as observed in

all high flux coatings and the low flux Cp-Ti-based composite coatings. This rounding of the bioactive glass powder suggests that the softening temperature (550°C) was reached or exceeded during deposition [94]. Furthermore, there are regions that appear darker than the surrounding coating localized around the glassy phase, as observed in the high flux coatings and Cp-Ti-based composite coatings (see Fig. 5-8 to 5-10 and 5-12a). The localized phase was further analyzed with SEM with EDX (see Fig. 5-12b) and found to be rich in Ca, Ti, and O. Therefore, it is evident that this darker region corresponds to a reaction phase between the bioactive glass and the surrounding matrix which was present for all coatings deposited under the high flux condition and all Cp-Ti-based coatings. A schematized version of the presence of the reaction phase is included in Fig. 5-12c. Additionally, the specific heat capacity of Cp-Ti is approximately 10% lower than that of Ti-6Al-4V alloy at the same temperature [83,91,99]. Also, the thermal diffusivity of Cp-Ti is approximately 3 times larger than that of Ti-6Al-4V at the same temperature [83,91,99]; therefore, it would be reasonable to expect that a particle of Ti-6Al-4V alloy of the same size in same environment of would attain a lower temperature. Furthermore, it is possible that an endothermic reaction occurs during the deposition process that is related to the presence of aluminum and/or vanadium for Ti-6Al-4V-based coatings. When taken together these observations suggest that the bioactive glass and Cp-Ti particles may have reached higher temperatures during deposition or remained at higher temperatures for a longer duration allowing for reaction between the bioactive glass and the

surrounding matrix to occur for Cp-Ti-based coatings as well as for all composite coatings sprayed under the high flux deposition condition.

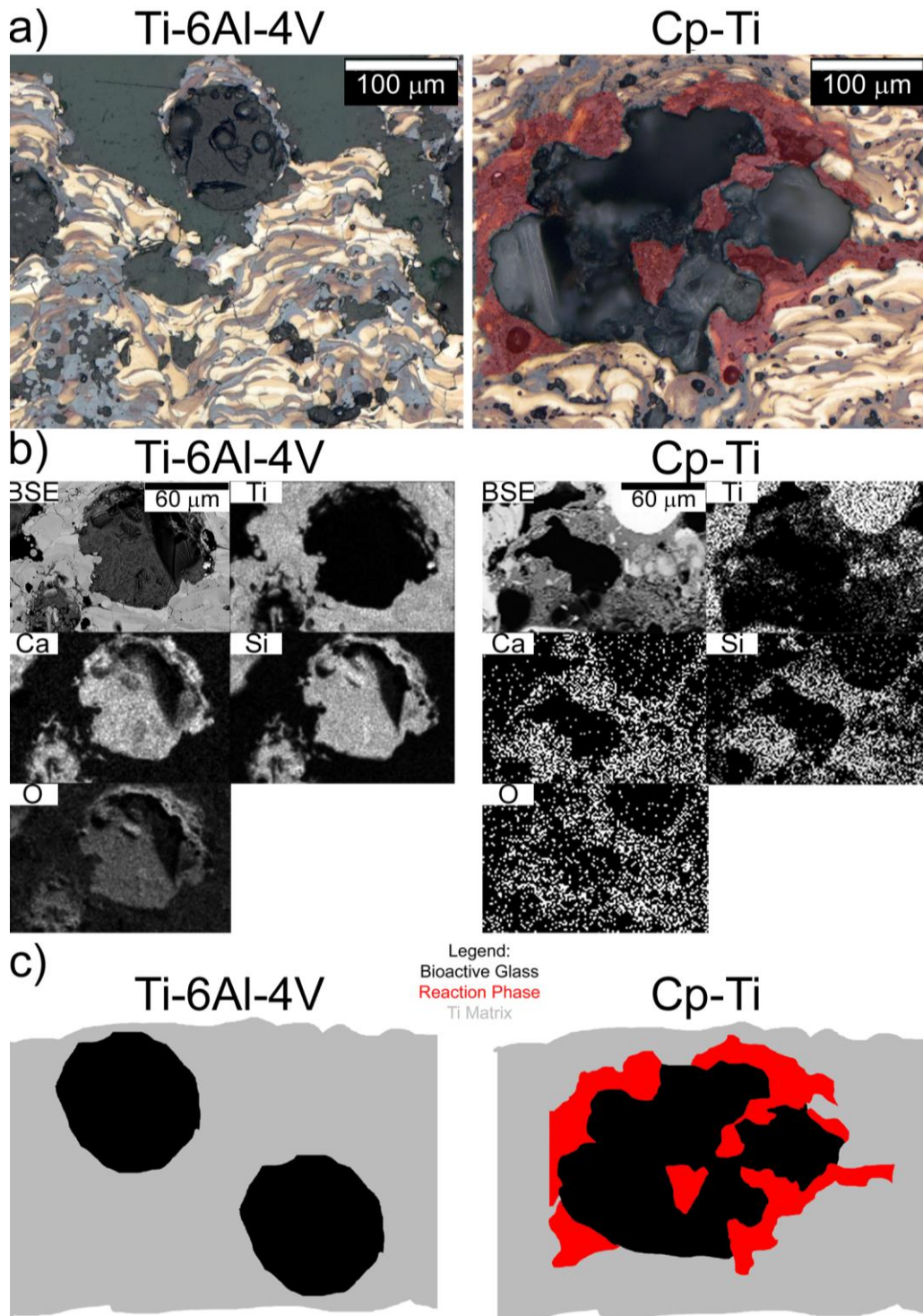


Figure 5-12. a. Optical cross-sectional micrographs of coatings deposited under the low flux condition demonstrating the presence of reaction phase (shaded red) for Cp-Ti-based coatings; b. Elemental mapping acquired by SEM with EDX localized around the glassy phase for coatings deposited under the low flux condition; c. Schematic representation of the glass morphology and reaction phase present within the microstructure for coatings deposited under the low flux condition

Within the microstructure of the coatings there are epoxy filled features (see red arrows in Fig. 5-7 to 5-10) that are surrounded by metal matrix or glassy phase. In order for these apparently closed features to be filled with epoxy the pore structure must be both open and interconnected. Therefore, it can be concluded that an open pore network exists which intersects with the glassy phase and provides access to sub-surface bioactive glass. However, whether or not the pore interconnectivity is conducive to tissue ingrowth would require *in vivo* testing accompanied by three dimensional imaging of the pore network and quantification of the diameter of the interconnectivity.

The coatings sprayed with 45 - 106 μm metallic powder appear to be more porous than the corresponding $< 45 \mu\text{m}$ metallic powder counterpart on qualitative comparison; the 45 - 106 μm metallic powder-based coatings exhibited a larger degree of intermixing as the bioactive glass, porosity and, reaction phases, if any, appeared to be distributed and dispersed more homogeneously throughout the structure (see Fig. 5-8 to 5-11). Furthermore, increasing the size of bioactive glass powder used in the coating also had a profound change on the structure. Selection of 90 - 180 μm bioactive glass over 45 - 90 μm bioactive glass powder decreased the portion of bioactive glass in each micrograph for low flux coatings. However, the incorporation of 180 - 250 μm bioactive glass resulted in a heterogeneous coating with significant regions devoid of bioactive glass and other regions consisting of bioactive glass and/or reaction phase (see Fig 5-7 to 5-11). The proportion of bioactive glass present within the coating for 180 - 250 μm

bioactive glass varied significantly with deposition condition and type of metallic alloy. That is, greater amounts of bioactive glass appeared to be present for 180 - 250 μm bioactive glass coatings when sprayed under the high flux condition, when blended with $< 45 \mu\text{m}$ metallic powder, and/or when blended with either Cp-Ti powder. However, the 180 - 250 μm bioactive glass coatings would be a poor candidate for load-bearing applications owing to the extremely heterogeneous nature of the distribution of the incorporated bioactive glass.

When sprayed under the high flux condition there was a dramatic change for both Ti-6Al-4V alloy and Cp-Ti-based composite coatings. The microstructure of Ti-6Al-4V-based composite consisted of large localized regions of the same darker phase as noted earlier mixed with lighter features (see Fig. 5-8, 5-10, and 5-11). These lighter features are likely particulates of Ti-6Al-4V alloy while the darker regions may consist of either a reaction phase and/or a blend of bioactive glass and Ti-6Al-4V alloy (see Fig. 5-12b). The presence of the darker regions and the intermixing could suggest that the bioactive glass reached or exceeded its melting temperature (1200°C) [94] or was held above its softening temperature for a significant portion of time. A similar dramatic change is seen in Cp-Ti-based composite coatings sprayed under the high flux condition. In this case, the same dark phase was spread throughout the microstructure rather than in localized zones of intermixing. The presence of the dark regions identified as reaction phase throughout the structure suggests that higher temperatures may have been attained in the deposition of Cp-Ti-based coatings than were reached for Ti-6Al-

4V-based coatings for the same reasons that were previously discussed. Further evidence of the relative temperatures attained during deposition will be presented in the discussion of the theoretical heat transfer model. Additionally, the presence of the darker phases and the changes in morphology suggest that when deposited under the high flux condition the metallic and bioactive glass particles reached a higher temperature than when deposited under the low flux condition. Alternatively, this may be due to heating of the substrate as the torch is positioned closer to the substrate, as compared with the low flux condition. It is reasonable to expect that the flame being closer to the substrate produced a greater degree of heating due to impingement of the flame on the coating and substrate.

The differences observed in the cross-sectional microstructure of the coating (see Fig. 5-11) suggest that the type of Cp-Ti or Ti-6Al-4V alloy has a significant impact on the final structure of the coating leading to larger degrees of intermixing and the presence of what may be a reaction phase suggesting that higher temperatures are reached while depositing Cp-Ti particles. The origin of this temperature difference is likely linked to the differences in thermophysical properties, such as heat capacity and thermal diffusivity, between Ti-6Al-4V alloy and Cp-Ti. Furthermore, selecting the high flux deposition condition results in a larger degree of glass-matrix intermixing and the generation of what may be a reaction phase. The selection of a larger metallic powder results in, qualitatively, a more spatially homogenous structure. The bioactive glass powder size used had a complex effect on the morphology of the final coating resulting in a less

homogenous coating with increasing particle size. Finally, it is important to note that a well dispersed and well distributed glassy phase is only of benefit when the bioactive glass intersects with an interconnected open pore network to allow for tissue ingrowth. Such an open pore network was shown to exist but further work is necessary to quantify the threedimensionality of the pore network.

5.5.2. Glass Content and Porosity

The quantitative glassy phase content and porosity of the coatings was measured through a semi-automated image processing routine of cross-sectional micrographs. The output of this routine was used to establish the percent porosity and glassy phase content as well as the area distributions of each. It was assumed that the area fraction of porosity in the metallurgical cross-sections was equivalent to the volume fraction of porosity in the entire coating. This assumption allows for a first-order estimation of the weight percent of incorporated bioactive glass; additionally, other studies of thermally sprayed coatings have assumed the equivalence between volumetric and area porosity [56,81]. A visual schematic was prepared to illustrate the trends presented and detailed herein related to the total porosity and bioactive glass content as a function of the manipulated variables (see Fig. 5-13 and 5-14).

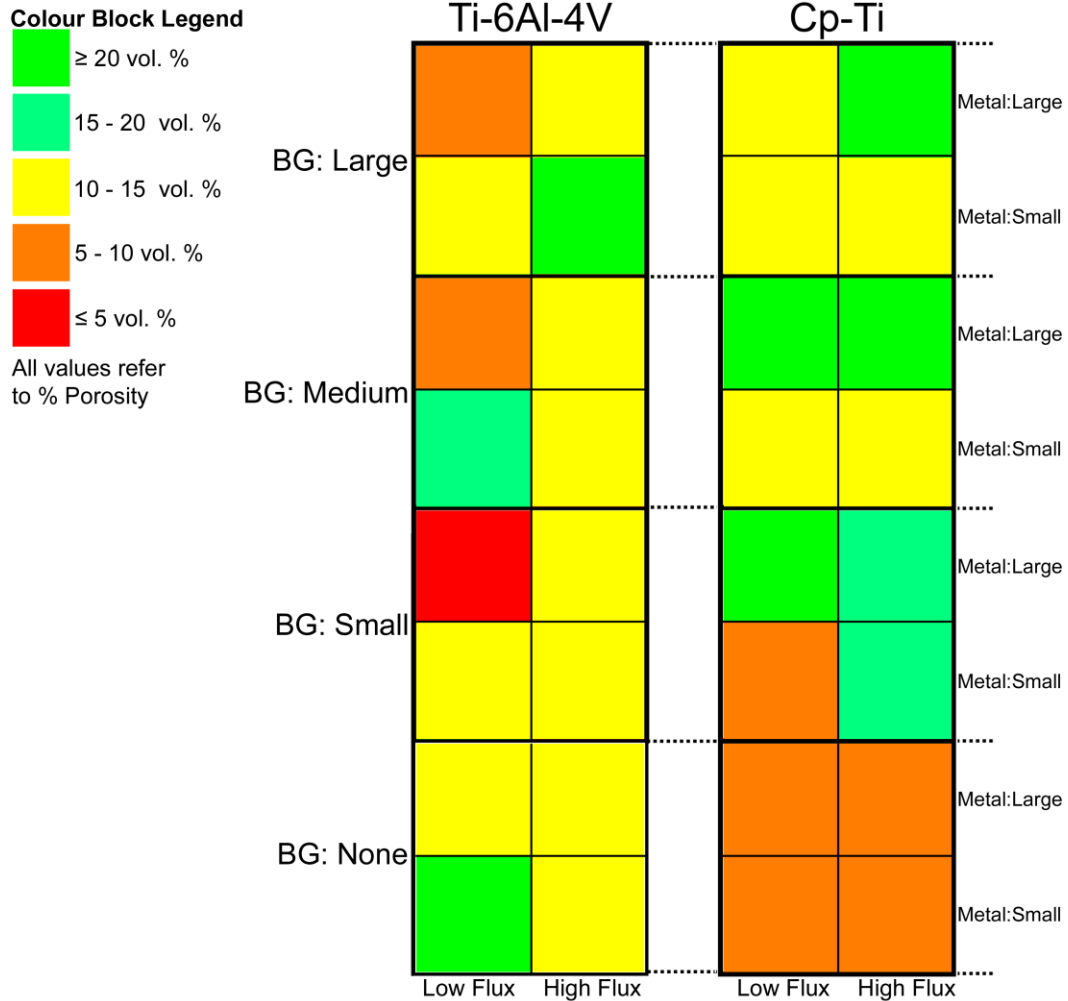


Figure 5-13. Schematic representation of the trends observed in the total porosity of the deposited coatings. Each tile represents an individual combination of powder size, composition, and deposition condition. Legend: Metal - Small refers to < 45 μm powder and Large refers to 45 - 106 μm powder; Bioactive Glass: Small refers to 45 - 90 μm powder, Medium refers to 90 - 180 μm powder, and Large refers to 180 - 250 μm powder.

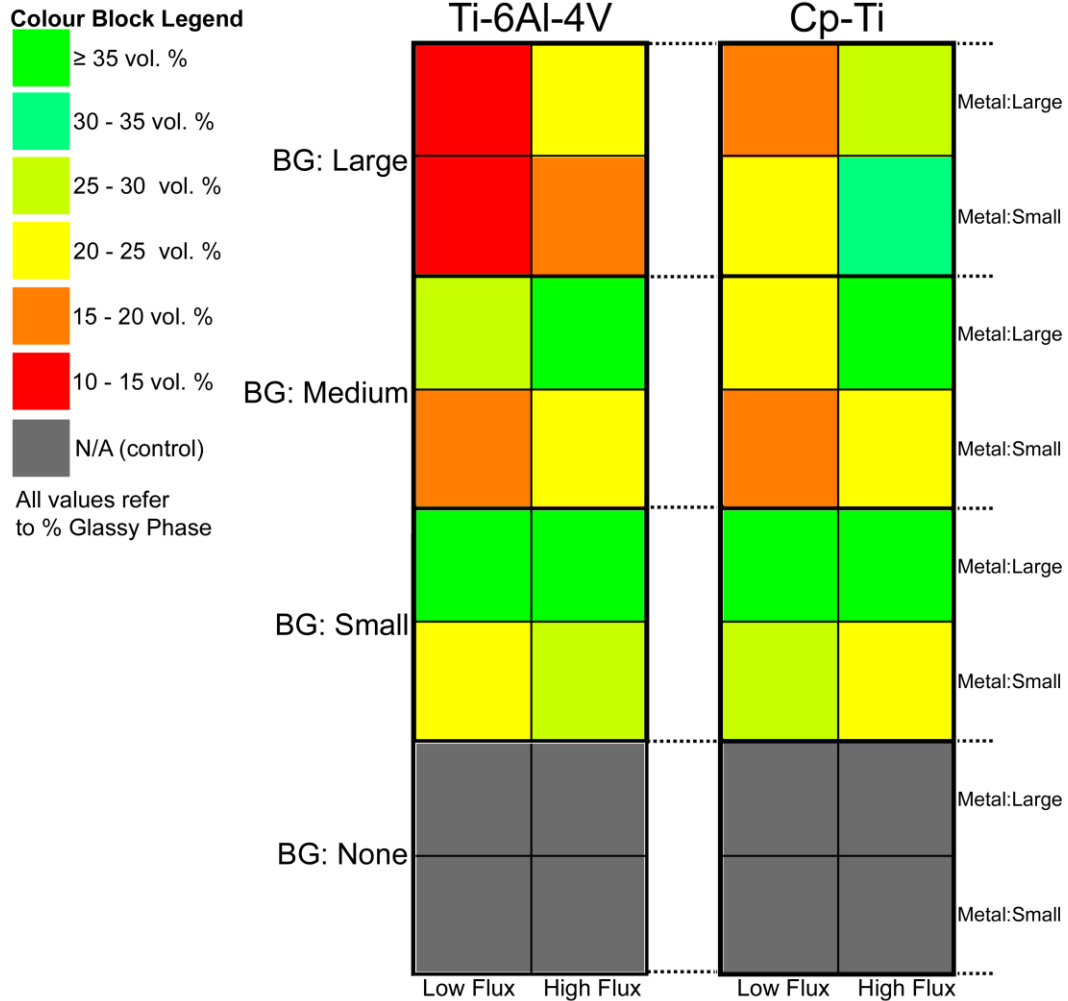


Figure 5-14. Schematic representation of the trends observed in the total glassy phase content of the deposited coatings. Each tile represents an individual combination of powder size, composition, and deposition condition. Legend: Metal - Small refers to $< 45 \mu\text{m}$ powder and Large refers to $45 - 106 \mu\text{m}$ powder; Bioactive Glass: Small refers to $45 - 90 \mu\text{m}$ powder, Medium refers to $90 - 180 \mu\text{m}$ powder, and Large refers to $180 - 250 \mu\text{m}$ powder.

To establish a baseline level for the effects of alloy choice, metallic particle size, and deposition condition the porosity of the control coatings was examined (see Table 5-3 and Fig. 5-13). The porosity was measured through image analysis of 12 micrographs ($n = 12$) that were acquired randomly from two coatings from the same deposition. The 95% confidence interval provided in Table 5-3 was calculated according to Eqn. 3-3 and statistical significance was determined by a

two-sample *T*-test according to Eqn. 3-5 or 3-6 after an *F*-test (see Eqn. 3-4) was used to determine whether or not the variances were equal. Coatings composed of Cp-Ti powder exhibited a greater degree of densification than those fabricated from Ti-6Al-4V alloy. Furthermore, alteration of the metallic powder size distribution did not have a statistically significant effect on the porosity of all control coatings with the exception of the low flux Ti-6Al-4V alloy coatings and high flux Cp-Ti coatings. In this case, the utilization of 45 - 106 μm Ti-6Al-4V alloy powder resulted in a substantially lower porosity while the opposite trend was observed for the high flux Cp-Ti-based coatings (see Fig. 5-13). The opposing trends suggest that a complex relationship may be present. Work conducted on the modified HVOF spraying of titanium by Kawakita *et al.* [100] and Kim *et al.* [101] indicated that an ideal but narrow range of particle sizes exists for a given powder and set of deposition conditions that will result in densification of the coating. This particle size range balances the particle surface area, particle mass, and particle velocity. Smaller particles oxidize and dissolve oxygen at a greater rate, owing to their greater surface area, but reach a higher temperature, and a higher velocity due to their lower masses. While larger particles will be less susceptible to oxidation and dissolution of oxygen but reach lower temperatures and lower velocities. Therefore, there is a particle size range which will balance the oxidation of the particles with the mechanical deformation upon impact leading to densification of the coating. Outside of this ideal particle size range an increase of porosity is observed which can be attributed to poor packing due significant oxide formation or insufficient deformation upon impact

with the substrate [100,101]. It should also be noted significant oxidation will lead to the inclusion of hard oxide particles which may be mechanically pulled out during sample preparation thus giving an apparent increase in porosity. The significant difference in porosity for low flux Ti-6Al-4V alloy control coatings and high flux Cp-Ti control coatings may be due to the effects as described previously.

Table 5-3. Summary of porosity for control coatings.

Condition	Metal Powder Size Range [μm]	Ti-6Al-4V	Cp-Ti
		Porosity [vol. %] ($n = 12$)	Porosity [vol. %] ($n = 12$)
Low Flux	0 to 45	25 ± 2	9 ± 1
	45 to 106	12 ± 1	7 ± 1
High Flux	0 to 45	11 ± 1	6 ± 1
	45 to 106	13 ± 2	9 ± 1

A statistically significant decrease in porosity was observed when spraying $< 45 \mu\text{m}$ Ti-6Al-4V powder and $< 45 \mu\text{m}$ Cp-Ti powder under the high flux deposition condition, 11 ± 1 vol. % and 6 ± 1 vol. % respectively, compared to the low flux condition, 25 ± 2 vol. % and 9 ± 1 vol. % respectively; while, a statistically significant increase in porosity was observed while spraying 45 - 106 μm Cp-Ti powder under the high flux deposition condition, 9 ± 1 vol. %, compared to the low flux condition, 7 ± 1 vol. %. The lack of a consistent trend, beyond the reduction in porosity observed for $< 45 \mu\text{m}$ metallic powder-based coatings, makes it difficult to establish how the high flux deposition condition alters porosity (see Fig. 5-13). Additionally, the comparison between the high flux and low flux conditions in terms of porosity is difficult as both the stand-off distance was decreased and the gaseous fuel flow rates were increased simultaneously.

Thermodynamic modeling demonstrated that a higher flame temperature and higher gas velocity resulted from such changes in stand-off distance and oxy-acetylene flow rate. It is also reasonable to expect that the decrease in stand-off distance and the increases in both flame temperature and gas velocity resulted in decreased particle residence times and increased substrate temperature. These factors impacted particle velocity, temperature, cooling rate, and degree of oxidation, which could have had a complex effect on coating porosity.

The porosity and glassy phase content of the composite coatings is summarized in Table 5-4 and the trends observed are represented in a visual schematic in Fig. 5-13 and Fig. 5-14. The error values provided are the 95% confidence interval calculated by Eqn 3-3. A total of 12 micrographs ($n = 12$) were used to establish the porosity and glassy phase content. The micrographs were taken randomly from two coatings deposited during the same flame spray deposition run. The addition of bioactive glass had a substantial effect on the porosity of the coating. However, it should be noted that the coatings containing 180 - 250 μm bioactive glass do not exhibit any clear trends for coatings deposited under the low flux condition. However, coatings containing 180 - 250 μm bioactive glass powder that were deposited under the high flux deposition condition displayed an increase in porosity relative to the corresponding coatings containing the smaller distributions of bioactive glass. The lack of clear trends for coatings containing the 180 - 250 μm bioactive glass powder that were fabricated under the low flux condition could be due to the extreme spatial heterogeneity observed in the cross-sectional microstructure (see Fig. 5-7 to 5-10). Therefore, the discussion of the

overall porosity and glassy phase content henceforth will be limited to that of coatings containing the two smaller size distributions of bioactive glass.

Table 5-4. Summary of porosity and glassy phase content for the composite coatings

Condition	Metal Powder Size Range [μm]	Bioactive Glass Powder Size Range [μm]	Ti-6Al-4V			Cp-Ti		
			Porosity [vol. %] (n = 12)	Glassy Phase [vol. %] [wt. %] (n = 12)		Porosity [vol. %] (n = 12)	Glassy Phase [vol. %] [wt. %] (n = 12)	
Low Flux	0 to 45	45 to 90	13 ± 4	25 ± 4	20 ± 3	8 ± 1	28 ± 3	21 ± 3
		90 to 180	18 ± 4	19 ± 1	15 ± 1	14 ± 6	19 ± 6	15 ± 4
		180 to 250	12 ± 4	12 ± 4	9 ± 3	13 ± 7	22 ± 9	17 ± 6
	45 to 106	45 to 90	5 ± 1	40 ± 3	30 ± 3	21 ± 5	35 ± 5	33 ± 4
		90 to 180	10 ± 4	28 ± 4	22 ± 3	29 ± 4	22 ± 5	21 ± 5
		180 to 250	7 ± 1	12 ± 5	8 ± 3	13 ± 3	20 ± 8	15 ± 6
High Flux	0 to 45	45 to 90	11 ± 3	26 ± 4	20 ± 3	15 ± 5	23 ± 4	18 ± 2
		90 to 180	12 ± 2	25 ± 5	19 ± 4	10 ± 3	21 ± 5	16 ± 4
		180 to 250	21 ± 4	17 ± 9	14 ± 8	19 ± 5	35 ± 5	28 ± 4
	45 to 106	45 to 90	11 ± 1	36 ± 5	29 ± 5	15 ± 4	43 ± 8	38 ± 7
		90 to 180	13 ± 3	38 ± 5	32 ± 5	20 ± 5	36 ± 9	33 ± 8
		180 to 250	21 ± 4	17 ± 9	19 ± 10	24 ± 2	28 ± 8	26 ± 9

The effect of increasing the bioactive glass size differs depending on whether the coating was deposited under the low or high flux deposition condition. It is clear upon comparing the porosity values that those coatings containing 90 - 180 μm instead of 45 - 90 μm bioactive glass powder displayed a higher degree of porosity and both lower volume and weight percentage of bioactive glass for coatings fabricated under the low flux deposition condition while there is no statistically significant trend under the high flux deposition condition. A decrease in weight percent of the retained glassy phase is noted with increasing bioactive powder size for all coatings fabricated under the low flux deposition condition. While, no clear trend exists when increasing bioactive glass particle size for coatings fabricated under the high flux condition.

The type of metallic powder that forms the matrix does not have a statistically significant effect on the volume or weight percent of bioactive glass incorporated into the coating regardless of deposition condition or whether the coating contained 45 - 90 μm bioactive glass or 90 - 180 μm bioactive glass. However, there are several significant effects on the porosity based on the type of titanium that composes the matrix of the coating. Coatings fabricated from $< 45 \mu\text{m}$ Cp-Ti powder under the low flux deposition condition were less or comparably porous to their Ti-6Al-4V-based composite coatings counterparts. However, when 45 - 106 μm metallic powder was deposited under the low flux deposition condition the porosity of Ti-6Al-4V-based composite coating was significantly lower than that of the Cp-Ti-based composite coating. The higher porosity is unexpected as the control coating data (see Table 5-3) suggested that Cp-Ti-based coatings would have a lower porosity than the corresponding Ti-6Al-4V alloy coating. However, the significantly higher porosity observed for the Cp-Ti-based coatings fabricated from 45 - 106 μm metallic powder may be due to the large pore area localized around the bioactive glass. The additional pore area localized around the bioactive glass may be due to titanium-bioactive glass interactions and/or chemical reactions. For coatings fabricated under the high flux deposition condition, there is no statistically significant difference in porosity based upon on the type of metallic powder with the exception of the coatings fabricated from 45 - 106 μm metallic powder blended with 90 - 180 μm bioactive glass; in the case of the aforementioned exception, the Cp-Ti-based coating was significantly more porous. Additionally, localization of pores in proximity to bioactive glass was

again observed (see Fig. 5-10). Possible explanations for the localization of pore area around bioactive glass for the Cp-Ti-based coatings demonstrating significantly higher porosity include: poor stacking, viscous flow of molten glass, localized boiling of one or more component, localized reactions evolving gas, and splashing of molten particles. As before, comparing the low flux and corresponding high flux coatings reveals no clear trend in terms of porosity.

5.5.2.1. Pore and Glassy Phase Size Distribution

To analyze the size of the features measured through image analysis a distribution by feature area was selected. The selection of a distribution by feature area over an equivalent circular diameter was made because of the non-circularity of many of the pores as well as the agglomeration observed for high flux coatings and Cp-Ti-based coatings (see Fig. 5-7 to 5-10). The measured pore and glassy phase area was binned by order of magnitude. The area was binned to accommodate the diverse range of feature area that ranged from 1 to 100,000 μm^2 . The value of each bin is the fraction of the total feature area in that bin to the total coating area. Therefore, summation of the plotted value from each bin yields the total porosity or glassy phase fraction of that coating (as shown in Table 5-3 and 5-4). This approach was selected over a traditional histogram because it gives a better understanding of what proportion of the pore or glassy phase area lies in each size range. The importance of the proportion of the pore area in larger size regimes is due to the ability of pores of that size to promote integration. Further, larger glassy features also represent soluble porogens that may produce pores suitable

for ingrowth in the “changing landscape coatings” as bioactive glass will dissolve in *vivo* [2,3]. Pores that are either 1000 to 10,000 μm^2 or greater than 10,000 μm^2 in area are of particular importance [18]. These pores correspond to an equivalent diameter of 36 and 112 μm , respectively. A study by Klenke *et al.* [11] showed that pore diameters of at least 80 μm promoted significant ingrowth of bone tissue into the pores, osseointegration, and promoted the development of vascular tissue; while, work by Underwood *et al.* [12] found that epidermal tissue ingrowth and vascularization occurs with pore diameters between 40 to 60 μm . Therefore, pores between 1000 to 10,000 μm^2 or in excess of 10,000 μm^2 are of vital importance to promoting viable tissue ingrowth and osseointegration of the coatings and to the success of the changing landscape coating concept. Pores with areas in excess of 1000 μm^2 will be referred to as suitable porosity or pores of suitable size henceforth. The trends observed in the portion of pores with areas that were suitable for tissue ingrowth are summarized in the form of a visual schematic in Fig. 5-15; additionally, trends observed in the portion of bioactive glass with areas that were suitable for producing a pore after dissolution for tissue ingrowth are summarized in another visual schematic in Fig. 5-16.

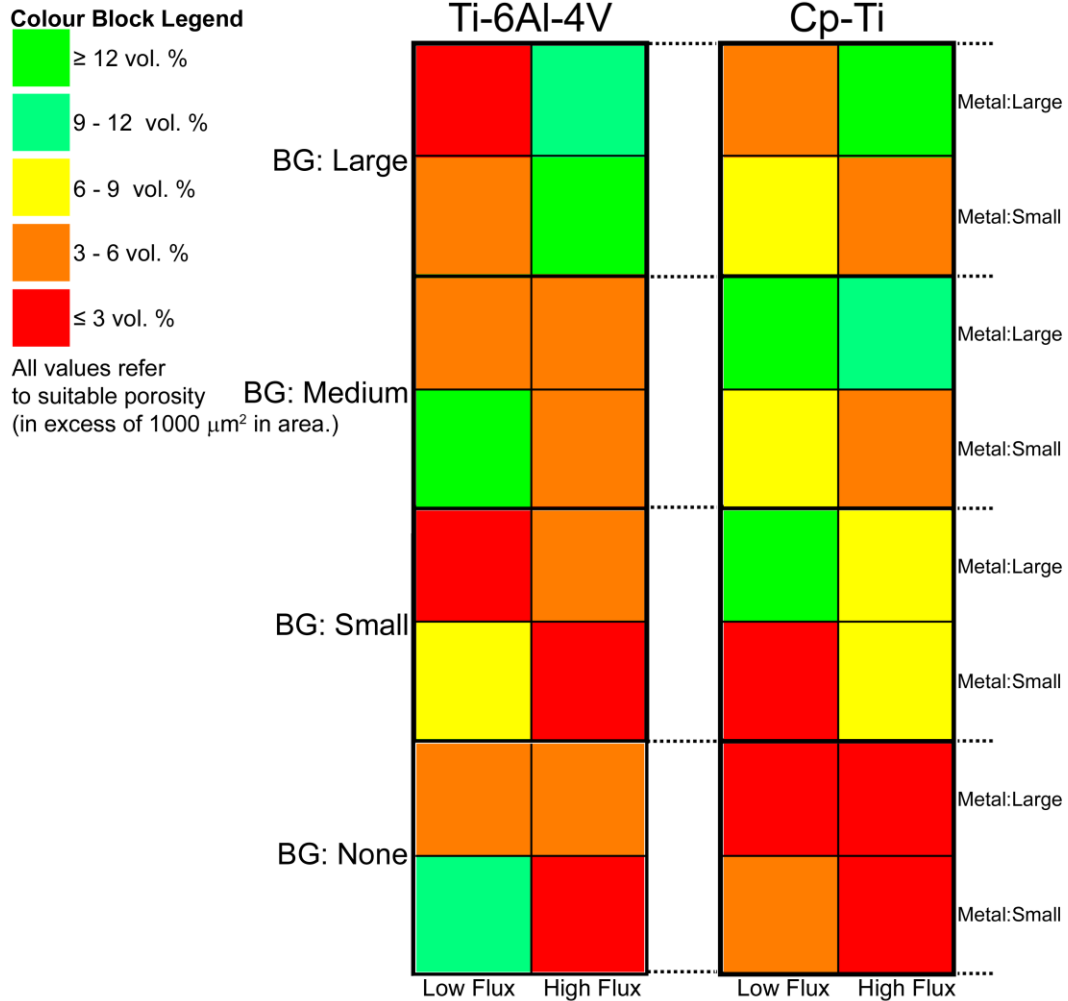


Figure 5-15. Schematic representation of the trends observed in the portion of porosity with areas that would be suitable for the ingrowth of bone tissue. Each tile represents an individual combination of powder size, composition, and deposition condition. Legend: Metal - Small refers to $< 45 \mu\text{m}$ powder and Large refers to $45 - 106 \mu\text{m}$ powder; Bioactive Glass: Small refers to $45 - 90 \mu\text{m}$ powder, Medium refers to $90 - 180 \mu\text{m}$ powder, and Large refers to $180 - 250 \mu\text{m}$ powder.

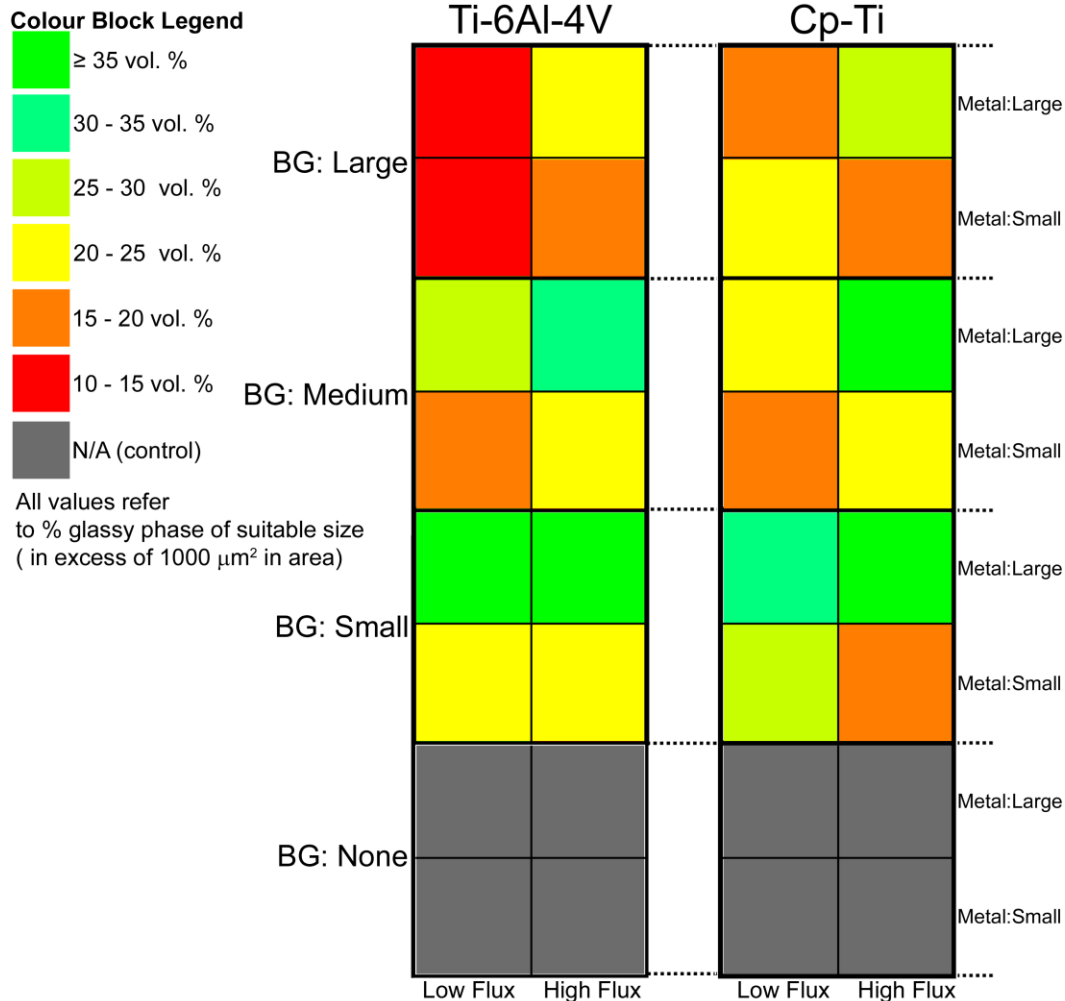


Figure 5-16. Schematic representation of the trends observed in the portion of glassy phase with areas that would be suitable for producing pores conducive to the ingrowth of bone tissue. Each tile represents an individual combination of powder size, composition, and deposition condition. Legend: Metal - Small refers to $< 45 \mu\text{m}$ powder and Large refers to $45 - 106 \mu\text{m}$ powder; Bioactive Glass: Small refers to $45 - 90 \mu\text{m}$ powder, Medium refers to $90 - 180 \mu\text{m}$ powder, and Large refers to $180 - 250 \mu\text{m}$ powder.

The control coatings (see Fig. 5-17 and 5-18) exhibited no pores in excess of $10,000 \mu\text{m}^2$. Also, only a small portion of the pore area was of suitable size for the control coatings with the exception of $< 45 \mu\text{m}$ Ti-6Al-4V alloy powder sprayed under the low flux deposition condition. The incorporation of bioactive glass into the composite coatings had a significant effect on the porosity of the

coatings. However, the behaviour of the 180 - 250 μm bioactive glass coating was contrary to the other coatings. The proportion of suitable pores was reduced when the size distribution of the metallic powder was increased. Additionally a greater proportion of suitable pores were observed in the coating when the powder blends were deposited under the high flux condition or Cp-Ti was used to form the matrix of the coating. Why this occurred is unclear but it may be due to localized interactions that occur between the bioactive glass particles and the metallic matrix. The particles may attain a higher temperature, owing to either a smaller diameter or the previously discussed smaller specific heat and larger thermal diffusivity of Cp-Ti, and thus better able to capture or react with the bioactive glass particle. Additionally, the extreme heterogeneity of the spatial distribution of porosity and bioactive glass in coatings containing 180 - 250 μm bioactive glass (see Fig. 5-7 to 5-10) means that the integration and ingrowth of tissue may be localized rather than homogenous throughout the coating; therefore, the coatings containing 180 - 250 μm bioactive glass are likely poor candidates for a changing landscape coating used in load-bearing applications. The discussion henceforth will focus on the coatings fabricated from the 45 - 90 μm and 90 - 180 μm bioactive glass powders.

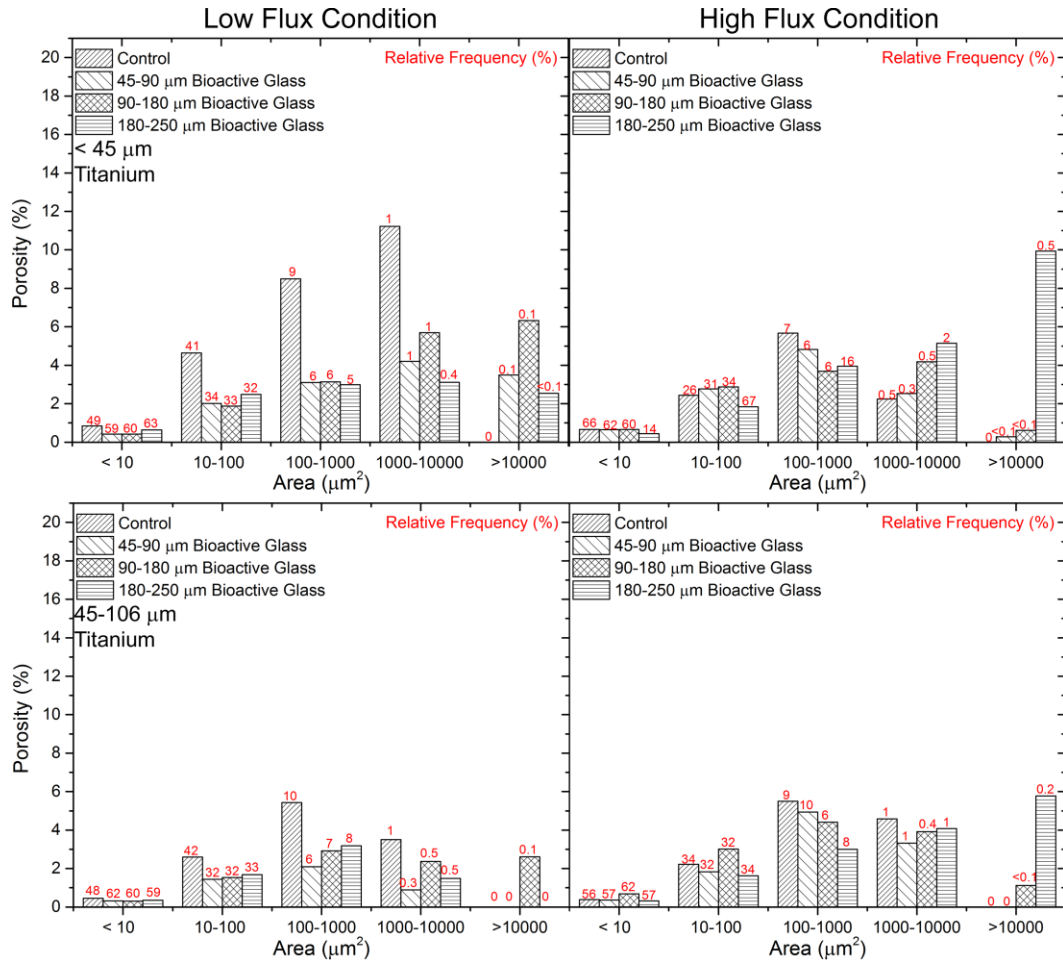


Figure 5-17. Porosity distribution by area for Ti-6Al-4V-based composite coatings binned by order of magnitude. The top plots correspond to coatings fabricated from <math>< 45 \mu\text{m}</math> metallic powder while the bottom plots correspond to coatings fabricated from 45 - 106 $\mu\text{m}</math> metallic powder. The relative frequency (number frequency) of features with areas in each size range is indicated above each bar.$

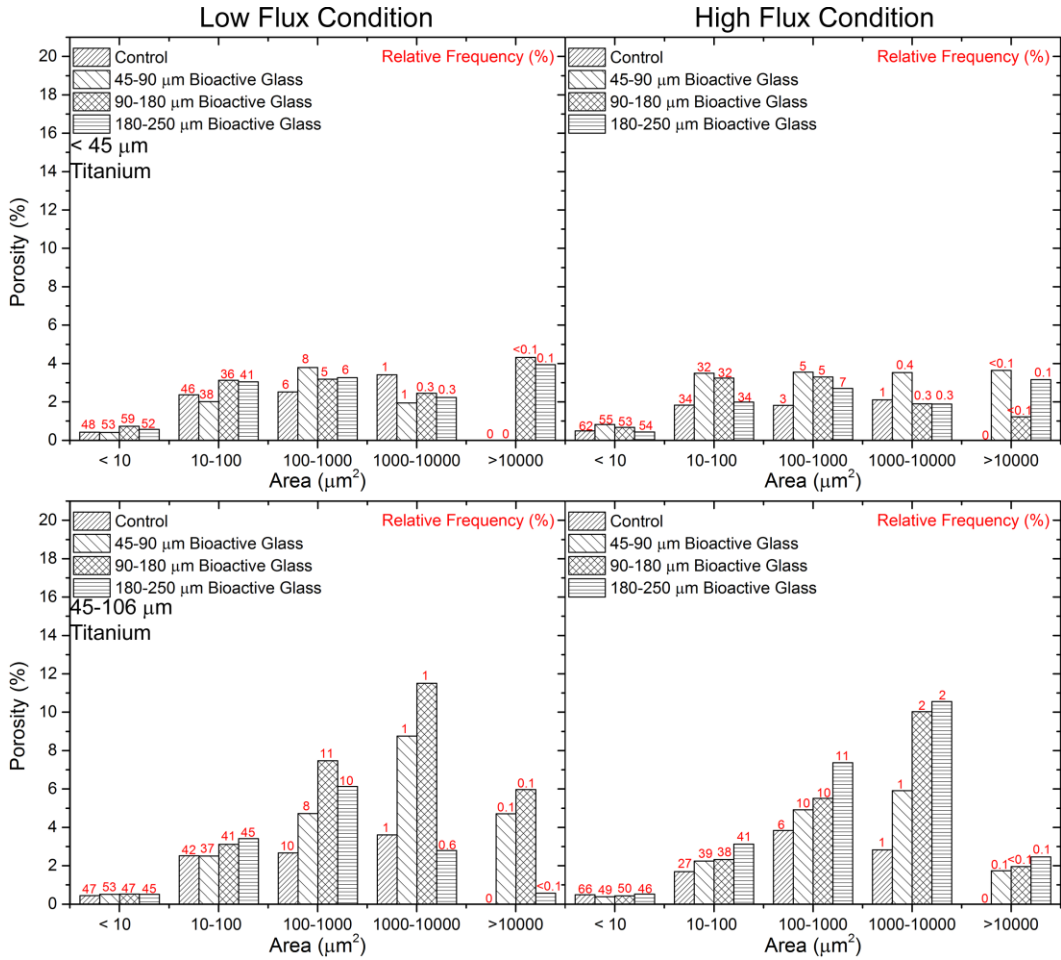


Figure 5-18. Porosity distribution by area for Cp-Ti-based composite coatings binned by order of magnitude. The top plots correspond to coatings fabricated from < 45 μm metallic powder while the bottom plots correspond to coatings fabricated from 45 - 106 μm metallic powder. The relative frequency (number frequency) of features with areas in each size range is indicated above each bar.

The low flux composite coatings (see Fig. 5-17 and 5-18; left images) demonstrated that coatings fabricated from Cp-Ti powder, in the < 45 μm particle size range, possessed a greatly reduced portion of suitable porosity compared to the corresponding Ti-6Al-4V-based coatings. The opposite trend was observed when 45 - 106 μm metallic powder was sprayed under the low flux condition. A decreased proportion of suitable porosity was observed for coatings fabricated from Ti-6Al-4V alloy in the 45 to 106 μm particle size range relative to the

corresponding Cp-Ti-based coating. However, the increase in the proportion of suitable porosity for coatings fabricated from 45 to 106 μm Cp-Ti powder, compared to coatings fabricated from 45 to 106 μm Ti-6Al-4V powder, is attributed to the aforementioned localized interaction phase and localized pore volume around the bioactive glass.

When the bioactive glass powder size was increased from 45 - 90 μm to 90 - 180 μm an increased proportion of suitable porosity was observed for all coatings with the exception of coatings based upon $< 45 \mu\text{m}$ metallic powder sprayed under the high flux condition which shows a negligible change. Therefore, bioactive glass in the 90 to 180 μm range is desirable to promote a greater volume of suitable pores as coatings with a substantial proportion of suitable pores are likely to promote a greater degree of tissue ingrowth and vascularization compared to a coating possessing fewer suitable pores. However, the use of 90 to 180 μm bioactive was shown to give a less spatially homogenous structure (see Fig. 5.7 to 5.10). Therefore, it is speculated that the use of an intermediate size range that encompasses a portion of both 45 to 90 μm and 90 to 180 μm would offer both a spatially homogenous structure and a larger proportion of porosity in the size regimes of interest.

Coatings sprayed under the high flux deposition condition (see Fig. 5-17 and 5-18; right images) exhibited similar trends to those noted above. Coatings sprayed under the high flux deposition parameters with 45 to 90 μm and 90 to 180 μm

bioactive glass powders show pore size distributions that are similar to their low flux counterparts. One expectation is the reduction of suitable pores for $< 45 \mu\text{m}$ metallic powder-based coatings when mixed with the $90 - 180 \mu\text{m}$ bioactive glass powder and sprayed under the high flux condition. Additionally, there is a reduction in the portion of suitable pores noted for $< 45 \mu\text{m}$ metallic powder-based coatings when sprayed under the high flux deposition condition (compared to the coatings deposited under the low flux deposition condition) with the exception of the coating fabricated from $< 45 \mu\text{m}$ Cp-Ti blended with $45 - 90 \mu\text{m}$ bioactive glass which showed a decrease. While no clear trend was demonstrated for coatings fabricated from $45 - 106 \mu\text{m}$ powder. It is difficult to predict what effects the high flux condition should have on the porosity and further systematic study may be necessary to decouple the effects of the substrate temperature with the gaseous flow rates to a gain meaningful understanding of the changes exhibited here.

In summary, the composite coatings studied contained suitable pores that would promote osseointegration when sprayed under both the low flux and high flux conditions. The addition of bioactive glass increased the proportion of pore area that would promote integration; however, a reduction in proportion of total suitable pores was noted when bioactive glass was added to the $< 45 \mu\text{m}$ Ti-6Al-4V alloy coatings. Despite the reduction observed for the $< 45 \mu\text{m}$ Ti-6Al-4V-based coatings the incorporation of bioactive glass should provide osteoproduative capabilities justifying the selection of a composite coating. It

was also noted that increasing the bioactive glass particle size to 90 to 180 μm from 45 to 90 μm generated a greater proportion of suitable pores corresponding to the pore areas between 1000 to 10,000 μm^2 and greater than 10,000 μm^2 , however the total magnitude of suitable porosity could, and should, be determined for these coatings through performance of *in vivo* testing

The most promising coatings are those that possess a significant portion of suitable pores (see Fig. 5-15, 5-18, and 5-19), those with areas in excess of 1000 μm^2 , for promoting the viable ingrowth of tissue while maintaining some degree of homogeneity in the spatial distribution of the bioactive glass. The most promising composite coatings on the basis of structure and suitable porosity are: < 45 μm Ti-6Al-4V alloy blended with 90 - 180 μm bioactive glass sprayed under the low flux condition, 45 - 106 μm Cp-Ti blended with 90 - 180 μm bioactive glass sprayed under low flux, 45 to 106 μm Cp-Ti blended with 45 - 90 μm bioactive glass sprayed under low flux and 45 to 106 μm Cp-Ti blended with 90 - 180 μm bioactive glass sprayed under the high flux condition. Other coating combinations did not possess both a large portion of suitable pores and spatially homogenous structures; for example, 45 - 106 μm Ti-6Al-4V alloy blended with 90 to 180 μm bioactive glass had a more spatially homogenous structure but a lower portion of suitable pores when compared to the corresponding < 45 μm Ti-6Al-4V alloy coating. Exploring an intermediate bioactive glass size range and/or metallic powder size range may also represent an avenue to obtain a balance between the spatial homogeneity and the portion of suitable pores.

The distribution of the glassy phase as shown in Fig. 5-19 and 5-20 shows a number of trends. First, the Cp-Ti shows a higher degree of glassy phase incorporated (see Table 5-4 and Fig. 5-19 and 5-20) for coatings containing with 180 to 250 μm bioactive glass when compared to their Ti-6Al-4V-based counterparts. If the incorporation of bioactive glass of this size was difficult due to lack of sufficient heating and softening then it could be that the higher temperature Cp-Ti particles were more easily able to capture the large particles of bioactive glass. Additionally, the high flux deposition condition had a higher proportion of glassy phase with areas corresponding to the size range between 1000 and 10,000 μm^2 and those in excess of 10,000 μm^2 . Bioactive glass with areas in excess of 1000 μm^2 will create a pore, after dissolution, which would encourage integration and bone growth. Additionally, Cp-Ti-based coatings that contain 45 - 90 μm bioactive glass possess a much higher proportion of bioactive glass in the greater than 10,000 μm^2 than the corresponding Ti-6Al-4V-based coating. The increase in the greater than 10,000 μm^2 size range of glassy phase was likely due to the agglomeration of glassy phase indicated by the optical micrographs (Fig. 5-7 to 5-10).

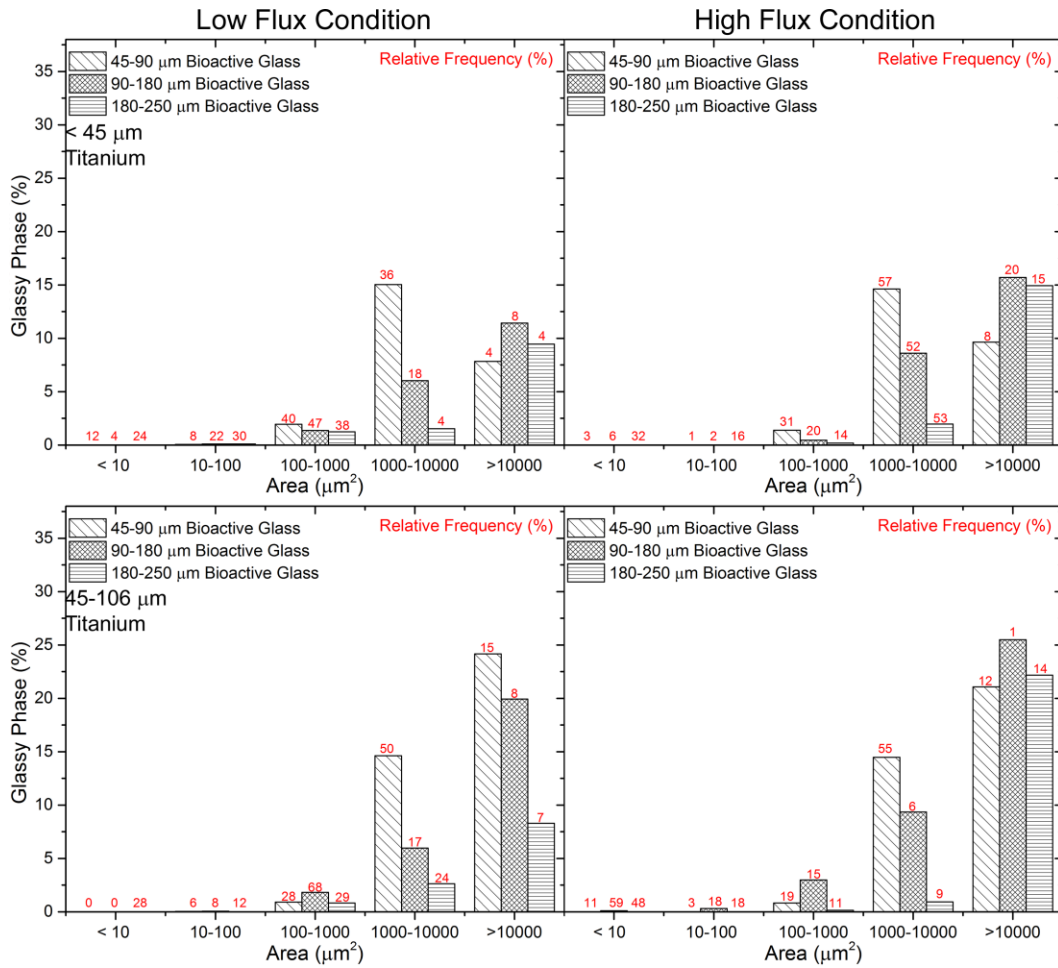


Figure 5-19. Glassy phase distribution by area for Ti-6Al-4V-based composite coatings binned by order of magnitude. The top plots correspond to coatings fabricated from $< 45 \mu\text{m}$ metallic powder while the bottom plots correspond to coatings fabricated from 45 - 106 μm metallic powder. The relative frequency (number frequency) of features with areas in each size range is indicated above each bar.

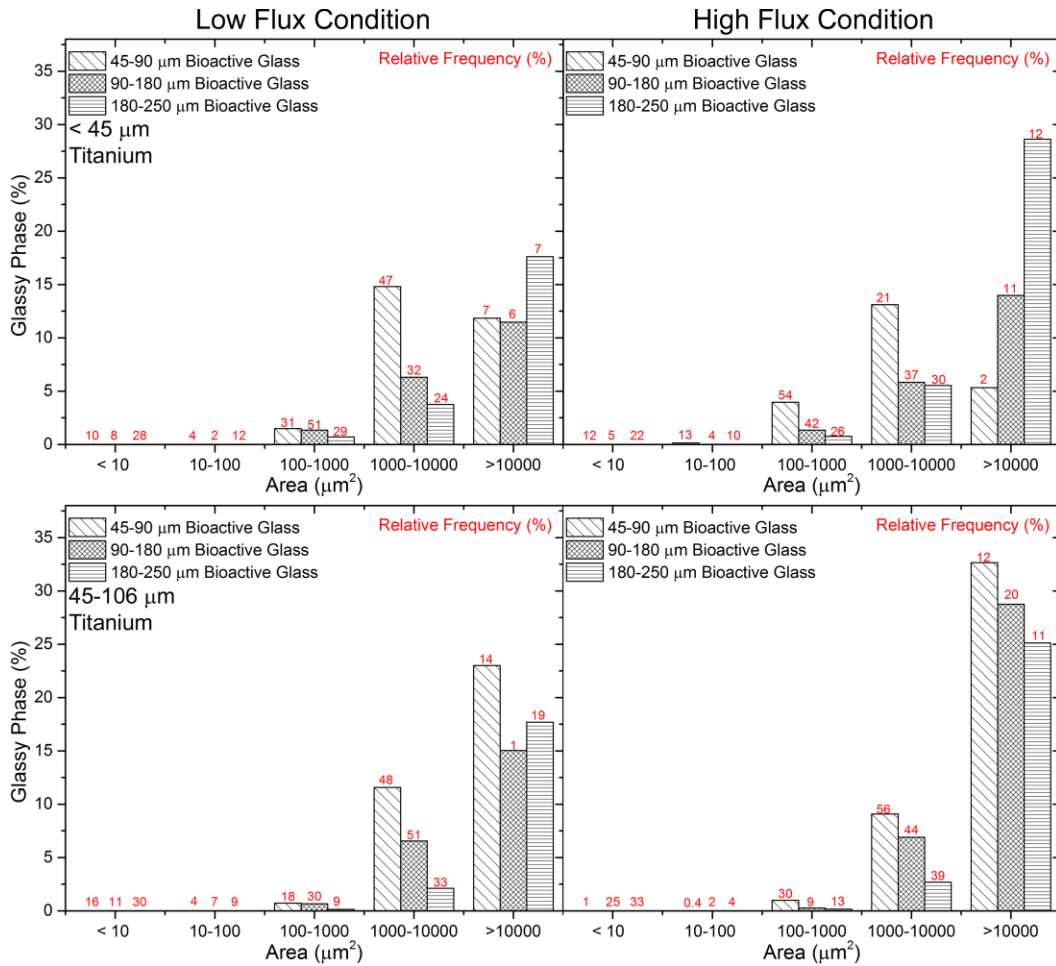


Figure 5-20. Glassy phase distribution by area for Cp-Ti-based composite coatings binned by order of magnitude. The top plots correspond to coatings fabricated from < 45 μm metallic powder while the bottom plots correspond to coatings fabricated from 45 - 106 μm metallic powder. The relative frequency (number frequency) of features with areas in each size range is indicated above each bar.

5.5.3. X-ray Diffraction (XRD)

The phase composition of each coating was assessed via XRD and the representative patterns are presented in Fig. 5-21 and 5-22. Shifting of peak positions was expected due to both the operation in parallel beam mode and sample surface roughness [102]. Additionally, altered peak intensities may be observed due to preferred orientation [102]. The trends discussed herein are summarized in a visual schematic form included in Fig. 5-23. Several phases were

found to be common among every composite coating and control coating, namely titanium suboxide (TiO_x), metallic titanium, the rutile phase of titanium dioxide (TiO_2), and the anatase phase of TiO_2 . However, the peaks corresponding to the rutile phase were absent for the control coatings fabricated from 45 - 106 μm Ti-6Al-4V alloy powder sprayed under the high flux deposition condition. Peaks assigned to the titanium (III) oxide (Ti_2O_3) were observed for Cp-Ti-based composite coatings and Cp-Ti control coatings. Peaks for a vanadium substituted titanium (III) oxide ($\text{Ti,V})_2\text{O}_3$ were observed for Ti-6Al-4V alloy control coatings as well as Ti-6Al-4V-based composite coatings. Cp-Ti-based composite coatings also showed peaks that matched perovskite (CaTiO_3) and combeite ($\text{Na}_2\text{Ca}_2\text{Si}_3\text{O}_9$). Combeite and perovskite were not observed for Ti-6Al-4V-based coatings fabricated under the low flux condition, except for the low signal to noise ratio peaks observed in the case of the coating fabricated from a blend of 90 - 180 μm bioactive glass and 45 - 106 μm Ti-6Al-4V alloy powder. Furthermore, peaks that matched to perovskite, combeite, and titanite (CaTiSiO_5) were present when composite coatings were sprayed under the high flux deposition condition.

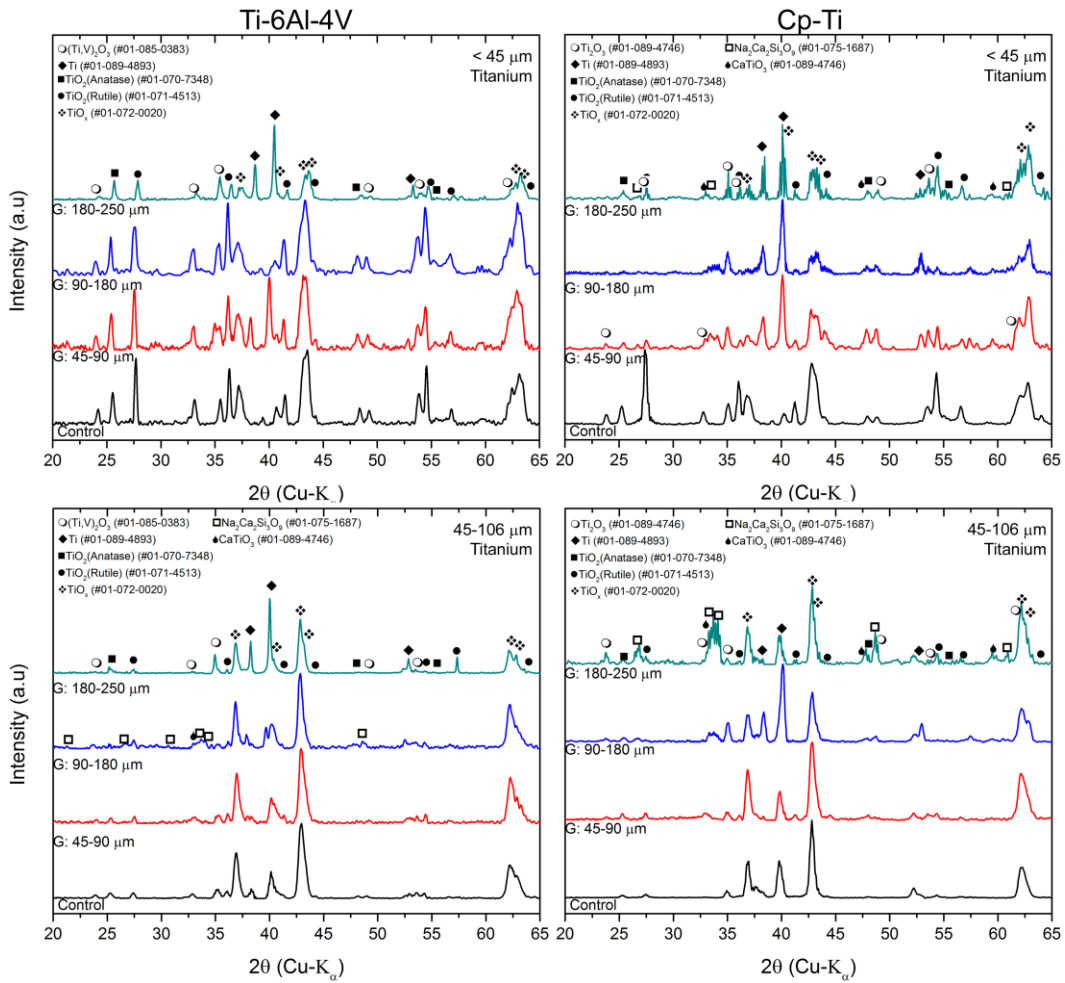


Figure 5-21. XRD patterns collected from coatings sprayed under the low flux condition.

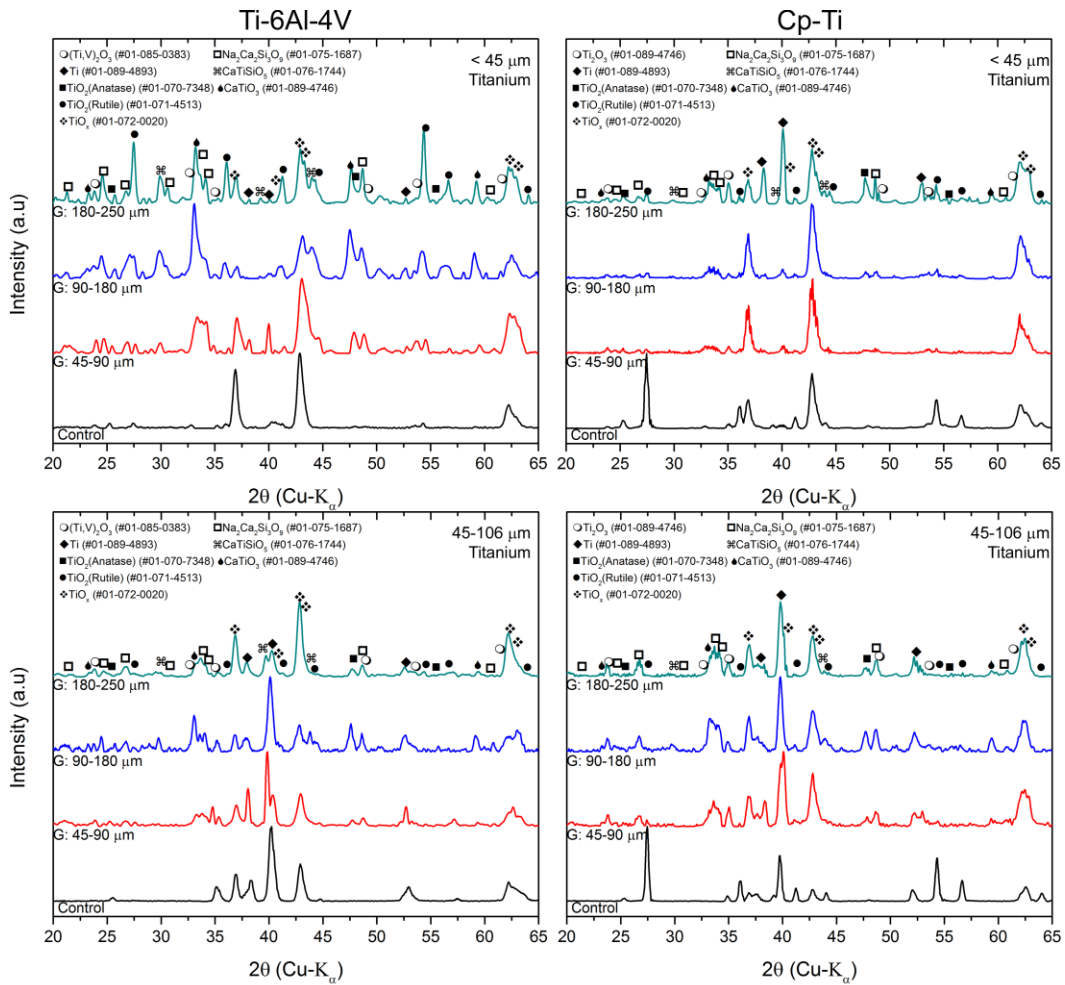


Figure 5-22. XRD patterns collected from coatings sprayed under the high flux condition.

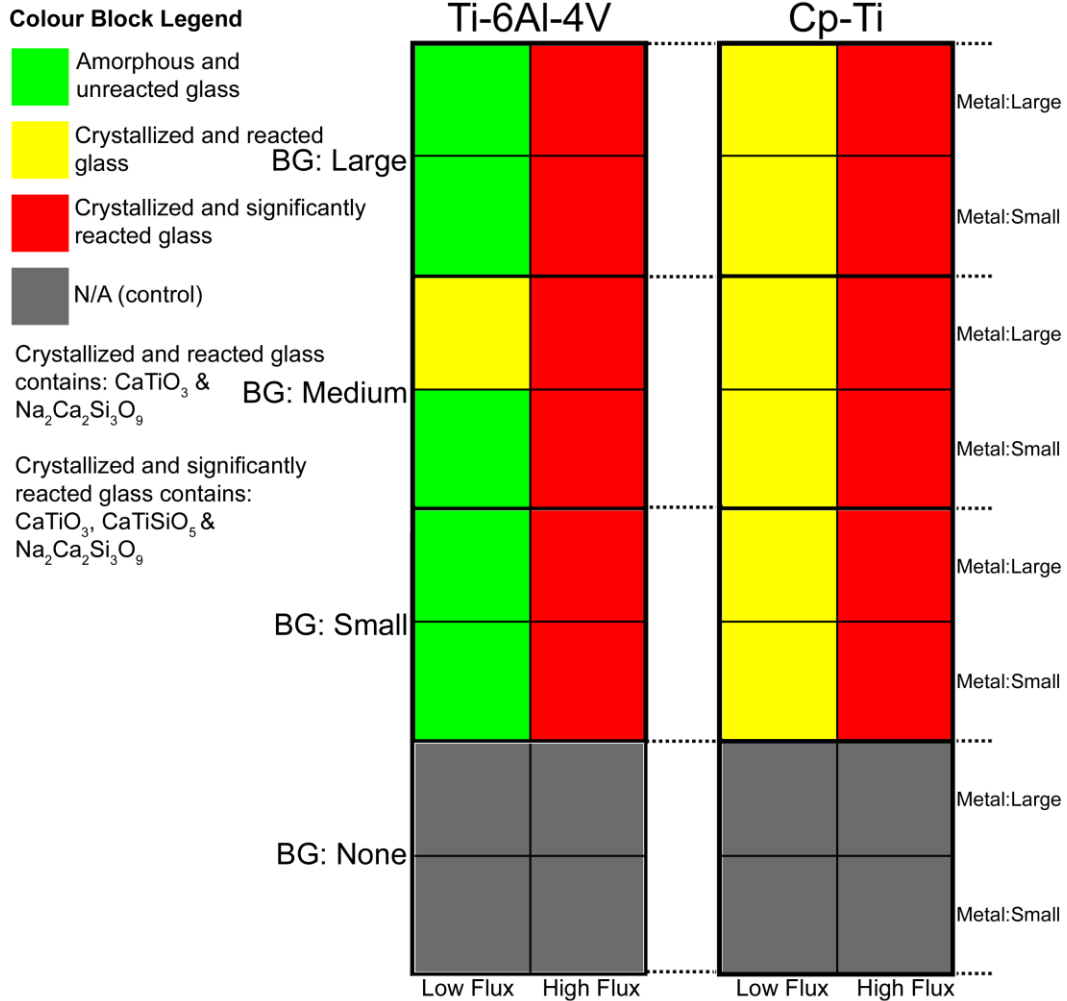


Figure 5-23. Schematic representation of the trends observed in the phase composition as a function of the manipulated variables. Each tile represents an individual combination of powder size, composition, and deposition condition. Legend: Metal - Small refers to $< 45 \mu\text{m}$ powder and Large refers to $45 - 106 \mu\text{m}$ powder; Bioactive Glass: Small refers to $45 - 90 \mu\text{m}$ powder, Medium refers to $90 - 180 \mu\text{m}$ powder, and Large refers to $180 - 250 \mu\text{m}$ powder.

Determination of the precise role of the particle size distribution on the phase composition is difficult without quantitative analysis of the XRD patterns. However, quantitative XRD analysis requires data with precise peak positions and a lack of preferred orientation effects [102]. The patterns presented in Fig. 5-21 and 5-22 were not suitable for such analysis owing to the variation in peak position as well as the preferred orientation effects on peak intensity. Therefore,

only significant changes in signal to noise ratio or the presence of a phase were used as an indication of an effect.

The presence of vanadium-substituted oxide is supported by oxidation studies. As previously discussed, performed on Ti-6Al-4V alloy in an environment containing water vapour; however, there should also be alumina (Al_2O_3) within the scale [95]. Although, no Al_2O_3 was observed in any of the patterns that were examined it is possible that this is evidence of a chemical reaction occurring during deposition.

The presence of combeite indicates that the bioactive glass powder was heated above its crystallization point (650 – 700 °C) [96,97] or its melting point (1200°C) [94] and cooled at an insufficient rate to avoid crystallization for the coatings fabricated under the high flux deposition condition and for the Cp-Ti-based composite coatings. Heating would either have occurred from heating in the flame or from impingement of the flame on the substrate during flame spray deposition. The presence of combeite as a minor or trace phase (based on the very poor signal to noise ratio) for the 90 - 180 μm bioactive glass blended with 45 - 106 μm Ti-6Al-4V alloy coating sprayed under the low flux condition is likely due to a decreased cooling rate from the increased thermal mass of the larger particles. It is likely that the bioactive glass was only partially crystallized due to the very poor signal to noise ratio observed when compared to the Cp-Ti-based coatings as well as the coatings fabricated under the high flux deposition condition. However, it is also possible that the combeite peaks correspond to the

iso-structural compound, $\text{Na}_2\text{CaSi}_2\text{O}_6$, which was found to be the main crystalline phase of 45S5 bioactive glass, formed between 610°C and 800°C by Lefebvre *et al.*[94] and Lin *et al.*[98]. Regardless, the presence of these peaks indicates crystallization of the previously amorphous (see Fig. 5-3) bioactive glass in the case of high flux coatings and Cp-Ti-based composite coatings. The coating produced by spraying a blend of 45 - 106 μm Ti-6Al-4V alloy and 90 - 180 μm bioactive glass powder under the low flux deposition condition is likely only partially crystallized due to comparatively signal to noise ratio observed.

The presence of perovskite peaks for composite coatings sprayed under the high flux deposition condition, the blend of 45 - 106 μm Ti-6Al-4V alloy and 90 - 180 μm bioactive glass powder sprayed under the low flux deposition condition, and in the Cp-Ti-based composite coating patterns, suggest that the bioactive glass may have chemically reacted with the surrounding metallic matrix. Such a reaction can occur in the solid state between calcium oxide (CaO) and TiO_2 or Ti at temperatures in excess of 1300°C [103,104]. However, 45S5 bioactive glass would already be molten at temperatures in excess of 1200°C [94]. The presence of a molten or semi-molten phase would likely accelerate the rate of reaction as it is as it is well known that liquid-liquid and liquid-solid reactions do not have the same kinetic and diffusional barriers as solid-solid reactions [105]. Therefore, it is most likely that the presence of perovskite indicates reaction between the molten/semi-molten bioactive glass and the surrounding titanium matrix. This is additionally supported by the poor signal to noise ratio observed for the peaks

corresponding to TiO_2 in the composite Cp-Ti-based coatings and those sprayed under the high flux deposition condition. The combined presence of combeite and perovskite may indicate that the bioactive glass did not cool rapidly (after leaving the torch and the flame), resulting in reaction with the surrounding matrix and crystallization upon cooling. It is likely that the darker phase (see Fig. 5-8, 5-9, 5-10 and 5-12) between bioactive glass and the surrounding matrix is a reaction phase such as perovskite. The absence of combeite and perovskite for Ti-6Al-4V-based composites, suggests that either the particles attained lower temperatures during flame spray deposition than particles of Cp-Ti, and/or the Ti-6Al-4V alloy or the particles cooled at an accelerated rate that preserved the amorphous nature of the glass. The one notable exception is the presence of both combeite and perovskite as a minor phase, on the basis of the poor signal to noise ratio for the characteristic peaks, (see Fig. 5-22 and 5-23) observed for the coating fabricated from 45 - 106 μm Ti-6Al-4V alloy powder blended with 90 - 180 μm bioactive glass powder with the low flux condition. The presence of both phases may be due to a lower cooling rate from the presence of a larger thermal mass of particles. However, there was no optical evidence (see Fig. 5-7) of the presence of reaction phase in the cross-sectional microstructure.

In the case of the coatings deposited under the high flux condition, the presence of titanite, combeite, and perovskite was noted (see Fig. 5-22 and 5-23). The combined presence of titanite and perovskite and the reduction in the intensity of the peaks corresponding to TiO_2 could suggest phase equilibrium. A study of the

CaO-TiO₂-SiO₂ ternary system by DeVires *et al.* [106] indicated that in predominately TiO₂ systems, the expected equilibrium phases are titanite, TiO₂, and perovskite. Additionally, the phase diagram proposed by DeVires *et al.* [106], and included in Fig. 5-24, suggests that a ternary eutectic between TiO₂-CaTiSiO₅-CaTiO₃ exists at 1365°C. Therefore, the presence of both perovskite and titanite in coatings deposited under the high flux condition suggests that the metallic particles may have formed a scale of TiO₂ in flight, which then reacted with the molten/semi-molten bioactive glass forming rutile, perovskite, and titanite upon cooling at the titanium-bioactive glass interface (see Fig 5-12). The relatively high signal to noise ratio of the corresponding peaks suggests that perovskite and titanite are not minor phases. It is possible that a liquid-liquid reaction occurred, indicating that temperatures reached or exceeded the ternary eutectic of 1365°C during the deposition process. Combeite most likely formed during the cooling process due to slow cooling of the unreacted bioactive glass phase. As previously discussed, an amorphous structure is desired for the bioactive glass. Therefore, coatings in which the bioactive glass is fully (or significantly) crystallized are undesirable candidates for a changing landscape coating.

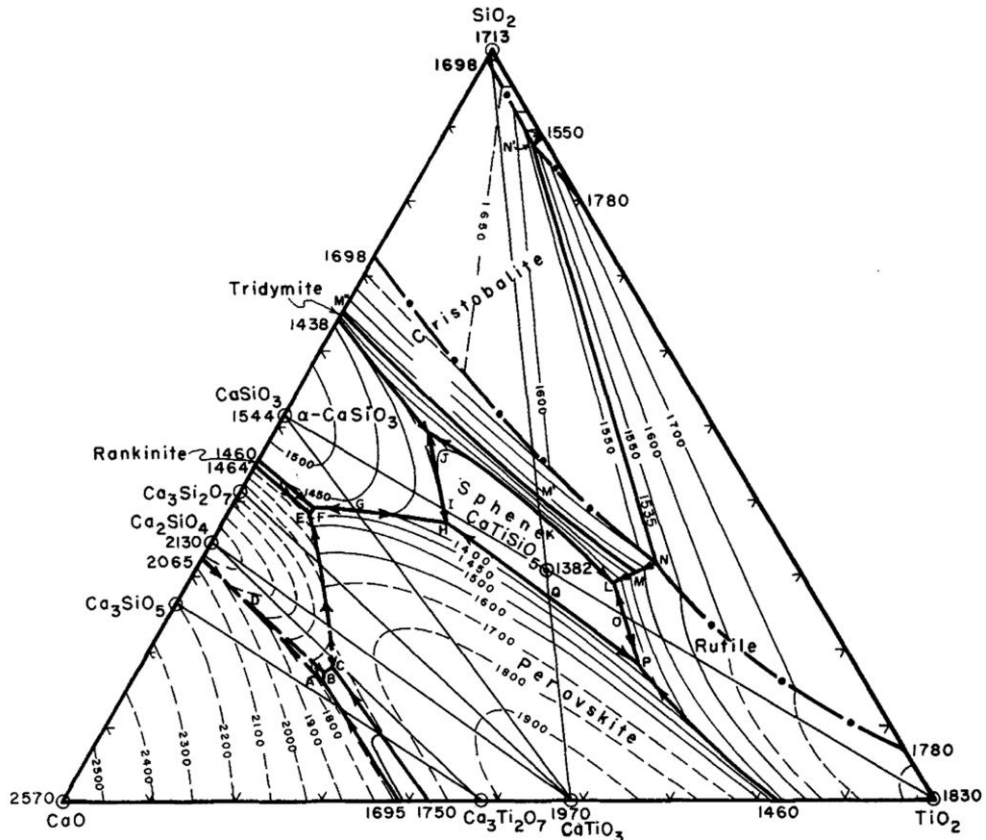


Figure 5-24. Phase diagram of the ternary CaO-TiO₂-SiO₂. Compositions are in weight percent and temperatures are given in °C. Heavy lines are phase boundaries; fine lines are isotherms (dashes in both cases indicate uncertainty); Heavy dash-dot lines indicate boundaries of two-liquid region and letters refer to invariant points. The eutectic of interest corresponds to point P at 1365°C (reprinted and reproduced with permission from John Wiley and Sons Inc.) [103].

5.6. *In Vitro* Bioactivity Assessment

The subset of coatings for *in vitro* bioactivity assessment, shown in Table 3-5, was selected to be representative of all coatings discussed so far. Furthermore, the coatings that are not tested were eliminated based upon microstructure, morphology, phase composition, porosity, or a combination of these characteristics; therefore, all further testing will occur with the subset of coatings shown in Table 3-5. Additionally, the selection was made to best demonstrate the effects of feedstock composition, feedstock particle size distribution, and deposition condition. However, the coatings fabricated under the high flux deposition condition exhibited formation of multiple reaction phases and the crystallization of the bioactive glass which may be undesirable; therefore, only a single composite coating fabricated from each alloy was tested to assess the effects of selecting the high flux deposition condition. Moreover, the control coatings sprayed under the high and low flux conditions were also assessed for *in vitro* bioactivity. The *in vitro* bioactivity was assessed by SBF immersion testing for 0, 3, 7, and 14 days. After immersion, the treated samples were analyzed for the presence of HA with two techniques: SEM with EDX, and FTIR. The results of the SEM with EDX and FTIR analysis on the tested coatings are discussed herein. Additionally, the findings for the Ti-6Al-4V-based composites discussed herein are in agreement with that found by Nelson *et al.*[78], indicating that the coating process is robust and produces consistent microstructures with similar performance regardless of the date of deposition. The findings of the analyses discussed in this section are summarized in a visual form in Fig. 5-25.

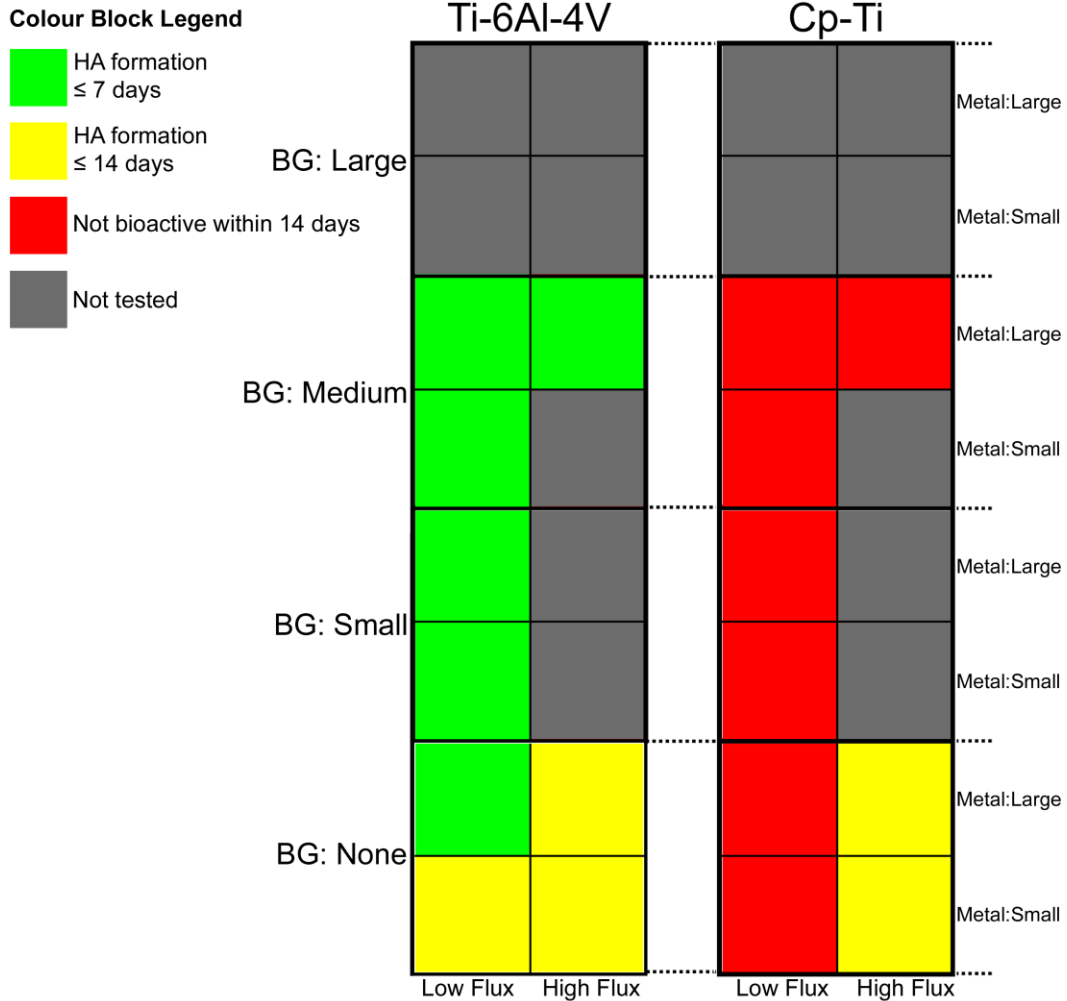


Figure 5-25. Schematic representation of the results of the in vitro bioactivity assessment through SBF immersion testing of the coated substrates. Positive results are indicated with the time interval that HA formation was observed. Each tile represents an individual combination of powder size, composition, and deposition condition. Legend: Metal - Small refers to < 45 μm powder and Large refers to 45 - 106 μm powder; Bioactive Glass: Small refers to 45 - 90 μm powder, Medium refers to 90 - 180 μm powder, and Large refers to 180 - 250 μm powder

5.6.1. Scanning Electron Microscopy (SEM) with Energy

Dispersive X-ray (EDX) Spectroscopy

Representative SEM micrographs, shown in Fig. 5-26a, were acquired in the SE and BSE imaging modes of the top surfaces of the coated titanium substrates that

were treated in SBF. The representative micrographs selected were of a sample that formed a HA mineral layer and a sample that was devoid of HA. EDX was used to determine the overall surface chemistry as well as the calcium to phosphorous (Ca/P) ratio of any layer that formed. However, SEM with EDX analysis is not sufficient to conclusively prove that an observed surface layer is HA; FTIR analysis (section 5.6.2) was used to demonstrate whether or not the observed surface layer, if any, was HA. Additionally, cross-sectional SEM micrographs of the bioactive glass located at or near the top surface of the coating are included in Fig. 5-26b. Common calcium phosphate minerals [2,4,18] and the Ca/P ratio for each mineral are included in Table 5-5. The SEM results are summarized in Table 5-6 as well as the Ca/P ratio of the surface layer observed after 14 days of formation.

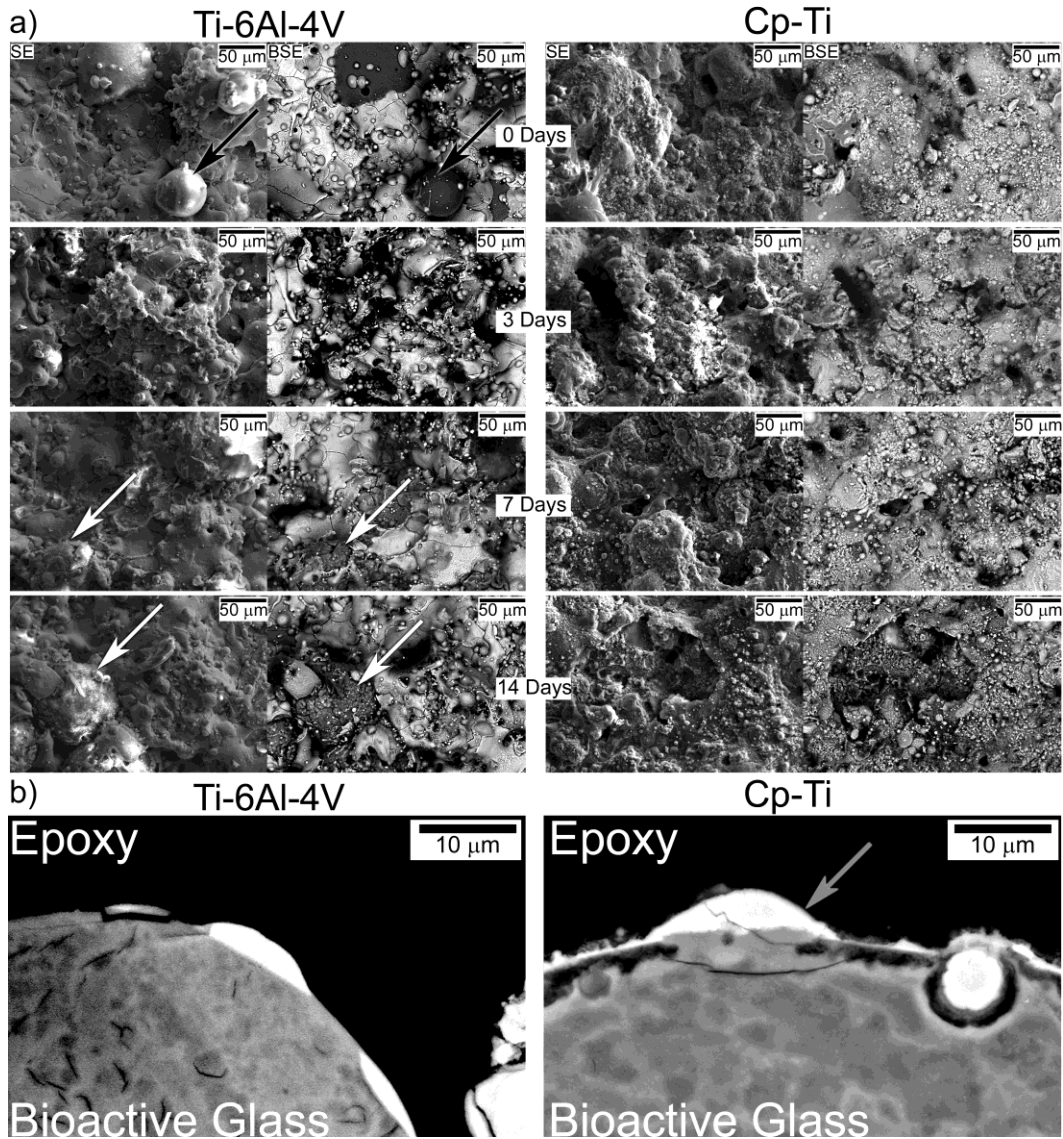


Figure 5-26. a. Representative time-lapse of SEM micrographs taken after SBF immersion in SE and BSE imaging mode of the $< 45 \mu\text{m}$ metallic powder blended with $45 - 90 \mu\text{m}$ bioactive glass coatings. White arrows correspond to hydroxyapatite and black arrows correspond to bioactive glass; b. Representative SEM micrographs of the cross-sectional morphology of the incorporated bioactive glass located at or near the top surface of the coating taken in BSE imaging mode (grey arrow indicates encapsulating layer surrounding bioactive glass particles). Left: $< 45 \mu\text{m}$ Ti-6Al-4V alloy blended with $45 - 90 \mu\text{m}$ bioactive glass; Right: $< 45 \mu\text{m}$ Cp-Ti blended with $45 - 90 \mu\text{m}$ bioactive glass

Table 5-5. Common calcium phosphate minerals and the theoretical Ca/P ratio

Mineral	HA	Bioglass	CaHPO ₄	Ca ₃ (PO ₄) ₂	Ca ₄ P ₂ O ₉
Ca:P Ratio	1.67	5.38	1	1.5	2

Table 5-6. Time of surface layer formation as well as Ca/P ratio, if any, of the observed surface layer as determined by SEM.

Deposition Condition	Metal Powder Size Range [μm]	Bioactive Glass Powder Size Range [μm]	Ti-6Al-4V		Cp-Ti	
			Immersion Time of Surface Layer Formation [days]	Atomic Ca/P Ratio of Surface	Immersion Time of Surface Layer Formation [days]	Atomic Ca/P Ratio of Surface
Low Flux	0 to 45	None	14	1.6	n.a.	n.a.
		45 to 90	7	1.8	n.a.	n.a.
		90 to 180	7	1.6	n.a.	n.a.
	45 to 106	None	7	1.9	n.a.	n.a.
		45 to 90	7	1.8	3	1.7
		90 to 180	7	1.8	3	1.5
High Flux	0 to 45	None	14	1.7	7	1.6
	45 to 106	None	14	1.8	14	1.5
		90 to 180	7	1.9	7	1.7

The control coatings showed very little change in terms of morphology until the surface layer developed. A surface layer with a morphology (see Fig. 5-27 left images) and Ca/P ratio (1.6 to 1.8) was formed for the Ti-6Al-4V-based control coatings that suggest the identity of the surface layer is HA [32,34,48]. However, the low flux coating composed of 45 - 106 μm Ti-6Al-4V alloy powder had a Ca/P ratio (1.9) that was higher than would be expected for HA. The Cp-Ti-based control coatings deposited under the high flux deposition condition also showed evidence of a surface layer. However, the Ca/P ratio observed is 1.5 to 1.6, which is on the lower end of the 1.6 to 1.8 [32,34,48] expected for HA and the morphology is inconsistent with that which is observed for the Ti-6Al-4V-based control coatings (see Fig. 5-27). However, the surface layer may still be HA if

there is some degree of residual contamination from the solution. Further investigation of the IR analysis in Section 5.6.2 is necessary.

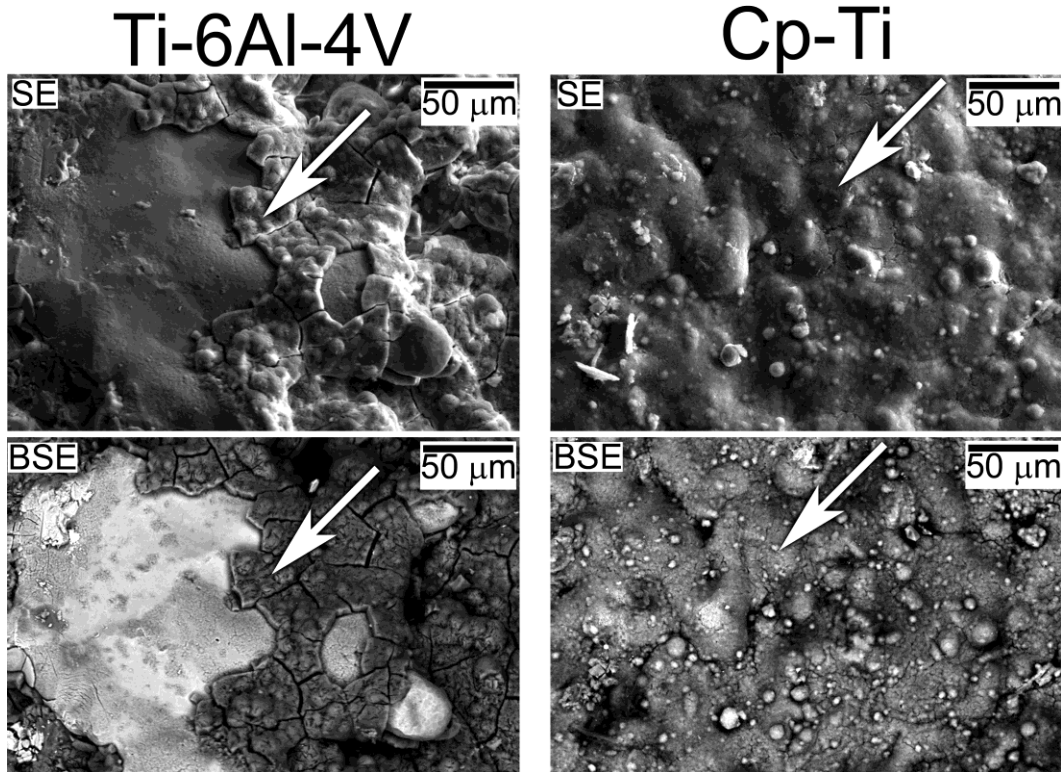


Figure 5-27. Representative SEM micrographs of observed mineral layer formation taken after SBF immersion in SE and BSE imaging mode of the control coatings sprayed under the high flux deposition condition. The white arrows correspond to the surface layer.

The Ti-6Al-4V-based composite coatings demonstrated the formation of a mineral layer that was localized on and around the bioactive glass as early as 7 days of immersion in SBF (see Table 5-3 and Fig. 5-26a left images). The morphology (see Fig. 5-26a left images) and Ca/P ratio (1.6 to 1.8 depending upon the specific coating) suggest that this layer is HA [32,34,48]. However, it should be noted that the Ca/P ratio exceeds that of the predicted 1.67 for several of the coatings. The higher Ca/P ratio could be due to signal from the underlying bioactive glass which has a calculated Ca/P ratio of 5.38. The low flux < 45 μm

Cp-Ti-based composite coatings showed no change in the testing timeframe. Furthermore, the surface is homogenous in composition with no exposed bioactive glass (see Fig. 5-26a right images and Fig. 2-26b). In contrast, the bioactive glass particles are clearly visible in the micrographs of the Ti-6Al-4V-based composite coatings (see Fig. 5-26a left images and Fig. 5-26b). Cross-sectional observation of the coating microstructure indicated that the bioactive glass may not be visible (inaccessible to fluid), in the case of the Cp-Ti-based composite coating, due to encapsulation of the bioactive glass particles by titanium and/or a titanium-bioactive glass reaction phase (see Fig. 5-26b). A surface layer is observed as early as 3 days for the 45 - 106 μm Cp-Ti-based composite coatings with morphology similar to Fig. 5-27 right images [32,34,48]. However, the Ca/P ratio of the observed surface layer for the coating containing 45 - 106 μm Cp-Ti powder and 45 - 90 μm bioactive glass powder is 1.5, which is lower than the 1.67 expected for HA. The identity of the surface layer is presently unknown however it may correspond to an amorphous calcium phosphate compound with an approximate composition of $\text{Ca}_3(\text{PO}_4)_2 \cdot 3\text{H}_2\text{O}$ [18]. Finally, the 45 - 106 μm titanium alloy composites sprayed under the high flux deposition condition show formation of a surface layer as early as 7 days around features that are identified as a glassy phase. The layer formed has a morphology (similar to Fig. 5-26 left images) and Ca/P ratio (1.6 to 1.8) that suggests it is HA [32,34,48]. The formation of a mineral layer on the Ti-6Al-4V-based control coatings and the high flux control coatings could be due to the potentially greater presence of the rutile and anatase phase of TiO_2 (see Fig. 5-19 and 5-20). The mechanism for this

formation was detailed in a review by Kokubo *et al.* [4]. The lack of formation of HA for the < 45 μm Cp-Ti-based composites may be due to the lack of surface accessible bioactive glass (see Fig. 5-26 right images); while the layer forming in the case of the remaining Cp-Ti-based composite coatings does not appear to be HA.

5.6.2. Fourier Transform Infrared (FTIR) Spectroscopy

The findings of the FTIR analysis are summarized in Table 5-7 along with the time of formation for HA. The collected spectra for the control coatings is included in Fig. 5-28 and 5-29; the spectra collected from the composite coatings are included in Fig. 5-30 and Fig. 5-31. The spectra shown in Fig. 5-28 and 5-29 show that the surface layer observed, if any, for the Ti-6Al-4V alloy control coatings sprayed under both the high and low flux conditions, and the Cp-Ti control coatings sprayed under the high flux condition is HA. However, the control coating produced by spraying 45 - 106 μm Ti-6Al-4V alloy under the low flux condition show evidence of a calcium phosphate compound but the lack of characteristic peak splitting between 600 and 550 cm^{-1} does not support that the layer is HA. The spectra shown in Fig. 5-30 support that the observed surface layers formed for the Ti-6Al-4V-based composite coatings that was formed on the treated substrates was HA. The spectra shown in Fig. 5-31 suggest that the observed surface layers formed for 45 - 106 μm Cp-Ti-based composite coatings is not HA. The peaks that represented the presence of titanium oxides (TiO_2) were located between 400 to 800 cm^{-1} , at approximately 825 cm^{-1} , 1000 to 1200 cm^{-1} , and at

approximately 1725 cm^{-1} [33,107-109]. The FTIR spectra showed little change with increasing immersion time for both the Cp-Ti and the Cp-Ti-based composite coatings. The formation of a surface compound is shown in the $< 45\text{ }\mu\text{m}$ Ti-6Al-4V alloy control coatings as early as 14 days and the Ti-6Al-4V-based composite coatings after 7 days of immersion in SBF. The identity of the surface layer HA is supported by the presence of bands attributed to $(\text{CO}_3)^{-2}$ and $(\text{PO}_4)^{-3}$. Characteristic peaks for inorganic carbonate are observed at approximately 1550 cm^{-1} , 1457 cm^{-1} , and 880 cm^{-1} [33,34,38,39,97,107]. The presence of these peaks suggest the the surface layer may be carbonated. However, these peaks can also correspond to residual sodium bicarbonate from the SBF solution and/or adsorbed carbon dioxide. These peaks were attributed to residual sodium biocarbonate and/or adsorbed carbon dioxide for samples that did not form a surface layer.

Table 5-7. Summary of surface layer identification by FTIR of the coated titanium substrates after SBF immersion testing.

Deposition Condition	Metal Powder Size Range [μm]	Bioactive Glass Size Range [μm]	Time to HA formation [Days]	
			Ti-6Al-4V	Cp-Ti
Low Flux	0 - 45	0	14	N/A
		45 - 90	7	N/A
		90 - 180	7	N/A
	45 - 106	0	7	N/A
		45 - 90	7	N/A
		90 - 180	7	N/A
High Flux	0 - 45	0	14	14
	45 - 106	0	14	14
		90 - 180	7	N/A

Low Flux Condition

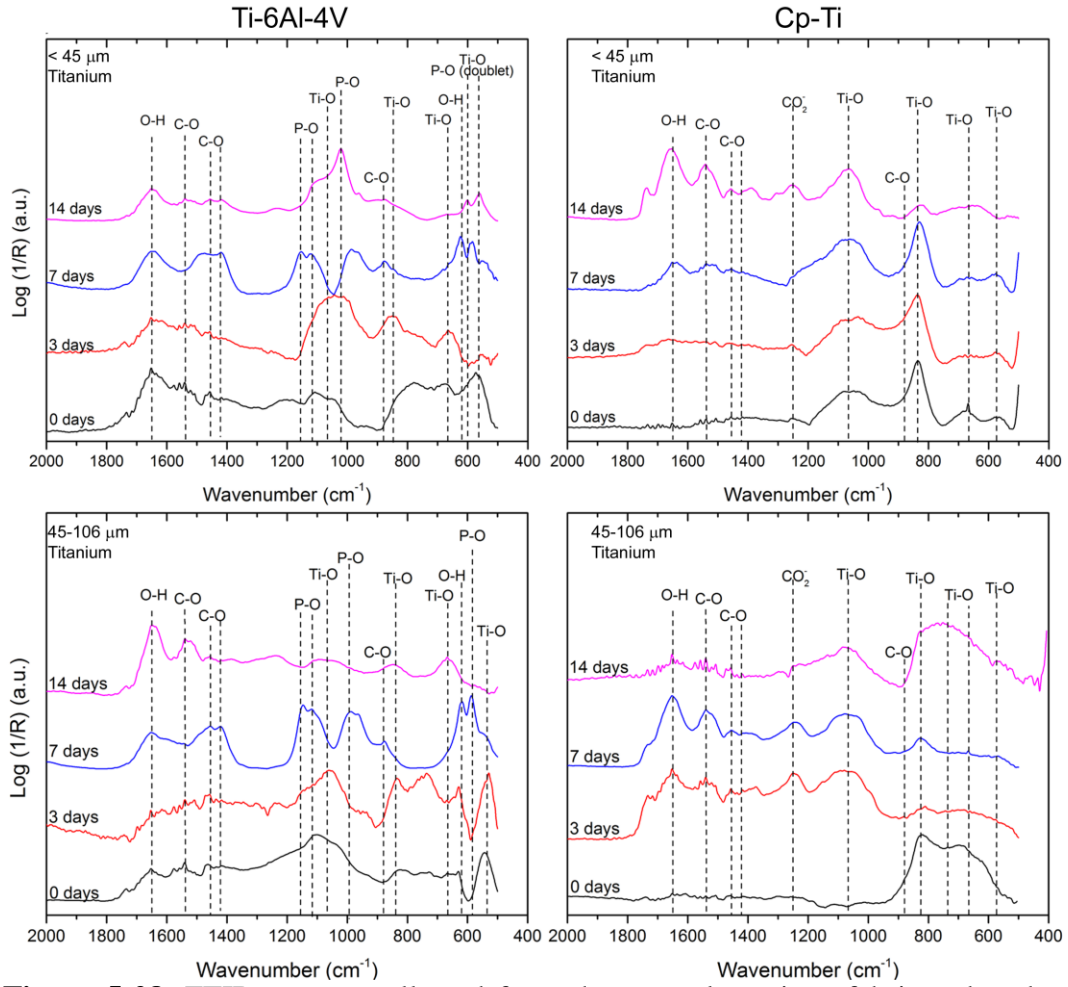


Figure 5-28. FTIR spectra collected from the control coatings fabricated under the high flux deposition condition after SBF immersion.

High Flux Condition

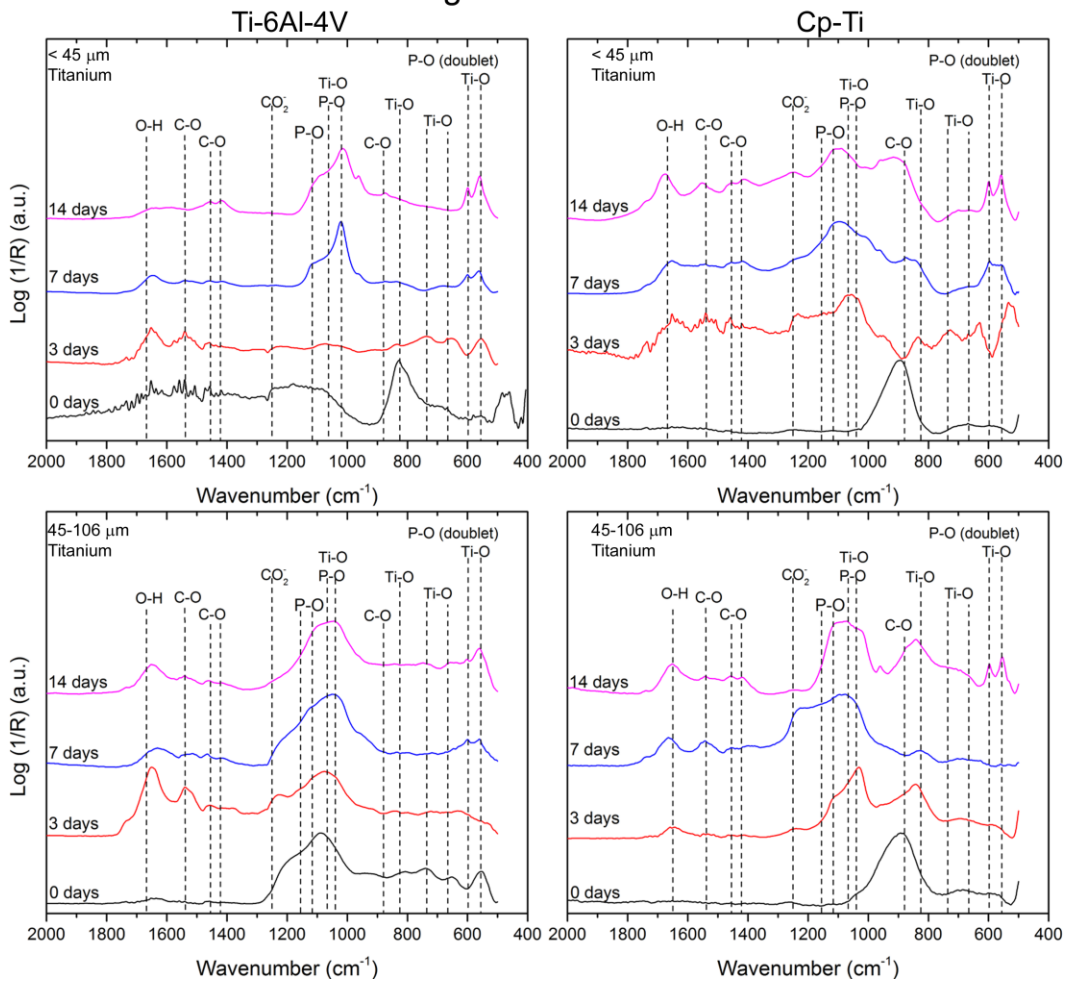


Figure 5-29. FTIR spectra collected from the control coatings fabricated under the high flux deposition condition after SBF immersion.

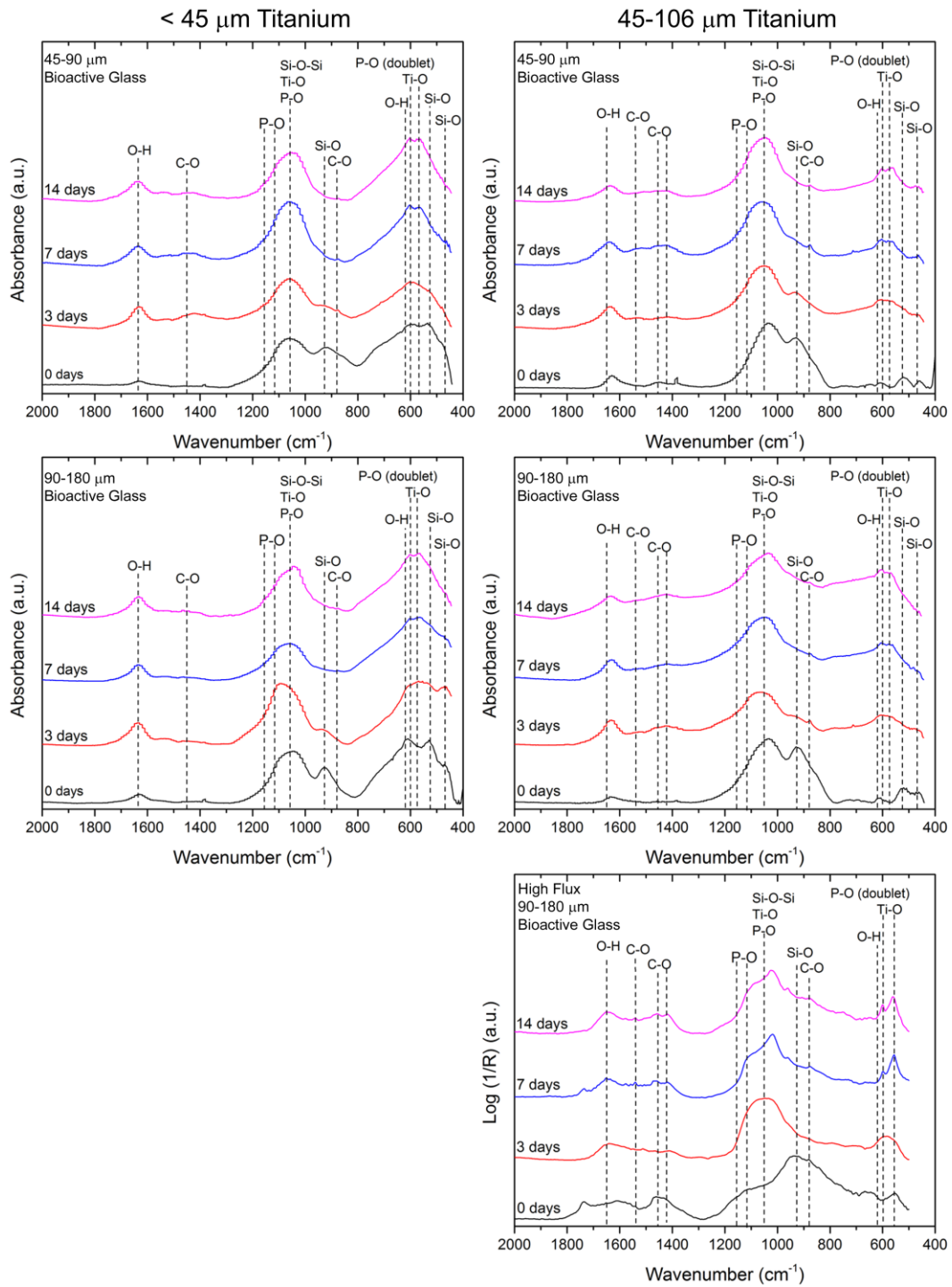


Figure 5-30. FTIR spectra collected from the Ti-6Al-4V-based composite coatings after SBF immersion.

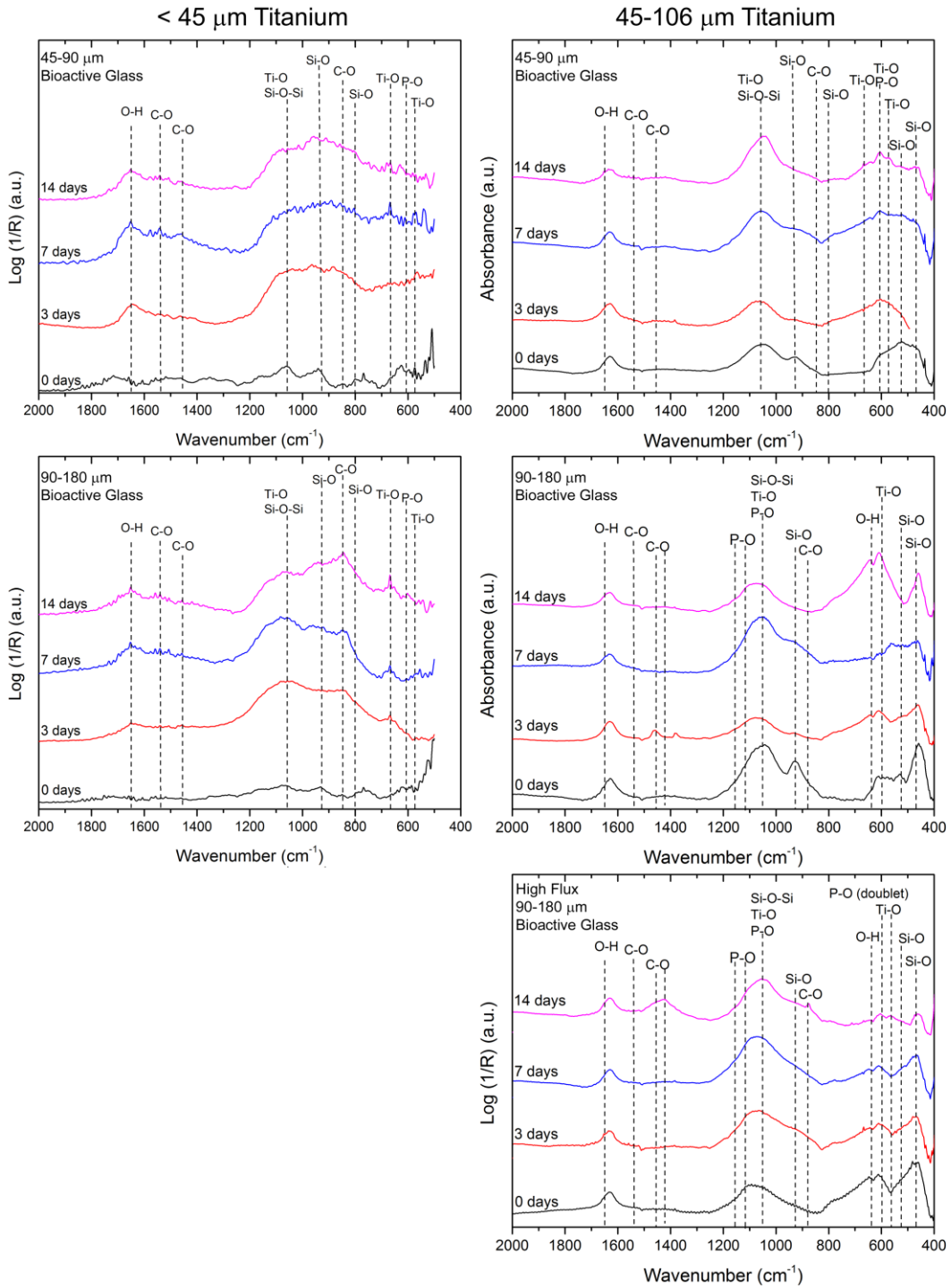


Figure 5-31. FTIR spectra collected from the Cp-Ti-based composite coatings after SBF immersion.

The characteristic peaks for $(\text{PO}_4)^{3-}$ ($n_3 \sim 1050 \text{ cm}^{-1}$, $n_1 \sim 960 \text{ cm}^{-1}$, $n_4 \sim 600 \text{ cm}^{-1}$ and 560 cm^{-1}) were observed for the Ti-6Al-4V-based composite coatings [27,34,38-

40,97,107,110]. The peak splitting observed in the $600 - 550 \text{ cm}^{-1}$ band is characteristic of HA. Peaks for bioactive glass and absorbed water were also observed and were assigned, as described by other investigators [27,33,34,38-40,94,97,107-111]. The peaks indicating surface mineralization appeared after 7 days of immersion for the Ti-6Al-4V-based composite coatings and as early as 14 days for $< 45 \text{ }\mu\text{m}$ Ti-6Al-4V alloy control coatings. The characteristic peaks for HA were also noted in the control coatings of Ti-6Al-4V alloy and Cp-Ti deposited under the high flux deposition condition after 14 days of immersion. The presence of the characteristic peaks indicate that HA is the surface mineral that was formed. The absence of the characteristic peaks for $(\text{PO}_4)^{-3}$ in the Cp-Ti control, $45 - 106 \text{ }\mu\text{m}$ Ti-6Al-4V alloy control sprayed under the low flux condition, and Cp-Ti composite coatings supports that no such layer was formed suggesting that the layer observed under the SEM is another compound. The identity of the surface layer is presently unknown however it may correspond to an amorphous calcium phosphate compound with an approximate composition of $\text{Ca}_3(\text{PO}_4)_2 \cdot 3\text{H}_2\text{O}$ [18]. Final determination of the identity of the unknown surface quantity requires further analysis but the FTIR spectras presented demonstrate that Cp-Ti-based composite coatings do not form HA *in vitro*.

5.6.3. Inductively Coupled Plasma Mass Spectroscopy (ICP-MS)

The spent SBF fluid from the composite coatings was analyzed with ICP-MS to assess if metallic ions leached into the physiological SBF solution. The solution was collected after each 3-day replacement cycle of the SBF immersion test for

composite coatings. The results presented in Fig. 5-32 are grouped by the deposition condition of the coatings as well as the metallic powder size distribution. An average baseline was established by measuring the concentration of Ti, V, and Al ions in the feedstock solution. Six samples of fluid ($n = 6$) were used to establish the average baseline and the error presented in Fig. 5-32 is the standard error. The baseline concentrations in the SBF were 2.0 ± 0.1 , 0.52 ± 0.04 , and 1.22 ± 0.04 $\mu\text{mol/L}$ of Ti, Al, and V respectively. Additionally, the concentration of Ti, V, and Al ions in the water used to prepare the SBF was measured and the concentration of Ti ions was below the detection limit of the instrument; Al and V concentrations were on the order of 0.3 $\mu\text{mol/L}$. The metallic ion release behaviour as a function of immersion time was established by this analysis. In the first cycle of immersion (see Fig. 5-32), a substantial increase was noted in the concentration of V ions for all Ti-6Al-4V-based coating samples. Each subsequent cycle of immersion resulted in a reduced concentration of V ions. This behaviour suggests that the release rate of vanadium decreases with increasing immersion time. The Ti and Al ions show no change until the second 3-day immersion cycle, after which the concentration of Ti and Al increased significantly and begin to decrease in subsequent cycles. For the Cp-Ti-based composites the change in the V concentration with increasing immersion time was negligible, as would be expected; however, the Al concentration increased from the baseline after the first cycle of immersion and maintained an elevated concentration in subsequent cycles. The increased concentration of Al ions for Cp-Ti-based composites was likely due to either contamination of the solution or

leaching of aluminum from the Al_2O_3 particles that may have become embedded during gritblasting of the substrate. Comparing the magnitude of the ionic concentration is difficult without normalizing the data by an appropriate parameter such as coating surface area. But, the coating surface area was not measured. Therefore, normalization and comparison of the magnitude of the ionic concentrations is left to future work. The presence of the increased concentration of V ions is of particular concern. Studies reviewed by Steinemann [1] have shown that the leeching of vanadium ions can result in a foreign body response and rejection of the implant. However, a foreign body response will not occur unless the concentration of vanadium ions released surpasses the concentration that causes local cell death or chronic toxicity. Therefore, further study is necessary to determine whether or not the concentration observed is sufficient to cause a detrimental response.

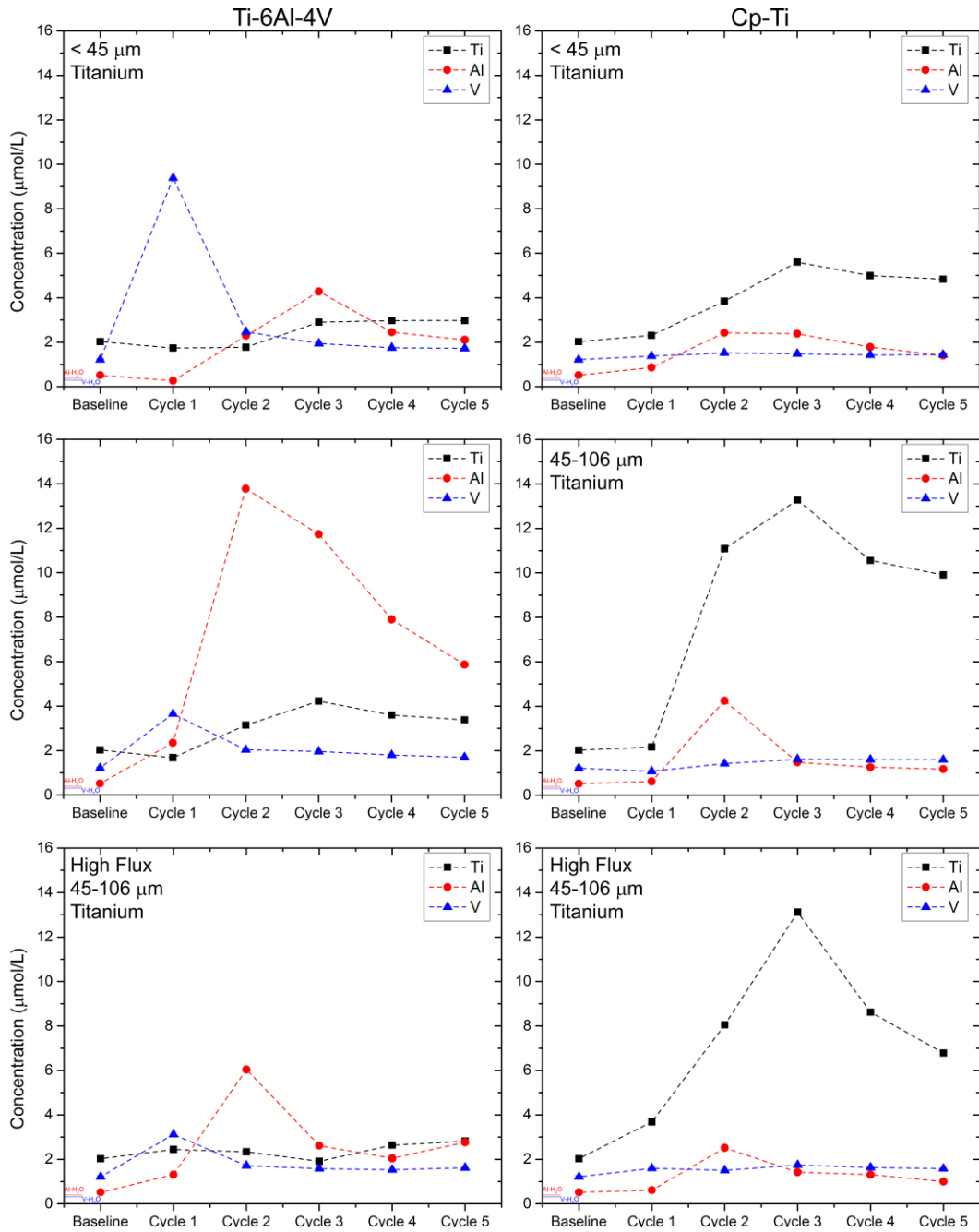


Figure 5-32. Aqueous concentrations of Ti, Al, and V in spent SBF solution collected after each 3 day cycle and measured by ICP-MS. Standard error was $\pm 0.1 \mu\text{mol/L}$ (Ti), and $\pm 0.04 \mu\text{mol/L}$ (Al, V).

5.6.4. Summary of *in vitro* Bioactivity Assessment

The trends discussed previously and summarized herein were also included in a visual schematic (see Fig. 5-25). The coatings tested for the formation of HA after immersion in SBF as an indicator for *in vitro* bioactivity demonstrated that HA forms within 7 days of immersion of Ti-6Al-4V-based composite coatings regardless of deposition condition or particle size distribution (see Fig. 5-26 and 5-30). While, formation of a surface layer is observed for some, but not all, Cp-Ti-based composite coatings the evidence collected supports that such a layer was not HA (see Table 5-5 and Fig. 5-31). The control coatings of Ti-6Al-4V alloy as well as the Cp-Ti control coatings fabricated under the high flux condition demonstrated the formation of HA after 14 days (see Fig. 5-27 to 5-29). The control fabricated from $< 45 \mu\text{m}$ Ti-6Al-4V alloy powder under the low flux condition demonstrated the formation of HA after 14 days (see Fig. 5-28); while, the control coating fabricated from 45 - 106 μm Ti-6Al-4V alloy powder under the low flux condition demonstrated the formation of HA after 7 days (see Fig. 5-28). The formation of HA on the control coatings may be due to the bioactive response to the anatase and/or rutile phase. However, these control coatings are not capable of actively promoting the differentiation of osteoblasts owing to the absence of a class A bioactive compound that can provide the release of ions at the critical concentrations and release rates to induce the differentiation of osteoblasts [2,3]; therefore, the control coatings are an inferior choice to the composite coatings as the composite coatings contain bioactive glass which is a

class A bioactive compound. Additionally, the lack of formation of HA for Cp-Ti-based composite coatings indicates that Cp-Ti-based composite coatings may be unsuitable for use in the intended application.

Therefore, the lack of bioactivity in the case of Cp-Ti-based composite coatings suggests that the Ti-6Al-4V-based composite coatings are the most promising. The inclusion of bioactive glass accelerates that rate of HA formation for Ti-6Al-4V-based composite coatings and may yield an osteopductive response from the incorporation of the surface-accessible (see Fig. 5-26) amorphous (see Fig. 5-3 and 5-21) bioactive glass. However, the release of potentially toxic vanadium ions (see Fig. 5-32) could be detrimental to the clinical success of the coating if the concentration is sufficient to result in a detrimental response [1].

5.7. Mechanical Properties

The tensile mechanical response was characterized with tensile adhesion testing for the same subset of coatings for which the *in vitro* bioactive response was assessed (see Table 3-5). Additionally, the control coatings sprayed under the low and high flux conditions were characterized. Tensile adhesion testing samples were tested according to ASTM Standard C633 [74] and the fractured surfaces were imaged with macrophotography. The mechanical response of these coatings and the fracture surfaces are discussed herein.

5.7.1. Adhesion Testing and Fractography

The mechanical properties of the coatings were assessed via the ASTM Standard C633 tensile adhesion test [74]. The bonded assemblies (see Fig. 3-2 and Appendix: Drawings) were pulled in a uniaxial mechanical tester until failure with a constant crosshead speed of 0.84 mm/min. The trends discussed herein are summarized in a visual schematic in Fig. 5-33. The failed samples were imaged through macrophotography and the fracture mode was determined from the fractographs. In this test, the coatings could have failed via several modes: adhesive failure between the coating and substrate, cohesive failure within the coating, adhesive failure between the coating and the epoxy, or a mixed mode (combination of the aforementioned modes). The bond strength of the epoxy used to bond the coatings and the fixtures was determined to be 22 ± 2 MPa ($n = 5$). The average mechanical strength and porosity were both plotted as a function of bioactive glass powder size, as shown in Fig. 5-34, to ascertain any correlations

between bioactive glass size, metallic powder size, spray condition, porosity, and mechanical response. The error bars in Fig. 5-34 correspond to the standard error ($n = 5$). A schematic representation of the possible failure modes which assigns a number to each failure mode is included in Fig. 5-35. Representative fractographs are included in Fig. 5-36 to 5-38, and the failure mode numbers (see Fig. 5-35) for each sample is provided. However, an adhesive failure between the substrate and coating was not observed for any of the test samples; close examination of the substrate-coating interface (see Fig. 5-36 for a representative micrograph) reveals a continuous interface which suggests that metallurgical bonding is attained between the coating and the substrate.

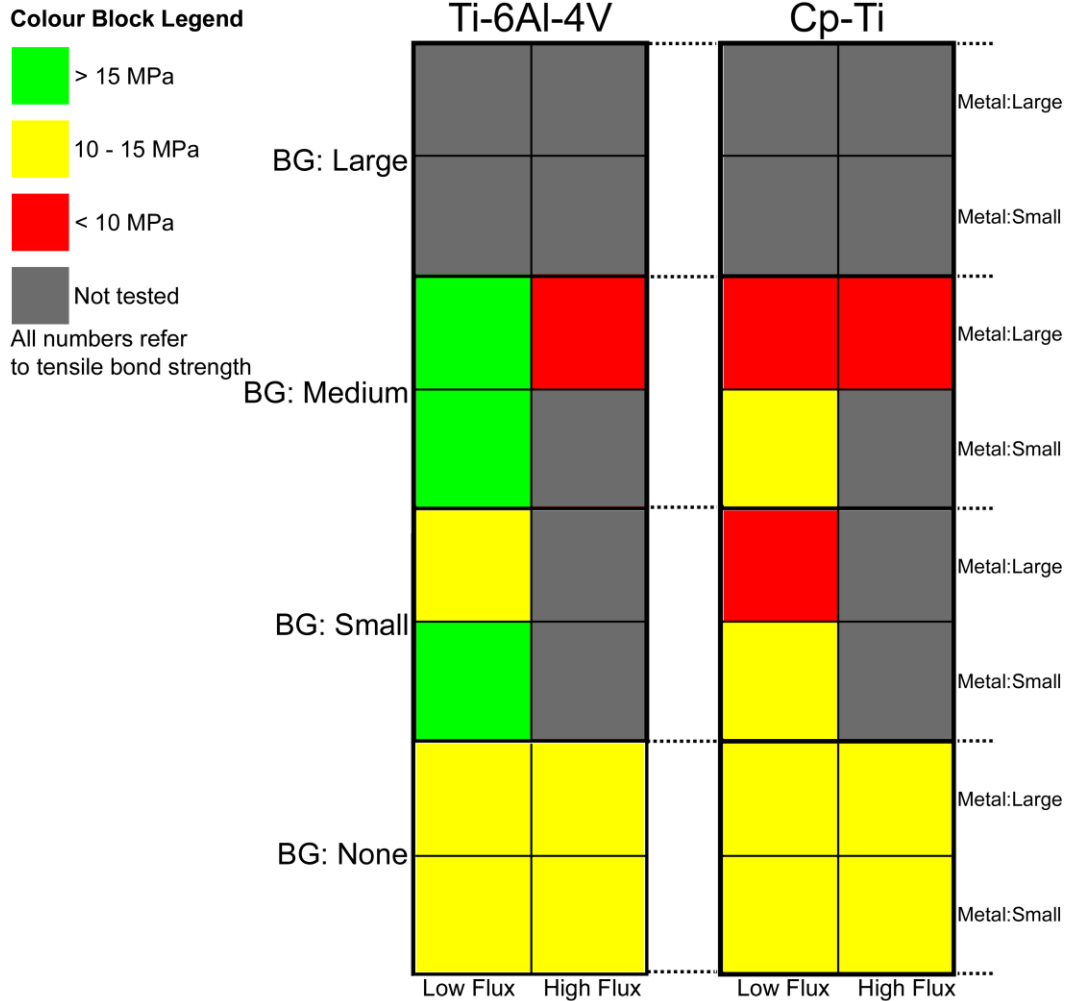


Figure 5-33. Schematic representation of the trends observed in the mechanical bond strengths of the coatings. Each tile represents an individual combination of powder size, composition, and deposition condition. Legend: Metal - Small refers to < 45 μm powder and Large refers to 45 - 106 μm powder; Bioactive Glass: Small refers to 45 - 90 μm powder, Medium refers to 90 - 180 μm powder, and Large refers to 180 - 250 μm powder.

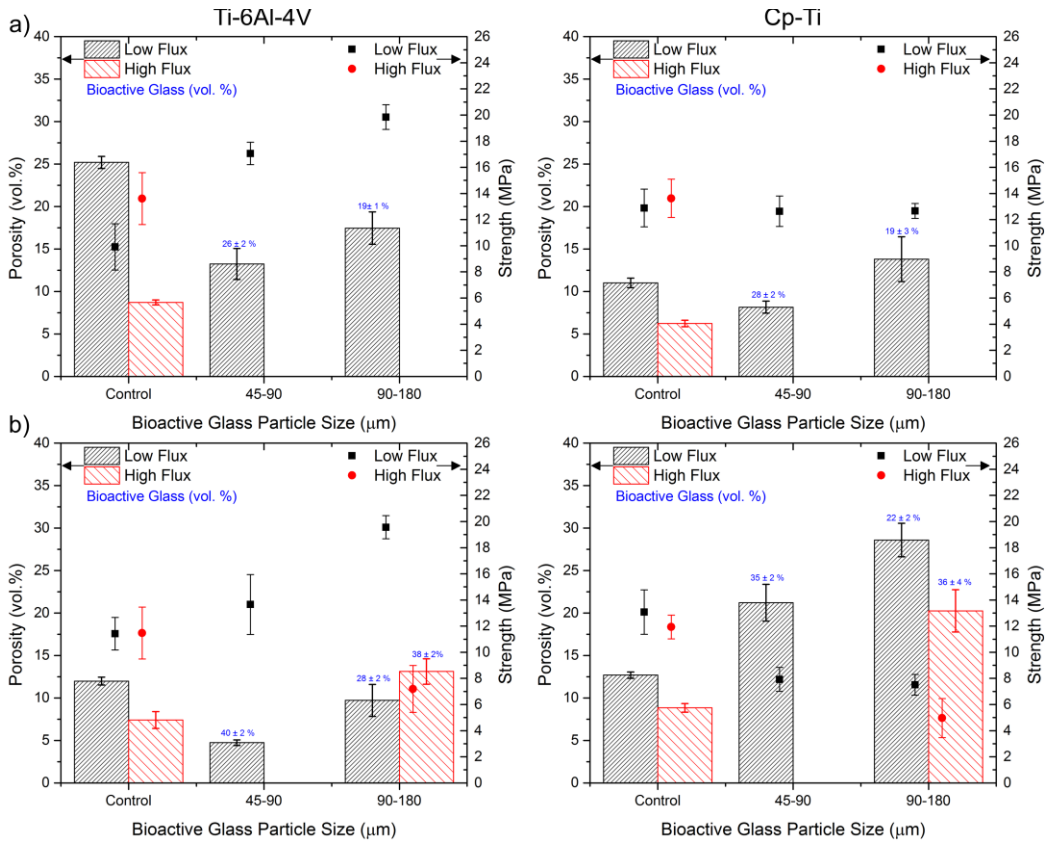


Figure 5-34. Composite plot of porosity and mechanical stress at coating fracture as a function of feedstock bioactive glass particle size distribution: a. coatings based upon < 45 μm metallic powder; b. coatings based upon 45 - 106 μm metallic powder.

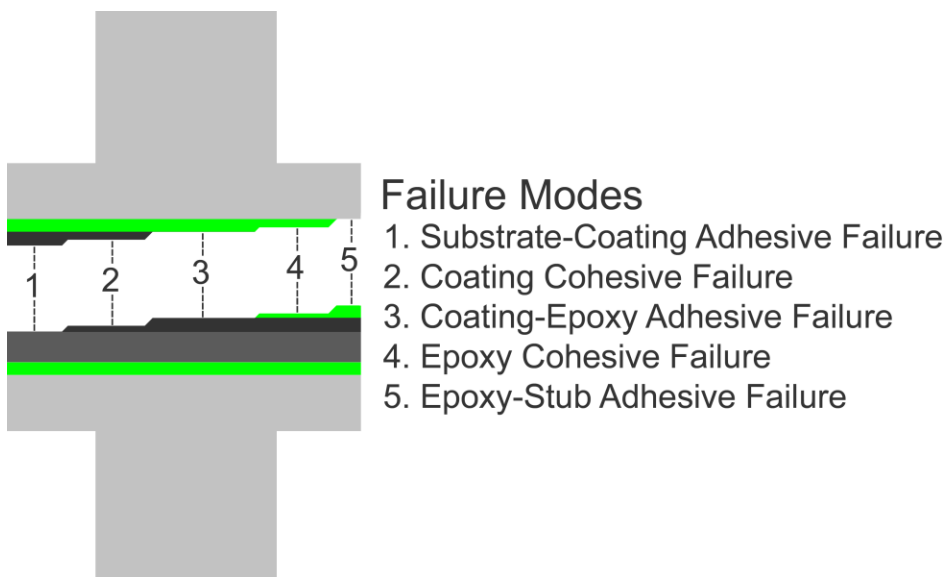


Figure 5-35. Schematic representation of potential failure modes in cross-section from ASTM Standard C633 tensile adhesion testing.



Figure 5-36. Representative fractographs of failed control coatings after ASTM Standard C633 tensile adhesion testing taken by macrophotography. Failure mode type legend: 1. Coating-substrate adhesive failure, 2. Coating cohesive failure, 3. Coating-epoxy adhesive failure, 4. Epoxy cohesive failure, and 5. Epoxy-stub adhesive failure.

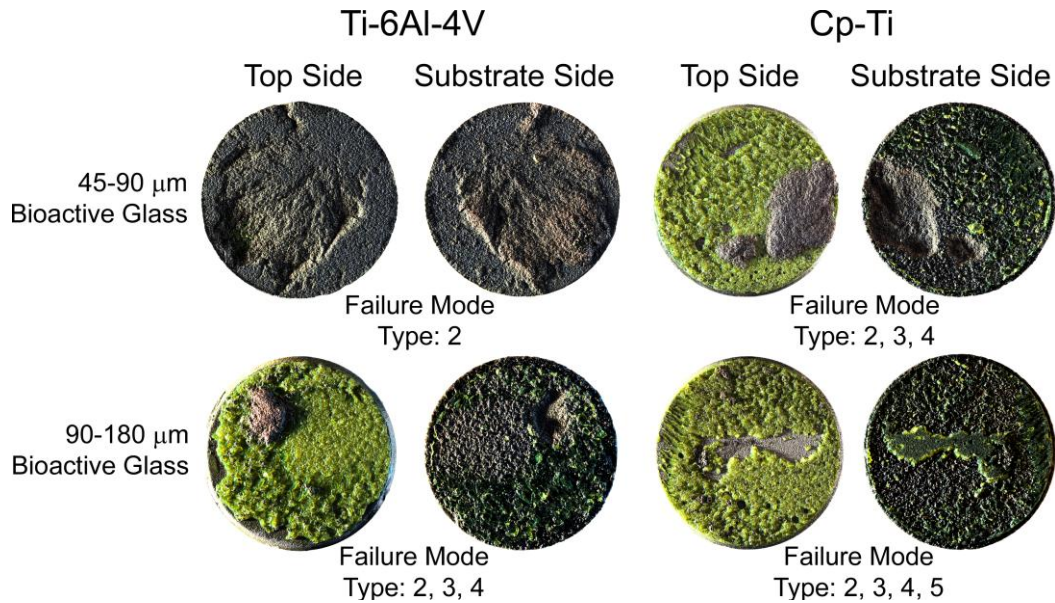


Figure 5-37. Representative fractographs of failed composite coatings fabricated from $< 45 \mu\text{m}$ metallic powder after ASTM Standard C633 tensile adhesion testing taken by macrophotography. Failure mode type legend: 1. Coating-substrate adhesive failure, 2. Coating cohesive failure, 3. Coating-epoxy adhesive failure, 4. Epoxy cohesive failure, and 5. Epoxy-stub adhesive failure.

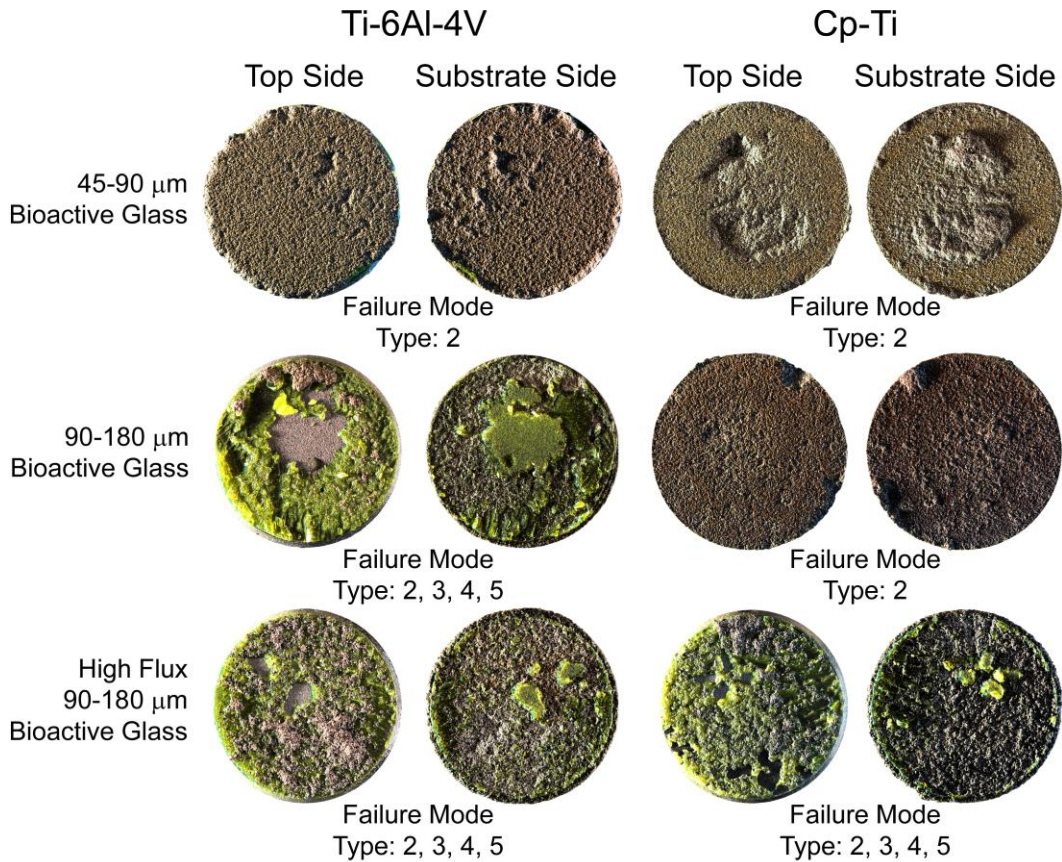


Figure 5-38. Representative fractographs of failed composite coatings tested fabricated from 45 - 106 μm metallic powder after ASTM Standard C633 tensile adhesion testing taken by macrophotography Failure mode type legend: 1. Coating-substrate adhesive failure, 2. Coating cohesive failure, 3. Coating-epoxy adhesive failure, 4. Epoxy cohesive failure, and 5. Epoxy-stub adhesive failure.

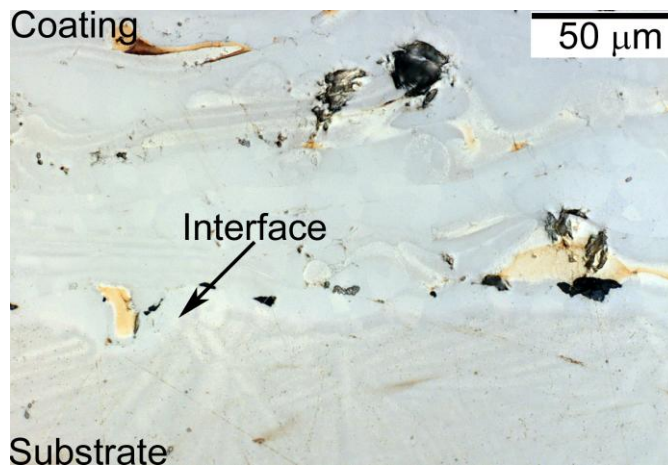


Figure 5-39. Representative optical micrograph of the substrate-coating interface in cross-section demonstrating a continuous interface that suggests metallurgical bonding has occurred. Image was taken from the 45 - 106 μm Cp-Ti-based control coating sprayed under the high flux deposition condition

It is immediately evident upon comparison of the control coatings and composite coatings (see Fig. 5-34) that a simple relationship does not exist between adhesion strength and porosity. The mechanical strength of the control coatings showed no statistically significant differences based on choice of alloy, deposition condition, or metallic powder size (see Table 5-8). The significance was assessed with a two-sample T -test (see Eqn. 3-5 and 3-6) and an F -test (see Eqn. 3-4). It is likely that a significant decrease in porosity would contribute to an increase in strength. Additionally, there was statistically significant difference in thickness observed ($n = 20$) between control coatings (see Table 5-8). The error values provided in Table 5-8 are the 95% CI calculated according to Eqn. 3-3. However, there was no statistically significant difference in mechanical bond strength. It would be expected that a correlation would exist as Hadad *et al.* [71] found, for dense monolithic coatings, that an increase in coating thickness would reduce the mechanical bond strength of the coating. Therefore, there are likely other factors altering the adhesion/cohesion strength of the coatings as a statistically significant change in porosity or coating thickness does not yield a statistically significant change in strength for the control coatings.

Table 5-8. Thickness and stress at failure of the thermally sprayed control coatings according to ASTM Standard C633 tensile adhesion testing.

Condition	Metallic Powder Size [μm]	Ti-6Al-4V		Cp-Ti	
		Thickness [μm] (n = 20)	Failure Strength [MPa] (n = 5)	Thickness [μm] (n = 20)	Failure Strength [MPa] (n = 5)
Low Flux	0 - 45	500 ± 11	10 ± 5	1017 ± 14	13 ± 4
	45 - 106	453 ± 10	11 ± 3	1061 ± 22	13 ± 5
High Flux	0 - 45	531 ± 10	14 ± 6	1043 ± 12	14 ± 4
	45 - 106	82 ± 16	12 ± 6	1111 ± 13	12 ± 3

First trends observed for the low flux composite coatings will be discussed. The incorporation of bioactive glass has a more complex effect on the mechanical strength of the coatings. The tensile stress measured at failure of the coating is included in Table 5-9 with a 95% confidence interval. A noticeable and statistically significant increase in mechanical strength is observed with the incorporation of bioactive glass for Ti-6Al-4V-based composite coatings (see Fig. 5-34, Table 5-8 and 5-9). Further, the strength of the Ti-6Al-4V-based composites is increased to 20 ± 3 MPa when 90 - 180 μm bioactive glass is used in the powder blend, from 10 ± 2 MPa and 11 ± 4 MPa for the < 45 μm and 45 - 106 μm Ti-6Al-4V alloy control coatings. Addition of bioactive glass has no statistical effect on the adhesion strength of < 45 μm Cp-Ti-based control coatings at 13 MPa. Increasing the bioactive particle size lead to an increase in strength for Ti-6Al-4V-based coatings but this increase was not of statistical significance; however, the calculated value of T was very close to the tabulated critical value. Increasing the bioactive glass particle size has no effect for < 45 μm Cp-Ti-based coatings while a decrease to 8 ± 2 MPa is observed for 45 - 106 μm Cp-Ti-based coatings (see Fig. 5-30 and Table 5-9). However, this decrease is not of statistical

significance. These trends suggest that the bioactive glass may be reinforcing the coating in the case of Ti-6Al-4V-based coating. In contrast, the inclusion of bioactive glass appears to have a negligible effect on the bond strength of < 45 μm Cp-Ti-based coatings and a negative effect on the bond strength of 45 - 106 μm Cp-Ti-based coatings.

Table 5-9. Stress at failure of the thermally sprayed composite coatings according to ASTM Standard C633 tensile adhesion testing.

Condition	Metallic Powder Size [μm]	Bioactive Glass Powder Size [μm]	Ti-6Al-4V	Cp-Ti
			Failure Strength [MPa] ($n = 5$)	Failure Strength [MPa] ($n = 5$)
Low Flux	0-45	45 - 90	17 ± 2	13 ± 5
		90 - 180	20 ± 3	13 ± 3
	45 - 106	45 - 90	14 ± 3	8 ± 3
		90 - 180	20 ± 6	8 ± 2
High Flux	45 - 106	90 - 180	7 ± 5	5 ± 4

The effect of spraying under the high flux condition over the low flux condition on mechanical strength is insignificant for the control coatings. However, a statistically significant decrease in mechanical strength was noted for the coatings fabricated from 45 - 106 μm Ti-6Al-4V powder and 90 - 180 μm bioactive glass powder when sprayed under the high flux deposition condition, 7 ± 5 MPa, when compared to the low flux deposition condition, 20 ± 6 MPa. Additional work is necessary to ascertain whether the reduction of the stand-off distance and the increase in gaseous flow rates will have a significant effect on the mechanical properties of all the composite coatings.

The fracture surfaces and fracture modes are shown in Fig. 5-36 to 5-38. A cohesive failure of the coating was observed for coatings that were fabricated from Ti-6Al-4V alloy and 45 - 90 μm bioactive glass powder blends and mixed mode failure for the coatings fabricated from the Ti-6Al-4V alloy and 90 - 180 μm bioactive glass powder blends. The failures occurred at 20 ± 3 MPa, which was comparable to the bond strength of the epoxy (20 ± 2 MPa). Mixed mode failures were observed for the composite coatings fabricated from -45 μm Cp-Ti powder, with substantial portions of coating cohesive failure occurring at 13 ± 3 MPa (see Table 5-9 and Fig. 5-36 to 5-38). Composite coatings fabricated from 45 - 106 μm Cp-Ti powder had coating cohesive failure occurring at a breaking stress of 8 ± 3 MPa. A possible explanation for the differences in failure mode and stress may be the differences in bioactive glass morphology between the Ti-6Al-4V-based and Cp-Ti-based composite coatings. The bioactive glass remained dispersed, circular, and discrete (see Fig. 5-7) in the case of Ti-6Al-4V-based composite coatings, while a globular agglomerated morphology was observed for Cp-Ti-based coatings (see Fig. 5-9). Therefore, it is possible that in the Ti-6Al-4V-based composite coatings the bioactive glass acts to increase the cohesive coating bond strength by 1) localizing shear in the tougher metallic alloy matrix of the coating through load shedding, 2) act as a barrier to crack propagation by deflecting the crack within the coating, or 3) act as a barrier to crack propagation by arresting and blunting the crack when the crack passes through the ceramic inclusion. Crack arresting by solid particle inclusions has been observed by Lima *et al.* [112], crack deflection, and shear localization and confinement is a common

strengthening mechanism in metal matrix composites with ceramic reinforcing phases [113-117]. Additionally, Xue *et al.* [118] found that Ti-6Al-4V alloy possessed a lower strain hardening index, 0.15, than that of Cp-Ti, 0.18; therefore, the strengthening provided by strain hardening through the localization of shear through load-shedding may be lesser in the case of Ti-6Al-4V alloy. Hence, the lower mechanical strength noted for the Cp-Ti-based coatings, with a maximum of 13 ± 3 MPa versus 20 ± 3 MPa for Ti-6Al-4V-based coatings, may be caused by the significant presence of an agglomerated glassy phase and reaction phases. The localization of significant portions of these phases in the microstructure (see Fig. 5-7) creates a glassy phase-matrix interfacial area that spans significant portions of the coating microstructure. It is possible that the agglomeration and localization of the glassy and interaction phases may provide a path for crack propagation along the matrix-glassy phase interface [117].

A representative micrograph of the mixed mode fracture surface taken from the coating fabricated from $< 45 \mu\text{m}$ Ti-6Al-4V alloy blended with $90 - 180 \mu\text{m}$ bioactive glass powder under the low flux deposition condition and the coating fabricated from $< 45 \mu\text{m}$ Cp-Ti blended with $45 - 90 \mu\text{m}$ bioactive glass powder under the low flux deposition condition is included in Fig. 5-40. Here, it can be seen that the piece of coating left behind on the surface appear to contain a translucent and/or transparent phase that likely corresponds to bioactive glass. Confirmation of the hypothesis discussed previously could be performed by examining the fracture surfaces in the SEM for evidence of reaction phase.

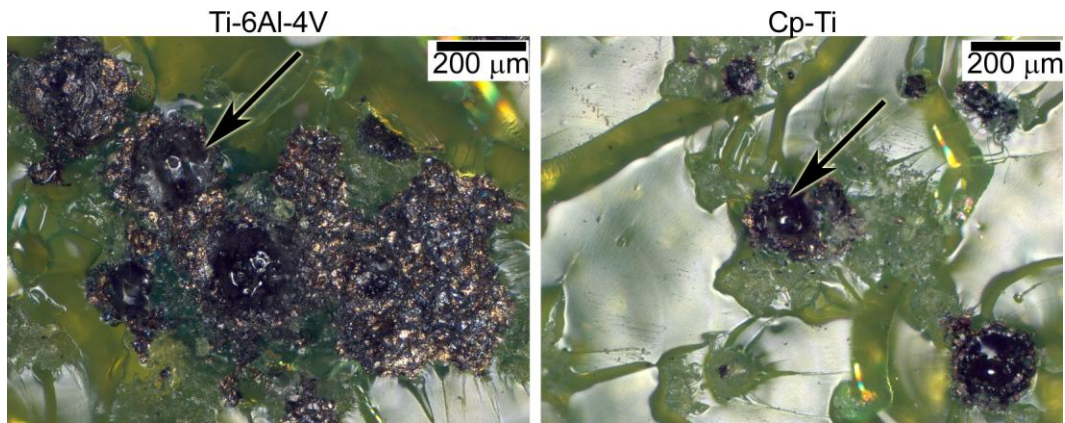


Figure 5-40. Representative optical micrographs of the epoxy-side of the fracture surfaces. Black arrows indicate a translucent/transparent phase that may be bioactive glass. Micrographs demonstrate epoxy-cohesive failure, epoxy-coating adhesive failure, and coating cohesive failure. Left image: coating fabricated from $< 45 \mu\text{m}$ Ti-6Al-4V alloy blended with $90 - 180 \mu\text{m}$ bioactive glass deposited under the low flux deposition condition; right image: coating fabricated from $< 45 \mu\text{m}$ Cp-Ti blended with $45 - 90 \mu\text{m}$ bioactive glass deposited under the low flux deposition condition.

Furthermore, the localization of pores in the Cp-Ti-based composite coatings fabricated from $45 - 106 \mu\text{m}$ Cp-Ti powder around the glassy phase may also contribute to the notable and statistically significant decrease in coating strength from $13 \pm 5 \text{ MPa}$ to $8 \pm 3 \text{ MPa}$, observed on addition of bioactive glass. The localization of strain between voids has been shown to lead to crack formation and propagation [116]. Additionally, the composite coatings fabricated under the high flux condition have large regions of glassy phase-titanium intermixing and reaction (see Fig. 5-7, 5-8, 5-21, and 5-22). The Ti-6Al-4V-based high flux composite coating demonstrates as statistically significant lower strength than the corresponding coatings fabricated under the low flux condition, at $7 \pm 5 \text{ MPa}$ for the high flux condition versus $20 \pm 6 \text{ MPa}$ for the low flux condition. The Cp-Ti-based coating exhibits a lower strength but it is not of statistical significance, at 5

± 4 MPa for the high flux condition versus 8 ± 2 MPa for the low flux condition. Therefore, based on the observations of the Cp-Ti-based composite coatings and composite coatings fabricated under the high flux condition, it is possible that the significant glassy phase-matrix interfacial area leads to a loss of the reinforcement provided by the bioactive glass and a deterioration of coating strength.

The tensile strength exhibited by the Ti-6Al-4V-based composites (most promising coating with 20 ± 3 MPa strength) is comparable or superior to other biomedical coatings fabricated with plasma and HVOF spraying, such as HA, HA-Cp-Ti, and HA-Ti-6Al-4V alloy composites, which all have reported bond strengths on the order of 10 to 25 MPa [21,55,57,58,60,62,67]. However, HVOF and plasma sprayed coatings will be dense and will likely not have pores in the size regime necessary to support tissue ingrowth and the development of vascular tissue [11,12,64]. As the coatings presented in this work are highly porous with comparable bond strengths this suggests they may represent a superior choice to dense coatings. Therefore, the use of the Ti-6Al-4V-bioactive-glass-based composite coatings may be a superior choice due to the possible osteoproducity from the bioactive glass, the potential ability to support tissue ingrowth, the development of vascular tissue, and the comparable strength to dense coatings.

5.8. Thermodynamic and Heat Transfer Modelling

A thermodynamic and heat transfer analysis was conducted to establish theoretical support for the mechanisms proposed in this study. An Ellingham diagram was constructed (see Fig. 5-41a) with data obtained from the FactSage™ database. There are a number of intersections between various oxidation reactions which provide insight into the unexpected absence of Al_2O_3 in the oxide scale (see Fig. 5-21 and 5-22). These intersections include: TiO and alumina (Al_2O_3) at 1121°C , TiO and lime (CaO) at 2099°C , Al_2O_3 and Ti_2O_3 at 2357°C , CaO and Ti_2O_3 at 2372°C , CaO and Al_2O_3 at 2375°C , TiO_2 and CaO at 2761°C , and Al_2O_3 and TiO_2 at 3061°C . Of particular note is the intersection of the line for the oxidation of aluminum to alumina (Al_2O_3) and the formation of TiO at 1121°C . The presence of this intersection indicates that above 1121°C , titanium would reduce Al_2O_3 to metallic aluminum while forming TiO. However, as this reaction occurs at a much lower temperature than the other Al_2O_3 intersections it is unlikely that the other reactions will be of consequence for Ti-6Al-4V-based coatings. The interactions between CaO and the titanium oxides are unlikely to be of consequence since formation of interaction phases such as CaTiO_3 and CaTiSiO_5 will occur at lower temperatures [103,106,119]. As discussed earlier, there exists a ternary eutectic at 1365°C in the CaO-SiO₂-TiO₂ system (see Fig. 5-24). Therefore, the additional presence of a liquid phase at these lower temperatures means it is likely that the formation of interaction phases would have occurred previous to the higher temperature intersections. Further examination (see Fig. 5-41b) indicates that the reduction of Al_2O_3 by the

oxidation of titanium to TiO is quite endothermic. It is possible that the cooling provided by this reduction may be responsible for the lack of reaction phases in the case of Ti-6Al-4V-based composite coatings, as evidenced by the lack of combeite and perovskite peaks and the high peak intensities for TiO_x for Ti-6Al-4V-based composite coating fabricated under low flux condition (see Fig. 5-21 and 5-22). The reaction between titanium and alumina also indicates a minimum temperature that was likely reached by the metallic particles during deposition since no selective oxidation of aluminum occurred during deposition as it is was expected for alumina to be present within the scale. Furthermore, the reduction of alumina and the production of TiO, metallic aluminum, and titanium aluminides, have been reported in the literature at temperatures above 1100°C [120,121].

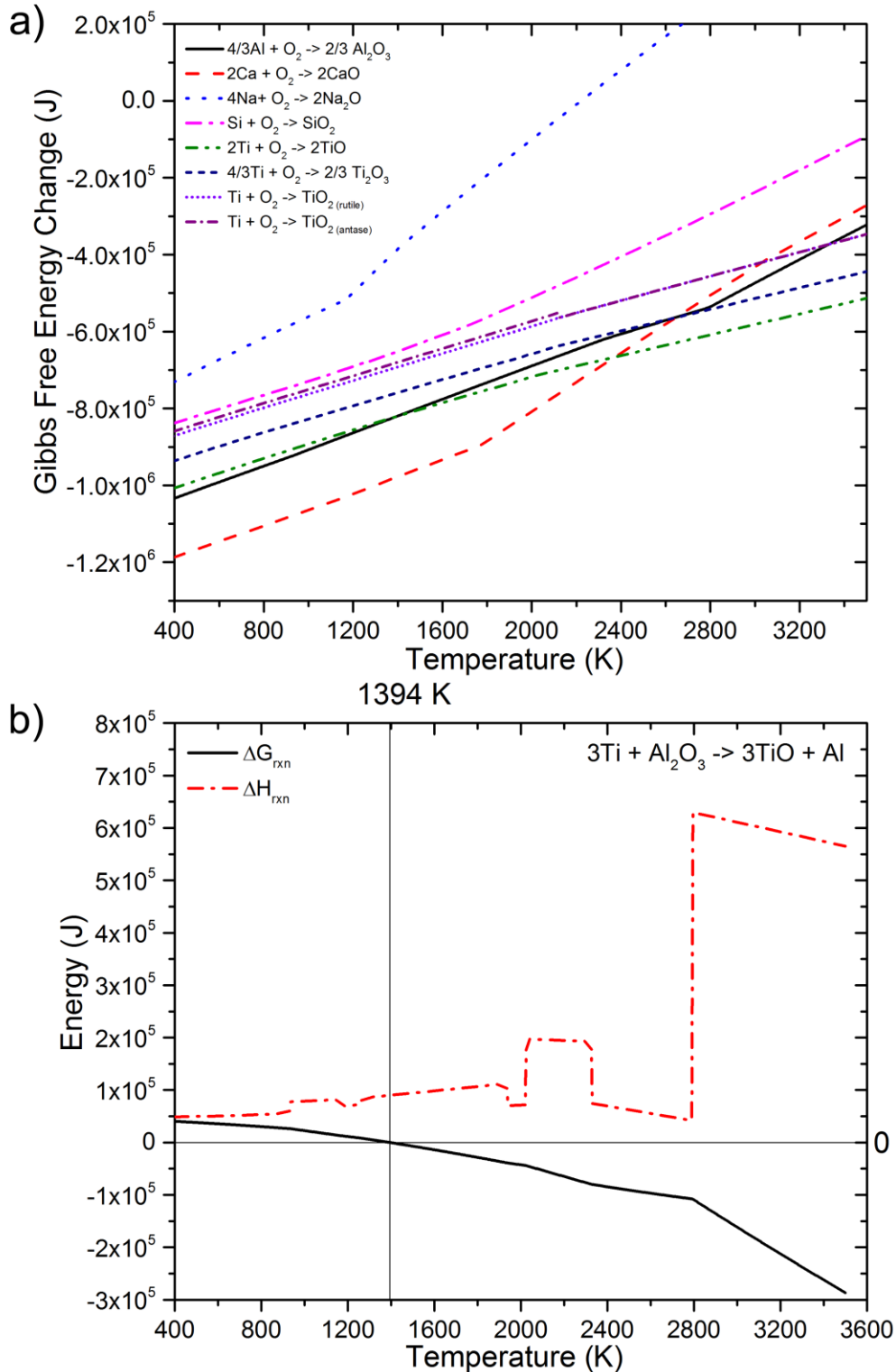


Figure 5-41. Thermodynamic reaction plots: a. Ellingham diagram of major oxides present within the system; b. Gibbs free energy and enthalpy of reaction for the reduction of alumina through the oxidation of Ti to TiO.

A lumped capacitance model was used to estimate the relative changes in particle temperatures achieved in the flame jet by Ti-6Al-4V alloy, Cp-Ti, and bioactive glass powder under the low and high flux conditions. As stated previously, the velocity of each particle was unknown; therefore, the model was solved in an iterative fashion with particle velocity as a variable between 10 to 40 m/s (see Fig. 5-42). The Biot number for each type of particle in flight was no greater than 2.2×10^{-3} , 2.4×10^{-3} , and 8.4×10^{-3} for Ti-6Al-4V alloy, Cp-Ti, and bioactive glass respectively. These values are below 0.1 confirming the assumption of lumped capacitance. The Reynolds number for each type of particle in flight was no greater than 11 and 19 for the metallic particles and bioactive glass particles respectively. The calculated values of the Reynolds number are below 5×10^6 validating the assumption of laminar flow. The predicted temperatures are lower for particles sprayed under the high flux condition than those under the low flux condition, mostly likely due to the shorter residence time in the flame and shorter stand-off distance. The reduced stand-off distance will increase the degree of flame impingement on the substrate. Therefore, it is likely that the substantially increased number of reactions that were observed in the case of the coatings fabricated under the high flux condition was due to heating from the impingement of the flame on the substrate. Based on the temperature profiles shown in Fig. 5-39, it is likely that metallic particles with diameters less than $76 \mu\text{m}$ were fully molten since the particle temperatures exceeded the melting point of Cp-Ti and Ti-6Al-4V alloy ($1600\text{-}1650^\circ\text{C}$ [91] and 1668°C [99], respectively), while the larger particles were within the β -phase region of the titanium phase diagram [99].

The bioactive glass particles in the 45 to 90 μm size range were likely molten (greater than 1200°C) [94] and cooled rapidly, avoiding crystallization. The larger bioactive glass particles on the higher side of the 90 to 180 μm range were more likely to have been heated above the softening point of the bioactive glass but below the crystallization point (610°C) [94], with some particles not softening sufficiently to be captured in the coating. The lack of softening is supported by the lower degree of glass incorporation (see Table 5-4) for coatings produced with the 90 to 180 μm bioactive glass powder. The bioactive glass powder reached lower temperatures during deposition than either of the metallic powders due to the lower thermal conductivity of glass. The Ti-6Al-4V alloy powder particles had lower temperatures than the Cp-Ti powder particles of similar size. The usually lower porosity content of the Cp-Ti control coatings and many of the Cp-Ti-based composite coatings (see Fig. 5-8, 5-17, 5-18, Table 5-3 and 5-4) as well as the presence of CaTiO_3 , $\text{Na}_2\text{Ca}_2\text{Si}_3\text{O}_9$ phases present in the Cp-Ti-based composite coatings (see Fig. 5-21 and 5-22) support the observation that the Ti-6Al-4V alloy particles attained lower temperatures during the deposition process. There were exceptions to the generalization that Cp-Ti-based coatings had a higher porosity than Ti-6Al-4V-based coatings but these exceptions were attributed to other factors, as discussed previously, such as localized reactions and impingement of the flame during high flux deposition.

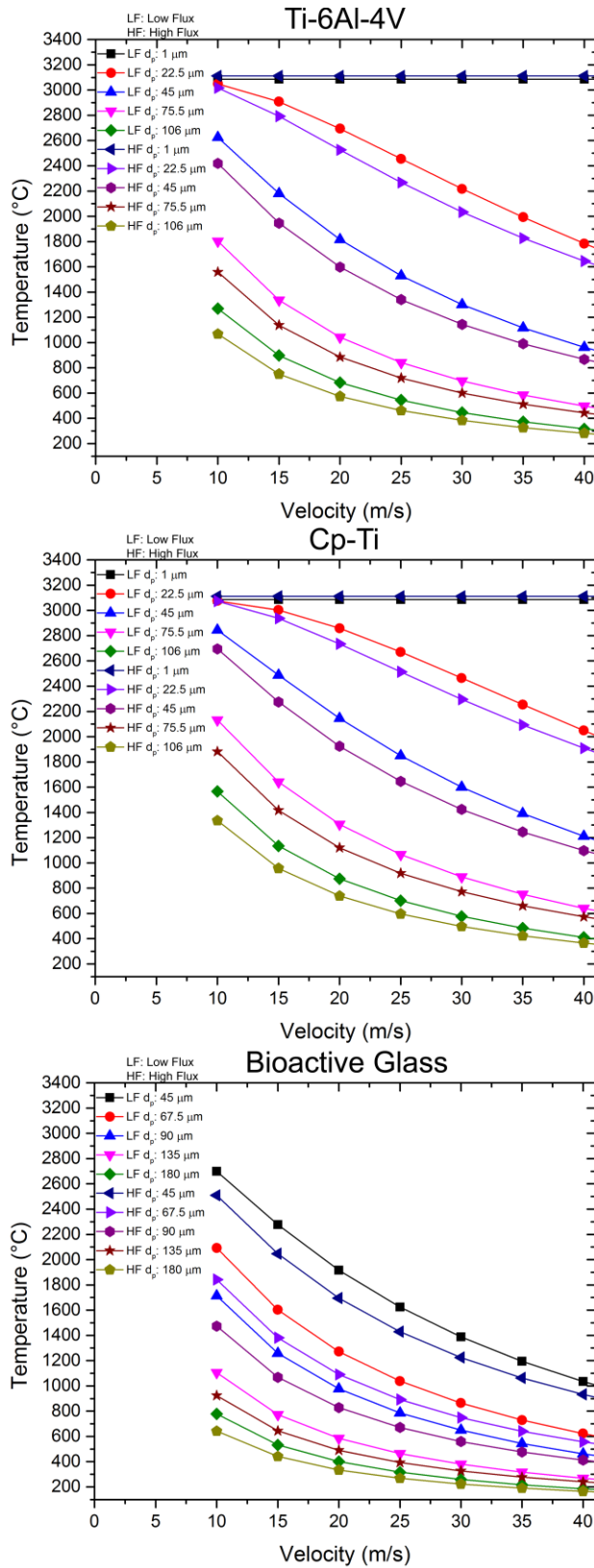


Figure 5-42. Theoretical particle temperatures attained during flame spray deposition as determined by heat transfer modeling.

Furthermore, the combination of the lower particle temperatures of the Ti-6Al-4V alloy and the endothermic reduction of alumina that occurred at 1121°C support the fact that bioactive glass would cool more slowly for Cp-Ti-based composites. Therefore, the bioactive glass is more likely to react with the surrounding matrix and crystallize upon cooling. The localization of defects as well as the loss of the dispersed glassy phase to deflect cracks when coupled with the higher temperature particles during flight may cause the noted decrease in cohesive strength. It is likely that the higher temperature Cp-Ti particles dissolved more oxygen during flight. The incorporation of oxygen into the titanium matrix is commonly associated with the production of brittle oxides and a decrease in cohesive strength [101,122]. The substantially lower strength of the high flux composite coatings also suggests that the presence of reaction phases contributed to the embrittlement of the coating.

5.9. Selection of the Most Promising Coating

The work presented in this thesis has focused on characterizing the differences between coatings that were produced by altering the type of alloy, the flame spray deposition conditions, and the size distribution of the feedstock powder. Based upon the previously discussed work, a promising candidate coating for the new changing landscape coating system should possess:

1. Demonstrated *in vitro* bioactivity induced by an osteoproducer compound
2. A mechanical bond strength that is comparable, or superior, to existing biomedical coatings (10 to 25 MPa [21,55,57,58,60,62,67])
3. A spatially homogenous microstructure with a dispersed glassy phase
4. A high degree of porosity with a size distribution that is suitable for promoting the viable ingrowth of tissue (pore areas greater than $1000 \mu\text{m}^2$)
5. An amorphous and unreacted bioactive glass
6. A substantial proportion of incorporated bioactive glass phase with a size (feature areas greater than $1000 \mu\text{m}^2$) that is conducive to producing pores of sufficient size to encourage tissue ingrowth

Coatings were eliminated or selected based upon the above criteria. The controls were eliminated as there was no type A bioactive compound present within the coatings. The composite coatings fabricated with 180 - 250 μm bioactive glass were eliminated owing to the extreme heterogeneity (see Section 5.5.1 and 5.5.2). The high flux composite coatings that were not selected for further testing were eliminated based upon the presence of many reaction phases (see Section 5.5.3)

and the severe agglomeration of the bioactive glass (see Section 5.5.1). However, one high flux composite coating was tested further to ascertain the effects of selecting the high flux deposition condition on the *in vitro* bioactivity and mechanical properties. The Cp-Ti-based composites were eliminated based upon the negative result observed for the *in vitro* SBF immersion testing (see Section 5.6). However, the composite coatings deposited under the high flux condition were eliminated based upon the poor mechanical strength observed (see Section 5.7), 7 ± 5 MPa and 5 ± 4 MPa for Ti-6Al-4V-based and Cp-Ti-based respectively. Therefore, the remaining candidate coatings were the Ti-6Al-4V-based composite coatings fabricated under the low flux condition. The Ti-6Al-4V-based composite coatings containing 45 - 90 μm bioactive glass were less suitable than the corresponding coating containing 90 - 180 μm bioactive glass owing to the lower portion of suitable porosity present within each coating (see Section 5.5.2) and the higher mechanical bond strengths (see Section 5.7).

Therefore, based upon the criteria described above (see Fig. 5-43), the most promising coatings, as a candidate for a changing landscape coating, targeted for load-bearing bone fixation applications, are both of the Ti-6Al-4V-based composite coatings that contained the 90 - 180 μm bioactive glass powder which were fabricated under the low flux deposition condition. The first candidate coating was fabricated with the < 45 μm Ti-6Al-4V alloy and possessed a greater portion of pore area, relative to the coating produced from 45 - 106 μm Ti-6Al-4V alloy, which could promote tissue ingrowth, and an unreacted dispersed glassy

phase. While, the corresponding coating fabricated from 45 - 106 μm Ti-6Al-4V alloy powder had a more spatially homogenous structure with a lower portion of pore area that could promote tissue ingrowth, and partial crystallization of the bioactive glass. However, the latter coating also possessed many bioactive glass particles that may act as porogens and a higher overall porosity. Both coatings exhibited comparable bioactive responses and mechanical bonds strengths. Therefore, both of the coatings described here are the best candidates for the new changing landscape coating system targeted at load-bearing bone fixation implants.

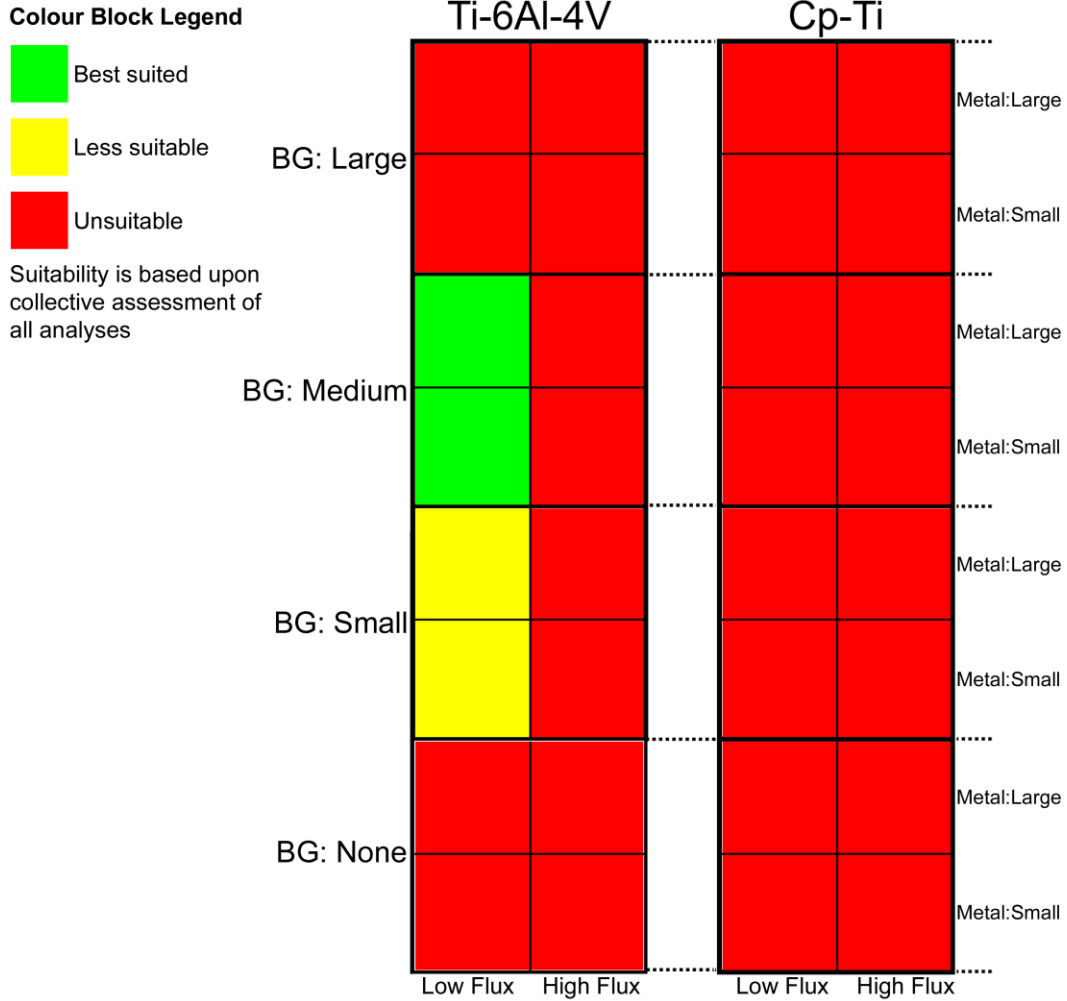


Figure 5-43. Overall schematic indicating which coatings are the most suitable candidates for the changing landscape coating system on the basis of an overall assessment of the results from each analysis technique. Each tile represents an individual combination of powder size, composition, and deposition condition. Legend: Metal - Small refers to < 45 µm powder and Large refers to 45 - 106 µm powder; Bioactive Glass: Small refers to 45 - 90 µm powder, Medium refers to 90 - 180 µm powder, and Large refers to 180 - 250 µm powder.

Chapter 6 – Conclusions and Future

Work

6.1. Conclusions

Load-bearing implants are often construed of bio-inert materials, such as titanium, while class A bioactive materials, such as bioactive glass, are brittle. Therefore, there is a need to develop a composite material suitable for load-bearing biomedical applications. The composite material should be mechanically stable, should have a porous structure conducive to tissue ingrowth, and should actively promote osteoblast attachment and proliferation. To facilitate this end a new composite coating of a load-bearing alloy and a resorbable bioactive material was proposed. The coating structure may be described as a porous metallic scaffold with partially encapsulated particulates of resorbable bioactive material. The resorbable bioactive material would initiate surface mineralization and induce the proliferation of osteoblasts. Additionally, the bioactive material would act as a porogen which would create a new pore after dissolution. The new pore will have an undercut keyhole-like shape and its creation will increase the mechanical interlocking of bone tissue with the implant provided the glass, and surrounding porosity, is large enough to create a suitable pore structure with individual pore diameters of at least 40 to 80 μm . This coating system is termed a changing landscape coating. In this work, a titanium or titanium alloy powder was blended

with 45S5 bioactive glass powder and deposited with the flame spray technique targeted for orthodontic and bone fixation applications.

This study illustrated the effects of the type of titanium alloy, the ratio of titanium alloy to bioactive glass, and alteration of the feedstock particle size distribution on the final coating performance. Additionally, two sets of depositions conditions were explored. The effects of the aforementioned variables on the morphology, microstructure, and phases formed in the flame-sprayed composite coatings were studied. The consequences of these factors on the *in vitro* bioactive response as well as the release of metallic ions *in vitro* were explored. The contribution of the coating porosity to osseointegration of an implant with a surface bioactive glass-Ti-based composite coating was discussed. The consequences of the microstructure, phases, and porosity on the mechanical response were studied by adhesion testing. Additionally, thermodynamic and heat transfer modeling was conducted to gain insight into the effects of the titanium alloy, the particle size distributions, and deposition conditions on the as-sprayed coating. The work performed shows that type of titanium alloy powder used (Ti-6Al-4V alloy or Cp-Ti powder) for flame spray deposition has far reaching effects, that are beneficial if Ti-6Al-4V alloy is used, on the porosity, the phases formed, the theoretical particle temperatures attained, the mechanical response, and the *in vitro* bioactive response of the composite coating.

Utilization of Ti-6Al-4V alloy, instead of Cp-Ti powder for flame spray deposition has numerous advantages. A greater portion of pore area that corresponds to circular pores with diameters between 36 μm and 112 μm , as well in excess of 112 μm , was obtained. These pores may promote tissue ingrowth, osseointegration, and vascularization. Therefore, a Ti-6Al-4V alloy-based composite coating may have a pore structure that promotes implant integration. Additionally, the surface of the coating has exposed bioactive glass in the case of Ti-6Al-4V-based composite coatings. The bioactive glass remains amorphous and does not react with the surrounding matrix while it crystallizes and reacts with the titanium matrix in the case of Cp-Ti based coatings and Ti-6Al-4V-based composite coatings have mechanical bond strengths (20 ± 3 MPa for the most promising) that are comparable to other dense biomedical coatings.

The *in vitro* formation of HA occurs after 7 days of immersion for Ti-6Al-4V – bioactive glass composite coatings; while, formation does not occur until after 14 days of immersion for the < 45 μm Ti-6Al-4V control coating sprayed under the low flux condition and all control coatings sprayed under the high flux condition. The lack of formation on the other low flux control coatings was attributed to the lesser amount of TiO_2 present on these control samples. No HA formation was observed in the tested time period for Cp-Ti – bioactive glass composite coatings. The rapid formation of HA for Ti-6Al-4V-based composite coatings suggests that incorporation of the bioactive glass enhances the bioactive response in comparison to the Ti-6Al-4V alloy control coating. Additionally, the

osteopductive properties of the bioactive glass should promote rapid integration and enhanced implant viability *in vivo*. However, the Ti-6Al-4V-based coatings released vanadium ions *in vitro*. These ions may potentially result in implant failure or rejection *in vivo* due to the toxicity of vanadium if the concentration is high enough to induce local cell death or chronic toxic effects.

The selection of lower gas flow rates and higher stand-off distance during flame spraying resulted in higher coating tensile strengths (up to 20 ± 3 MPa), fewer reaction phases, and a greater portion of pore area in the 1000 to 10,000 μm^2 and greater than 10 000 μm^2 pore size ranges, which is known to promote tissue ingrowth and vascularization. The Ti-6Al-4V-based composite coatings displayed a discrete and continuous glass phase. The glass phase was amorphous and there was minimal reaction phases formed. The Ti-6Al-4V-based composites were reinforced with the addition of bioactive glass and exhibited increasing tensile strength when the coatings were made with 90 - 180 μm bioactive glass powder when compared to those fabricated from 45 - 90 μm bioactive glass powder. The Cp-Ti-based composite coatings possessed a continuous and globular glassy phase that crystallized during deposition and reacted with the surrounding matrix to form CaTiO_3 . The Cp-Ti-based composite coatings also showed a markedly lower strength, with a maximum strength of 13 ± 3 MPa compared to 20 ± 3 MPa for Ti-6Al-4V-based composites. It was also found that the addition of bioactive glass resulted in a decrease of coating cohesion strength for Cp-Ti-based coatings fabricated with the 45 - 106 μm metallic powder. Furthermore, it was found that

both CaTiO_3 and CaTiSiO_5 formed for coatings deposited under the high flux condition, supporting the hypothesis that a greater degree of reaction occurred when the flame spray gas flow rates were higher and the stand-off distance was lower to produce higher flame temperatures.

Thermodynamic and heat transfer modeling showed that the bioactive glass particles reached a lower temperature during deposition when compared to the metallic particles owing to the higher specific heat capacity of Ti-6Al-4V alloy. The Ti-6Al-4V alloy particles reached a lower temperature than the Cp-Ti particles in flight. Additionally, the absence of Al_2O_3 in the oxide scale of Ti-6Al-4V-based composite coatings suggests that the endothermic reduction of Al_2O_3 at temperatures in excess of 1121°C occurred for Ti-6Al-4V-based composite coatings. The combined effects of the lower particle temperature during deposition and this endothermic reaction likely created the environment that allowed for rapid cooling of the bioactive glass thus preserving the amorphous nature of the glass. Evidence of the lower particle temperature for Ti-6Al-4V-based coatings during deposition was present in the morphology, microstructure and phase composition. Modeling showed that particles attained lower temperatures when deposited under the high flux deposition condition rather than the low flux deposition condition. However, the greater extent of reaction observed for coatings deposited under the high flux deposition condition despite the lower predicted particle temperatures may be due to the impingement of the

torch flame on the substrate during deposition owing to the decreased stand-off distance.

The work presented herein indicates that the most promising coatings, as a candidate for a changing landscape coating on a load-bearing bone fixation implant, are both of the Ti-6Al-4V-based composites fabricated with the 90 -180 μm bioactive glass size under the low flux deposition condition; the coating fabricated with the $< 45 \mu\text{m}$ Ti-6Al-4V alloy had a greater portion of pore area that could promote tissue ingrowth and no crystallization or reaction of the bioactive glass. While, the corresponding coating fabricated from 45 - 106 μm Ti-6Al-4V alloy had a more spatially homogenous structure with a lower portion of pore area that could promote tissue ingrowth and partial crystallization of the bioactive glass. However, the latter coating also possessed many bioactive glass particles that may act as porogens. Therefore, both of the coatings described here, which possess comparable mechanical bond strength and bioactive response, are the best candidates for the new changing landscape coating system.

6.2. Future Work

The results of this research suggest that these coatings are promising. However, further work is necessary to further develop and characterize these coatings. Several potential areas for future work include:

- Microfractography of the failed ASTM Standard C633 coatings. The fracture mechanism, origin of crack initiation, and path of crack propagation were not established in this study. SEM with EDX examination of the fracture surface to locate phases present along the fracture surface would help determine what path the crack followed
- Characterization of the coating topography to obtain a fractal parameter. Performing a fractal analysis of the roughness of a coating will aid in determining whether or not osteoblasts will be able to spread out and attach to a coating.
- Optimization of porosity, strength and morphology by fine-tuning deposition parameters. A potential link was shown between the bioactive glass morphology, the mechanical strength and the porosity of the coating. Additional factors, such as excessive oxidation, increased the amount of porosity, but likely contributed to a lower strength, and as such, there exists room for optimization.
- Characterization of the shear, bending, and fatigue behaviour of the coatings to establish the load bearing capabilities of the composite coatings. The

adhesion testing conducted in this study accounts for neither the complicated loading condition present *in vivo* nor the friability of the coating on a cylindrical surface.

- Further work must also be performed to assess the levels of potential vanadium toxicity for the Ti-6Al-4V-based composite coatings; studies on the attachment of cells must also be performed. This work can be informed by the fractal analysis and will provide a better measure of the *in vivo* response and bioactivity of the coatings.
- Studies on the properties of the coating when deposited upon a cylindrical, helical screw, and/or orthodontic implant to assess whether or not the desired microstructure can be obtained on the new geometry.

Chapter 7 – References

- [1] S.G. Steinemann, Titanium - the material of choice? *Periodontol.* 2000. 17 (1998) 7-21.
- [2] L. Hench, Bioceramics, *J Am Ceram Soc.* 81 (1998) 1705-1728.
- [3] L.L. Hench, The story of Bioglass (R), *J. Mater. Sci. : Mater. Med.* 17 (2006) 967-978.
- [4] T. Kokubo, H. Kim, M. Kawashita, Novel bioactive materials with different mechanical properties, *Biomaterials.* 24 (2003) 2161-2175.
- [5] J.E. Ellingsen, Surface configurations of dental implants, *Periodontol.* 2000. 17 (1998) 36-46.
- [6] F. Javed, K. Almas, R. Crespi, G.E. Romanos, Implant Surface Morphology and Primary Stability: Is There a Connection? *Implant Dentistry.* 20 (2011) 40.
- [7] A. Rakngarm, Y. Miyashita, Y. Mutoh, Formation of hydroxyapatite layer on bioactive Ti and Ti-6Al-4V by simple chemical technique, *J. Mater. Sci. : Mater. Med.* 19 (2008) 1953-1961.
- [8] L. Jiang, X. Lu, Y. Leng, S. Qu, B. Feng, J. Weng, Micropatterned TiO₂ effects on calcium phosphate mineralization, *Mater. Sci. Eng. , C.* 29 (2009) 2355-2359.
- [9] B. Liang, S. Fujibayashi, J. Tamura, M. Neo, H. Kim, M. Uchida, T. Kokubo, T. Nakamura, Bone-bonding ability of anodic oxidized titanium, *240-2* (2003) 923-926.
- [10] K. Ou, Y. Shih, C. Huang, C. Chen, C. Liu, Preparation of bioactive amorphous-like titanium oxide layer on titanium by plasma oxidation treatment, *Appl. Surf. Sci.* 255 (2008) 2046-2051.
- [11] F.M. Klenke, Y. Liu, H. Yuan, E.B. Hunziker, K.A. Siebenrock, W. Hofstetter, Impact of pore size on the vascularization and osseointegration of ceramic bone substitutes in vivo, *J. Biomed. Mater. Res. , Part A.* 85A (2008) 777-786.
- [12] R.A. Underwood, M.L. Usui, G. Zhao, K.D. Hauch, M.M. Takeno, B.D. Ratner, A.J. Marshall, X. Shi, J.E. Olerud, P. Fleckman, Quantifying the effect

- of pore size and surface treatment on epidermal incorporation into percutaneously implanted sphere-templated porous biomaterials in mice, *J. Biomed. Mater. Res. , Part A.* 98A (2011) 499-508.
- [13] L. Pawlowski, *The Science and Engineering of Thermal Spray Coatings*, 2nd ed., John Wiley & Sons, Chichester, UK, 2008.
- [14] D.C. Greenspan, L.L. Hench, Chemical and Mechanical-Behavior of Bioglass-Coated Alumina, *J. Biomed. Mater. Res.* 10 (1976) 503-509.
- [15] W. Cao, L. Hench, Bioactive materials, *Ceram. Int.* 22 (1996) 493-507.
- [16] T. Kokubo, Bioactive glass ceramics: properties and applications, *Biomaterials.* 12 (1991) 155-163.
- [17] S. Bauer, P. Schmuki, K. von der Mark, J. Park, Engineering biocompatible implant surfaces Part I: Materials and surfaces, *Progress in Materials Science.* 58 (2013) 261-326.
- [18] S.J. Simske, R.A. Ayers, T.A. Bateman, Porous materials for bone engineering, *Porous Materials for Tissue Engineering.* 250 (1997) 151-182.
- [19] A. Ravaglioli, A. Krajewski, Implantable porous bioceramics, *Porous Materials for Tissue Engineering.* 250 (1997) 221-230.
- [20] K. Lai, W. Shen, C. Chen, C. Yang, W. Hu, G. Chang, Failure of hydroxyapatite-coated acetabular cups - Ten-year follow-up of 85 Landos Atoll arthroplasties, *J. Bone Joint Surg. Br.* 84B (2002) 641-646.
- [21] K. Khor, C. Yip, P. Cheang, Ti-6Al-4V/hydroxyapatite composite coatings prepared by thermal spray techniques, *J. Therm. Spray Technol.* 6 (1997) 109-115.
- [22] J. Lee, H. Kim, Y. Koh, Highly porous titanium (Ti) scaffolds with bioactive microporous hydroxyapatite/TiO₂ hybrid coating layer, *Mater Lett.* 63 (2009) 1995-1998.
- [23] L.L. Hench, H.A. Paschall, Direct Chemical Bond of Bioactive Glass-Ceramic Materials to Bone and Muscle, *J. Biomed. Mater. Res.* 7 (1973) 25-42.
- [24] T.K. Greenlee, C.A. Beckham, J.C. Malmorg, A.R. Crebo, Glass Ceramic Bone Implant - Light Microscopic Study, *J. Biomed. Mater. Res.* 6 (1972) 235-244.

- [25] C. Beckham, T. Greenlee, A. Crebo, Bone Formation at a Ceramic Implant Interface, *Calcif. Tissue Res.* 8 (1971) 165-171.
- [26] H. Stanley, M. Hall, A. Clark, C. King, L. Hench, J. Berte, Using 45S5 bioglass cones as endosseous ridge maintenance implants to prevent alveolar ridge resorption: A 5-year evaluation, *Int. J. Oral Maxillofac. Implants.* 12 (1997) 95-105.
- [27] O. Peitl, G.P. LaTorre, L.L. Hench, Effect of crystallization on apatite-layer formation of bioactive glass 45S5, *J. Biomed. Mater. Res.* 30 (1996) 509-514.
- [28] T. Kokubo, H. Kushitani, S. Sakka, T. Kitsugi, T. Yamamuro, Solutions able to reproduce in vivo surface-structure changes in bioactive glass-ceramic A-W3, *J. Biomed. Mater. Res.* 24 (1990) 721-734.
- [29] T. Kokubo, H. Takadama, How useful is SBF in predicting in vivo bone bioactivity? *Biomaterials.* 27 (2006) 2907-2915.
- [30] M. Bohner, J. Lemaitre, Can bioactivity be tested in vitro with SBF solution? *Biomaterials.* 30 (2009) 2175-2179.
- [31] T. Himeno, M. Kawashita, H. Kim, T. Kokubo, T. Nakamura, Zeta-potential variation of bioactive titanium metal during apatite formation on its surface in simulated body fluid, *Bioceramics* 14. 218-2 (2002) 641-644.
- [32] A.R. Boccaccini, V. Maquet, Bioresorbable and bioactive polymer/Bioglass (R) composites with tailored pore structure for tissue engineering applications, *Composites Sci. Technol.* 63 (2003) 2417-2429.
- [33] H.H. Beherei, K.R. Mohamed, G.T. El-Bassyouni, Fabrication and characterization of bioactive glass (45S5)/titania biocomposites, *Ceram. Int.* 35 (2009) 1991-1997.
- [34] A. Slosarczyk, Z. Paszkiewicz, C. Paluszkiwicz, FTIR and XRD evaluation of carbonated hydroxyapatite powders synthesized by wet methods, *J. Mol. Struct.* 744 (2005) 657-661.
- [35] J.A. Nychka, D. Li, B. Alexander, In vitro bioactivity of 45S5 bioactive glass as a function of indentation load, *Journal of the Mechanical Behavior of Biomedical Materials.* 1 (2008) 243-251.
- [36] R. Lima, B. Marple, H. Li, K. Khor, Biocompatible nanostructured high-velocity oxyfuel sprayed titania coating: Deposition, characterization, and mechanical properties, *J. Therm. Spray Technol.* 15 (2006) 623-627.

- [37] M. Lindgren, M. Astrand, U. Wiklund, H. Engqvist, Investigation of boundary conditions for biomimetic HA deposition on titanium oxide surfaces, *J. Mater. Sci. : Mater. Med.* 20 (2009) 1401-1408.
- [38] E. Kontonasaki, T. Zorba, L. Papadopoulou, E. Pavlidou, X. Chatzistavrou, K. Paraskevopoulos, P. Koidis, Hydroxy carbonate apatite formation on particulate bioglass in vitro as a function of time, *Cryst. Res. Technol.* 37 (2002) 1165-1171.
- [39] M.H. Fathi, A. Hanifi, V. Mortazavi, Preparation and bioactivity evaluation of bone-like hydroxyapatite nanopowder, *J. Mater. Process. Technol.* 202 (2008) 536.
- [40] W.J. Wu, G.H. Nancollas, Kinetics of nucleation and crystal growth of hydroxyapatite and fluorapatite on titanium oxide surfaces, *Colloids Surf. , B.* 10 (1997) 87-94.
- [41] E. Verne, M. Ferraris, A. Ventrella, L. Paracchini, A. Krajewski, A. Ravaglioli, Sintering and plasma spray deposition of bioactive glass-matrix composites for medical applications, *J. Eur. Ceram. Soc.* 18 (1998) 363-372.
- [42] R.L. Reis, F.J. Monteiro, G.W. Hastings, Stability of Hydroxylapatite Plasma-Sprayed Coated Ti-6al-4v Under Cyclic Bending in Simulated Physiological Solutions, *J. Mater. Sci. : Mater. Med.* 5 (1994) 457-462.
- [43] I. Rehman, M. Karsh, L.L. Hench, W. Bonfield, Analysis of apatite layers on glass-ceramic particulate using FTIR and FT-Raman spectroscopy, *J. Biomed. Mater. Res.* 50 (2000) 97-100.
- [44] H. Kawahara, Y. Soeda, K. Niwa, M. Takahashi, D. Kawahara, N. Araki, *In vitro* study on bone formation and surface topography from the standpoint of biomechanics, *J. Mater. Sci. Mater. Med.* 15 (2004) 1297-1307.
- [45] J. Legoux, F. Chellat, R. Lima, B. Marple, M. Bureau, H. Shen, G. Candeliere, Development of osteoblast colonies on new bioactive coatings, *J. Therm. Spray Technol.* 15 (2006) 628-633.
- [46] J.A. Nychka, S.L.R. Mazur, S. Kashyap, D. Li, F. Yang, Dissolution of bioactive glasses: The effects of crystallinity coupled with stress, *JOM.* 61 (2009) 45-51.
- [47] M. Uchida, H. Kim, T. Kokubo, S. Fujibayashi, T. Nakamura, Structural dependence of apatite formation on titania gels in a simulated body fluid, *J. Biomed. Mater. Res. Part A.* 64A (2003) 164-170.

- [48] G. Ciobanu, G. Carja, O. Ciobanu, I. Sandu, A. Sandu, SEM and EDX studies of bioactive hydroxyapatite coatings on titanium implants, *Micron*. 40 (2009) 143-146.
- [49] S. Overgaard, K. Soballe, K. Josephsen, E. Hansen, C. Bunger, Role of different loading conditions on resorption of hydroxyapatite coating evaluated by histomorphometric and stereological methods, *J. Orthop. Res.* 14 (1996) 888-894.
- [50] D. Packham, Surface energy, surface topography and adhesion, *Int J Adhes Adhes.* 23 (2003) 437-448.
- [51] G. Iezzi, G. Aprile, D. Tripodi, A. Scarano, A. Piattelli, V. Perrotti, Implant Surface Topographies Analyzed Using Fractal Dimension, *Implant Dentistry*. 20 (2011) 131.
- [52] S. Amada, H. Yamada, Introduction of fractal dimension to adhesive strength evaluation of plasma-sprayed coatings, *Surf. Coat. Technol.* 78 (1996) 50-55.
- [53] S. Amada, T. Hirose, Planar fractal characteristics of blasted surfaces and its relation with adhesion strength of coatings, *Surf. Coat. Technol.* 130 (2000) 158-163.
- [54] S. Amada, T. Hirose, Influence of grit blasting pre-treatment on the adhesion strength of plasma sprayed coatings: fractal analysis of roughness, *Surf. Coat. Technol.* 102 (1998) 132-137.
- [55] K. Khor, Y. Gu, D. Pan, P. Cheang, Microstructure and mechanical properties of plasma sprayed HA/YSZ/Ti-6Al-4V composite coatings, *Biomaterials*. 25 (2004) 4009-4017.
- [56] M. Gaona, R.S. Lima, B.R. Marple, Nanostructured titania/hydroxyapatite composite coatings deposited by high velocity oxy-fuel (HVOF) spraying, *Mater. Sci. Eng. , A*. 458 (2007) 141-149.
- [57] X. Zheng, M. Huang, C. Ding, Bond strength of plasma-sprayed hydroxyapatite/Ti composite coatings, *Biomaterials*. 21 (2000) 841-849.
- [58] Y. Tsui, C. Doyle, T. Clyne, Plasma sprayed hydroxyapatite coatings on titanium substrates Part 1: Mechanical properties and residual stress levels, *Biomaterials*. 19 (1998) 2015-2029.
- [59] V. Sergo, O. Sbaizero, D.R. Clarke, Mechanical and chemical consequences of the residual stresses in plasma sprayed hydroxyapatite coatings, *Biomaterials*. 18 (1997) 477-482.

- [60] M. Espanol, V. Guipont, K. Khor, M. Jeandin, N. Llorca-Isern, Effect of heat treatment on high pressure plasma sprayed hydroxyapatite coatings, *Surf. Eng.* 18 (2002) 213-218.
- [61] K.A. Gross, C.C. Berndt, H. Herman, Amorphous phase formation in plasma-sprayed hydroxyapatite coatings, *J. Biomed. Mater. Res.* 39 (1998) 407-414.
- [62] K.A. Khor, Y.W. Gu, C.H. Quek, P. Cheang, Plasma spraying of functionally graded hydroxyapatite/Ti-6Al-4V coatings, *Surf Coat Technol.* 168 (2003) 195-201.
- [63] Y. Wang, C. Li, A. Ohmori, Influence of substrate roughness on the bonding mechanisms of high velocity oxy-fuel sprayed coatings, *Thin Solid Films.* 485 (2005) 141-147.
- [64] R. Lima, K. Khor, H. Li, P. Cheang, B. Marple, HVOF spraying of nanostructured hydroxyapatite for biomedical applications, *Mater. Sci. Eng. , A.* 396 (2005) 181-187.
- [65] R. Lima, B. Marple, High Weibull modulus HVOF Titania coatings, *J. Therm. Spray Technol.* 12 (2003) 240-249.
- [66] R. Lima, B. Marple, Optimized HVOF titania coatings, *J. Therm. Spray Technol.* 12 (2003) 360-369.
- [67] H. Li, K. Khor, P. Cheang, Effect of the powders' melting state on the properties of HVOF sprayed hydroxyapatite coatings, *Mater. Sci. Eng. , A.* 293 (2000) 71-80.
- [68] R. Bandyopadhyay, P. Nylen, A computational fluid dynamic analysis of gas and particle flow in flame spraying, *J. Therm. Spray Technol.* 12 (2003) 492-503.
- [69] A. McDonald, C. Moreau, S. Chandra, Use of thermal emission signals to characterize the impact of fully and partially molten plasma-sprayed zirconia particles on glass surfaces, *Surf Coat Technol.* 204 (2010) 2323-2330.
- [70] G. Marot, J. Lesage, P. Demareaux, M. Hadad, S. Siegmann, M.H. Staia, Interfacial indentation and shear tests to determine the adhesion of thermal spray coatings, *Surf. Coat. Technol.* 201 (2006) 2080-2085.
- [71] M. Hadad, G. Marot, P. Demareaux, D. Chicot, J. Lesage, L. Rohr, S. Siegmann, Adhesion tests for thermal spray coatings: correlation of bond strength and interfacial toughness, *Surf. Eng.* 23 (2007) 279-283.

- [72] A. Kucuk, C.C. Berndt, U. Senturk, R.S. Lima, C.R.C. Lima, Influence of plasma spray parameters on mechanical properties of yttria stabilized zirconia coatings. I: Four point bend test, Mater. Sci. Eng. , A. 284 (2000) 29-40.
- [73] M. Vollenweider, T.J. Brunner, S. Knecht, R.N. Grass, M. Zehnder, T. Imfeld, W.J. Stark, Remineralization of human dentin using ultrafine bioactive glass particles, Acta Biomater. 3 (2007) 936-943.
- [74] ASTM Standard C633, 2008, "Standard Test Method for Adhesion or Cohesion Strength of Thermal Spray Coatings," ASTM International, West Conshohocken, PA, 2003, DOI: 10.1520/C0633-01R08, www.astm.org.
- [75] K.K. Kuo, Principles of Combustion, 1st ed., John Wiley & Sons, New York, 1986.
- [76] M.P. Dewar, A.G. McDonald, A.P. Gerlich, Interfacial heating during low-pressure cold-gas dynamic spraying of aluminum coatings, J. Mater. Sci. 47 (2012) 184-198.
- [77] D.R. Gaskell, Introduction to Thermodynamics of Materials, 5th ed., Taylor & Francis, New York, 2008.
- [78] G. Nelson, J. Nychka, A. McDonald, Flame Spray Deposition of Titanium Alloy-Bioactive Glass Composite Coatings, J. Therm. Spray Technol. 20 (2011) 1339-1351.
- [79] M. Hedayati, M. Salehi, R. Bagheri, M. Panjepour, A. Maghzian, Ball milling preparation and characterization of poly (ether ether ketone)/surface modified silica nanocomposite, Powder Technol. 207 (2011) 296-303.
- [80] ASTM Standard E2109, 2007, "Test Methods for Determining Area Percentage Porosity in Thermal Sprayed Coatings," ASTM International, West Conshohocken, PA, 2003, DOI: 10.1520/E2109-01R07, www.astm.org
- [81] A. Braem, T. Mattheys, B. Neirinck, J. Schrooten, O. Van der Biest, J. Vleugels, Porous Titanium Coatings Through Electrophoretic Deposition of TiH₂ Suspensions, Adv. Eng. Mater. 13 (2011) 509-515.
- [82] D.C. Montgomery, G.C. Runger, Applied Statistics and Probability for Engineers, 4th ed., John Wiley & Sons, New York, 2007.
- [83] R. Boyer, G. Welsch, E.W. Collings, Materials Properties Handbook: Titanium Alloys, (1994).
- [84] J.F. Shackelford, W. Alexander, CRC Materials Science and Engineering Handbook, Third Edition, (2000).

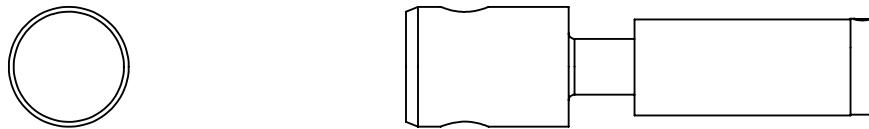
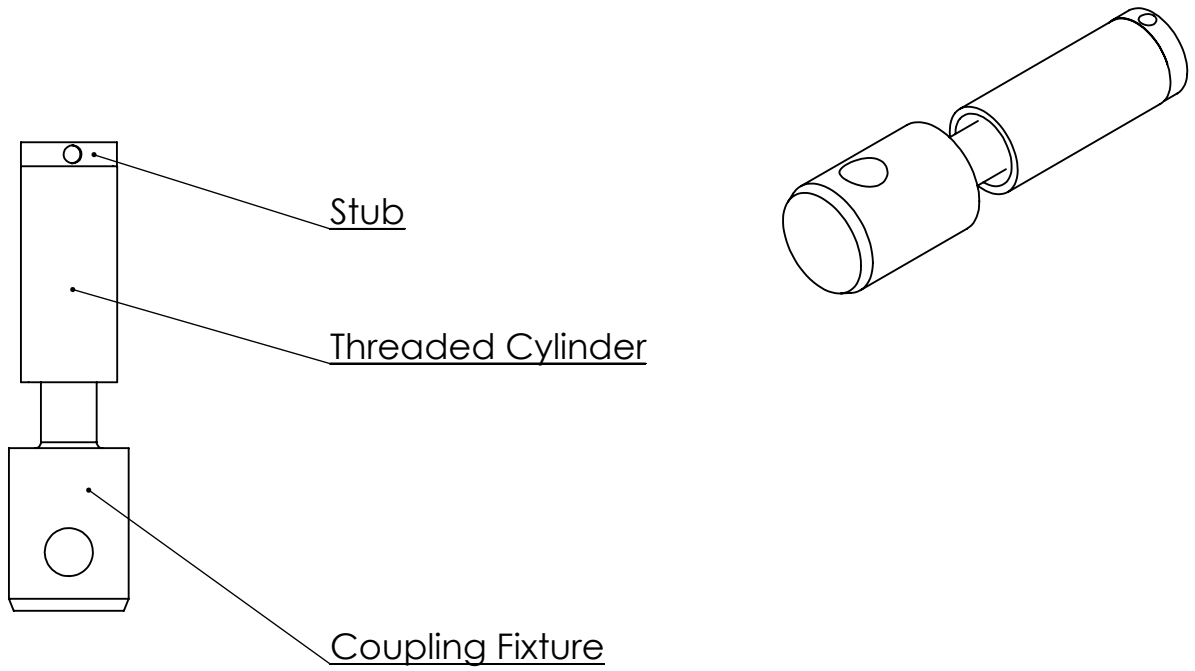
- [85] A.H. Shapiro, *The Dynamics and Thermodynamics of Compressible Flow*, Volume 1, The Ronald Press Company, New York, 1953.
- [86] A.H. Shapiro, *The Dynamics and Thermodynamics of Compressible Flow*, Volume 2, The Ronald Press Company, New York, 1953.
- [87] T.A. Davidson, A simple and accurate method for calculating the viscosity of gaseous mixtures, 9456 (1993).
- [88] E.W. Lemmon, R.T. Jacobsen, Viscosity and thermal conductivity equations for nitrogen, oxygen, argon, and air, *Int. J. Thermophys.* 25 (2004) 21-69.
- [89] P.K. Tondon, S.C. Saxena, Calculation of Thermal Conductivity of Polar-Nonpolar Gas Mixtures, *Applied Scientific Research.* 19 (1968) 163-170.
- [90] E.A. Mason, S.C. Saxena, Approximate Formula for the Thermal Conductivity of Gas Mixtures, *Phys. Fluids.* 1 (1958) 361-369.
- [91] O. Kubaschewski, C.B. Alcock, P.J. Spencer, *Materials Thermochemistry*, 6th ed., Pergamon Press, 1993.
- [92] D.E. Sharp, L.B. Ginther, Effect of Composition and Temperature on the Specific Heat of Glass, *J Am Ceram Soc.* 34 (1951) 260-271.
- [93] Y.A. Çengel, *Heat and Mass Transfer: a practical approach*, 3rd ed., McGraw-Hill, 2007, pp. 861-862.
- [94] L. Lefebvre, J. Chevalier, L. Gremillard, R. Zenati, G. Thollet, D. Bernache-Assolant, A. Govin, Structural transformations of bioactive glass 45S5 with thermal treatments, *Acta Mater.* 55 (2007) 3305-3313.
- [95] F. Motte, C. Coddet, P. Sarrazin, M. Azzopardi, J. Besson, A Comparative Study of the Oxidation with Water Vapor of Pure Titanium and of Ti-6Al-4V, *Oxidation of Metals.* 10 (1976) 113-126.
- [96] D. Clupper, L. Hench, Crystallization kinetics of tape cast bioactive glass 45S5, *J. Non Cryst. Solids.* 318 (2003) 43-48.
- [97] O. Bretcanu, X. Chatzistavrou, K. Paraskevopoulos, R. Conradt, I. Thompson, A.R. Boccaccini, Sintering and crystallisation of 45S5 Bioglass® powder, *J. Eur. Ceram. Soc.* 29 (2009) 3299-3306.
- [98] C. Lin, L. Huang, P. Shen, Na₂CaSi₂O₆-P₂O₅ based bioactive glasses. Part 1: Elasticity and structure, *J. Non Cryst. Solids.* 351 (2005) 3195-3203.

- [99] M. Boivineau, C. Cagran, D. Doytier, V. Eyraud, M.-. Nadal, B. Wilthan, G. Pottlacher, Thermophysical properties of solid and liquid Ti-6Al-4V (TA6V) alloy, *Int. J. Thermophys.* 27 (2006) 507-529.
- [100] J. Kawakita, S. Kuroda, T. Fukushima, H. Katanoda, K. Matsuo, H. Fukanuma, Dense titanium coatings by modified HVOF spraying, *Surf Coat Technol.* 201 (2006).
- [101] K. Kim, M. Watanabe, J. Kawakita, S. Kuroda, Effects of Temperature of In-flight Particles on Bonding and Microstructure in Warm-Sprayed Titanium Deposits, *J. Therm. Spray Technol.* 18 (2009) 392-400.
- [102] B.D. Cullity, S.R. Stock, *Elements of X-Ray Diffraction*, 3rd ed., Prentice Hall, Upper Saddle River, NJ, 2001.
- [103] H. Kay, P. Bailey, Structure and Properties of CaTiO₃, *Acta Crystallogr.* 10 (1957) 219-226.
- [104] G. Pfaff, Synthesis of Calcium Titanate Powders by the Sol-Gel Process, *Chem. Mat.* 6 (1994) 58-62.
- [105] P. Kofstad, *High Temperature Oxidation of Metals*, John Wiley & Sons, New York, 1966.
- [106] R. Devries, R. Roy, E. Osborn, Phase Equilibria in the System CaO-TiO₂-SiO₂, *J Am Ceram Soc.* 38 (1955) 158-171.
- [107] T. Sun, N. Zheng, M. Wang, Characteristics and In Vitro Biologic Assay of Apatite/Titania Composite Coatings on Ti-6Al-4V for Medical Applications, *International Journal of Applied Ceramic Technology.* 9 (2012) 517-528.
- [108] M. Manickam, P. Singh, T. Issa, S. Thurgate, Electrochemical behavior of anatase TiO₂ in aqueous lithium hydroxide electrolyte, *J. Appl. Electrochem.* 36 (2006) 599-602.
- [109] P. Manivasakan, V. Rajendran, P.R. Rauta, B.B. Sahu, P. Sahu, B.K. Panda, S. Valiyaveetill, S. Jegadesan, Effect of TiO₂ Nanoparticles on Properties of Silica Refractory, *J Am Ceram Soc.* 93 (2010) 2236-2243.
- [110] J. Serra, P. González, S. Liste, C. Serra, S. Chiussi, B. León, M. Pérez-Amor, H.O. Ylänen, M. Hupa, FTIR and XPS studies of bioactive silica based glasses, *J. Non Cryst. Solids.* 332 (2003) 20-27.
- [111] D. Zhang, C. Zhang, P. Zhou, Preparation of porous nano-calcium titanate microspheres and its adsorption behavior for heavy metal ion in water, *J. Hazard. Mater.* 186 (2011) 971-977.

- [112] R.S. Lima, B.R. Marple, Enhanced ductility in thermally sprayed titania coating synthesized using a nanostructured feedstock, *Mater. Sci. Eng. , A*. 395 (2005) 269-280.
- [113] M. Taya, Strengthening Mechanisms of Metal Matrix Composites, *Mater. Trans. JIM*. 32 (1991) 1-19.
- [114] J. Eshelby, The Continuum Theory of Lattice Defects, *Solid State Physics-Advances in Research and Applications*. 3 (1956) 79-144.
- [115] W. Miller, F. Humpherys, Strengthening Mechanisms in Particulate Metal Matrix Composites, *Scripta Metallurgica Et Materialia*. 25 (1991) 33-38.
- [116] M. Irfan, V. Prakash, Dynamic deformation and fracture behavior of novel damage tolerant discontinuously reinforced aluminum composites, *Int. J. Solids Structures*. 37 (2000) 4477-4507.
- [117] R.W. Hertzberg, *Deformation and Fracture Mechanics of Engineering Materials*, 4th ed., John Wiley & Sons Inc, New York, 1995.
- [118] Q. Xue, M. Meyers, V. Nesterenko, Self-organization of shear bands in titanium and Ti-6Al-4V alloy, *Acta Materialia*. 50 (2002) 575-596.
- [119] S. Redfern, High-temperature structural phase transitions in perovskite (CaTiO₃), *J. Phys. Condens. Matter*. 8 (1996) 8267-8275.
- [120] M. Koyama, S. Arai, S. Suenaga, M. Nakahashi, Interfacial Reactions between Titanium Film and Single-Crystal Alpha-Al₂O₃, *J. Mater. Sci*. 28 (1993) 830-834.
- [121] X.L. Li, R. Hillel, F. Teyssandier, S.K. Choi, F.J.J. Vanloo, Reactions and Phase-Relations in the Ti-Al-O System, *Acta Metall. Mater*. 40 (1992) 3149-3157.
- [122] J. Kawakita, H. Katanoda, M. Watanabe, K. Yokoyama, S. Kuroda, Warm Spraying: An improved spray process to deposit novel coatings, *Surf Coat Technol*. 202 (2008) 4369-4373.

Chapter 8 – Appendix: Drawings

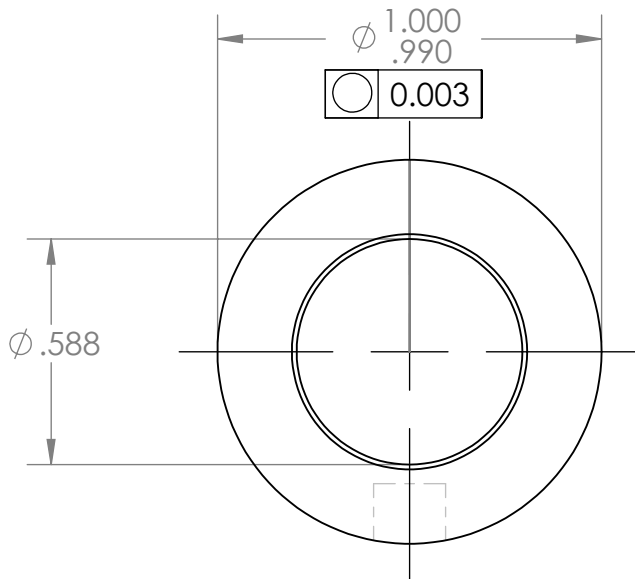
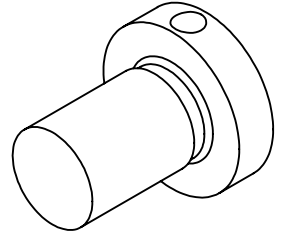
This appendix includes the engineering drawings of the series of fixtures designed for ASTM Standard C633 Tensile Adhesion Testing. All fixtures are constructed of 1045 carbon steel rod with a diameter of 25.4 mm supplied in the turned, ground, and polished state by the Metals Super Market and were fabricated by the staff of the Department of Mechanical Engineering Machine Shop.



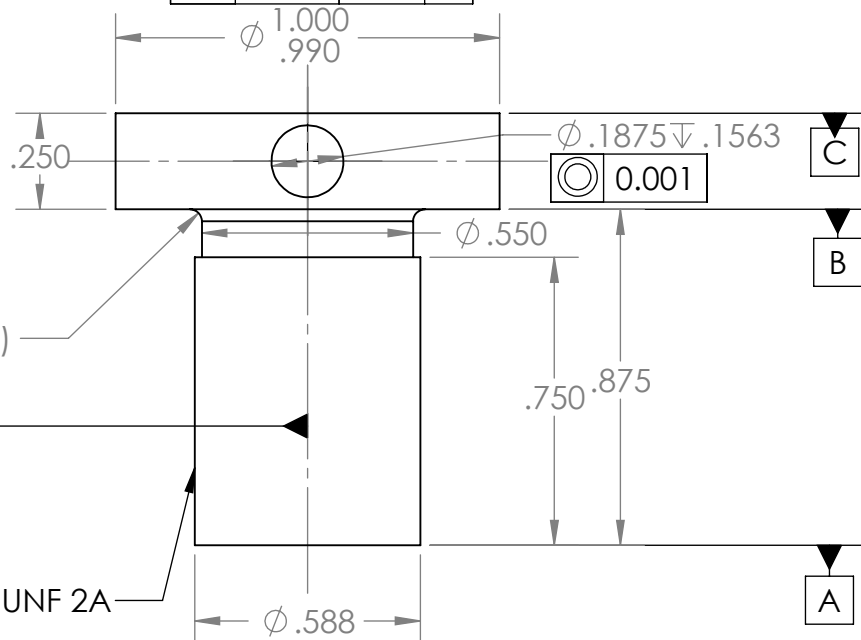
**SolidWorks Student Edition.
For Academic Use Only.**

DIMENSIONS ARE IN INCHES TOLERANCES: FRACTIONAL $\pm 1/64$ " TWO PLACE DECIMAL ± 0.01 " THREE PLACE DECIMAL ± 0.003 " MATERIAL SAE C1045 (Cold finished) FINISH Machined surfaces: 32 DO NOT SCALE DRAWING	NAME	DATE	<h1>Assembly</h1>	
	DRAWN	Greg N		07/03/2013
	CHECKED			
	ENG APPR.			
	MFG APPR.			
	Q.A.			
	COMMENTS:			
	SIZE	DWG. NO.	REV.	
	A	ASTMC633 Assembly		
	SCALE:1:2	WEIGHT:	SHEET 1 OF 1	

Isometric
Scale 1:1



∥	0.003	A	B	C
⊥	0.003	A,B,C	D	



R.0313 (1/32")

D

5/8 - 18 x 0.75" UNF 2A

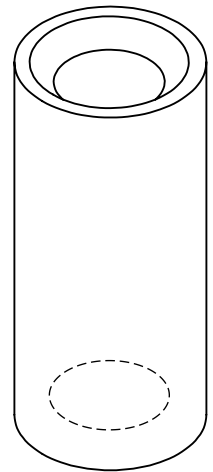
**SolidWorks Student Edition.
For Academic Use Only.**

DIMENSIONS ARE IN INCHES TOLERANCES: FRACTIONAL ± 1/64	
TWO PLACE DECIMAL ± 0.01 THREE PLACE DECIMAL ± 0.003	
MATERIAL	SAE C1045 (cold finished)
FINISH	Machined Surfaces: 32
DO NOT SCALE DRAWING	

	NAME	DATE
DRAWN	Greg N	25/04/12
CHECKED		
ENG APPR.		
MFG APPR.		
Q.A.		
COMMENTS:		

Stub		
SIZE	DWG. NO.	REV.
A	Stub	
SCALE: 2:1	WEIGHT:	SHEET 1 OF 1

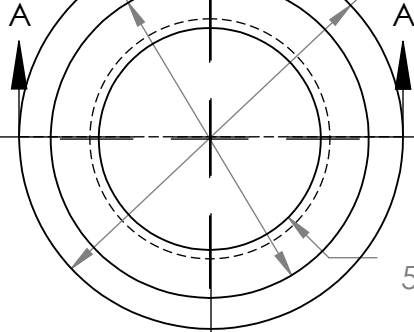
Isometric Scale 1:1



ϕ .828

0.003

ϕ 1.000
 ϕ .990



ϕ .578 THRU ALL
5/8-18 UNF - 2B THRU ALL

ϕ 1.000
 ϕ .990

45 Degree Chamfer

.125

B

2.250

///	0.003	A	B
□	0.003	A, B	C

5/8-18 UNF -2B THRU ALL

2.000

C

45 Degree Chamfer

.578

.828

SECTION A-A

.125

A

**SolidWorks Student Edition.
For Academic Use Only.**

DIMENSIONS ARE IN INCHES
TOLERANCES:
FRACTIONAL $\pm 1/64$
TWO PLACE DECIMAL ± 0.01
THREE PLACE DECIMAL ± 0.003

MATERIAL
SAE C1045 (cold finished)
FINISH
Machined Surfaces: 32

DO NOT SCALE DRAWING

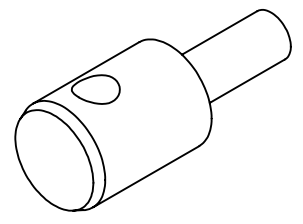
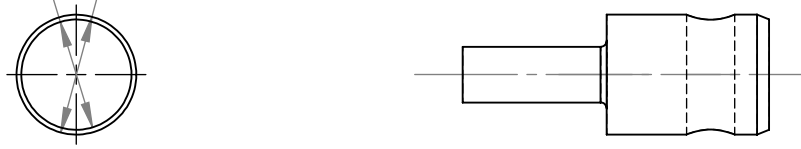
	NAME	DATE
DRAWN	Greg N	07/03/2013
CHECKED		
ENG APPR.		
MFG APPR.		
Q.A.		
COMMENTS:		

Threaded Cylinder

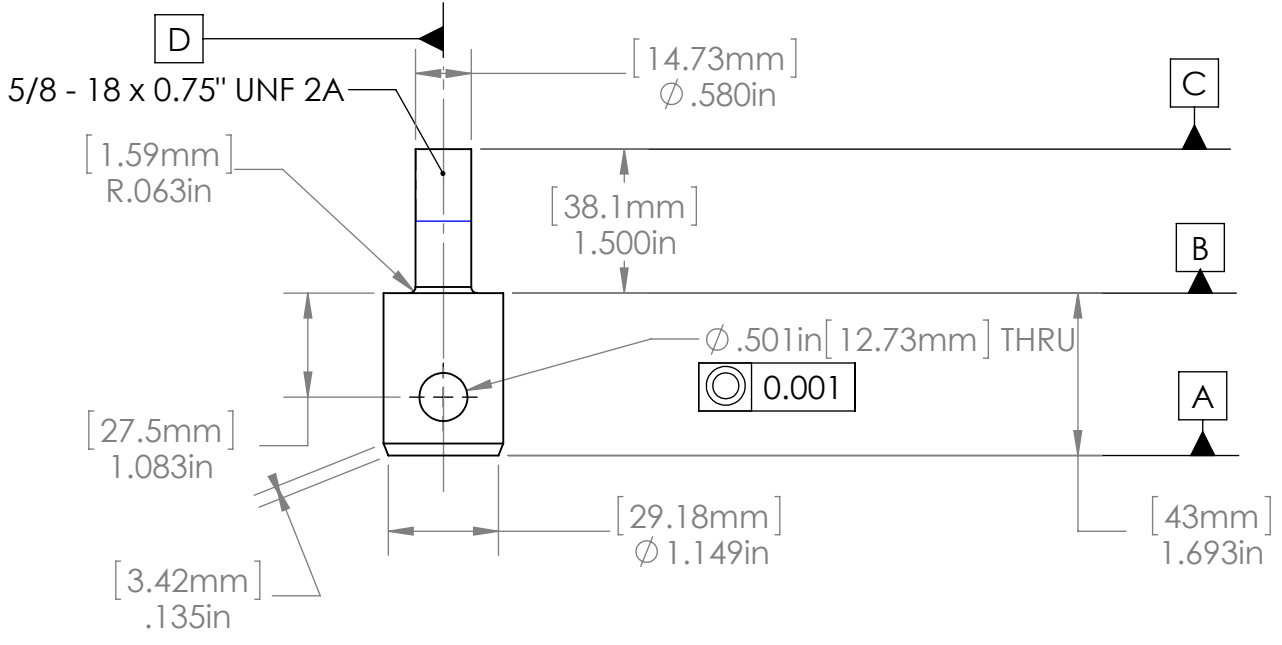
SIZE	DWG. NO.	REV.
A	Threaded Cylinder	
SCALE:2:1	WEIGHT:	SHEET 1 OF 1

[29.18mm]
Ø 1.149in

[31.72mm]
Ø 1.249in



///	0.003	A	B	C
□	0.003	A,B,C	D	



**SolidWorks Student Edition
For Academic Use Only.**

DIMENSIONS ARE IN INCHES
TOLERANCES:
FRACTIONAL ± 1/64"
TWO PLACE DECIMAL ± 0.01"
THREE PLACE DECIMAL ± 0.003"
MATERIAL: SAE C1045 (Cold finished)
FINISH: Machined Surfaces: 32
DO NOT SCALE DRAWING

	NAME	DATE
DRAWN	Greg N	07/03/2013
CHECKED		
ENG APPR.		
MFG APPR.		
Q.A.		
COMMENTS:		

Coupling Fixture

SIZE A	DWG. NO. Coupler	REV.
SCALE:1:2	WEIGHT:	SHEET 1 OF 1